The Resolution and Structure of High Reynolds Number Turbulent Boundary Layers Over Rough and Smooth Walls in Pressure Gradient

Vidya Vishwanathan

Dissertation submitted to the Faculty of the
Virginia Polytechnic Institute and State University
in partial fulfillment of the requirements for the degree of

Doctor of Philosophy
in
Aerospace Engineering

William J. Devenport, Co-chair
K. Todd Lowe, Co-chair
Eric J. Paterson
Bhuvana Srinivasan
Karen A. Flack

December 2nd, 2022
Blacksburg, Virginia

Keywords: Non-Equilibrium Flows, Pressure Gradient, Rough Wall Turbulent Boundary Layers, Smooth Wall Turbulent Boundary Layers.
Copyright 2023, Vidya Vishwanathan

The Resolution and Structure of High Reynolds Number Turbulent Boundary Layers Over Rough and Smooth Walls in Pressure Gradient

Vidya Vishwanathan

(ABSTRACT)

The velocity fields of high Reynolds number, turbulent, wall boundary layers in non-equilibrium pressure gradients are experimentally investigated. Experiments in two wall configurations were performed; one with a hydrodynamically smooth test wall composed of flat aluminum panels, and the other with a rough surface consisting of 2 mm tall, staggered, circular cylindrical elements. A representative set of pressure gradient distributions were generated on the research wall by a systematically rotated NACA 0012 airfoil placed in a wind tunnel section to determine the functional dependence of the boundary layer formation on pressure gradient. Particle image velocimetry (PIV) was the primary measurement technique used to determine time-resolved features of the velocity flow field.

It is shown that regardless of wall condition and Reynolds number, the non-equilibrium turbulent boundary layers exhibit increasingly non-local behavior with streamwise development. This is apparent as a lag to the pressure gradient distribution observed in the streamwise developing integrated boundary layer parameters. These "history effects" are also prevalent in mean velocity profiles which are exhibited as a cross-over of the favorable and adverse pressure gradient profiles in the logarithmic layer. Similar cross-over points are observed in the Reynolds shear and normal stresses, particularly at the streamwise station downstream of the pressure gradient switch. The primary effect of the rough wall is to increase the magnitude of flow scales, and, while they exhibit the same qualitative history effects as the smooth wall, the rough wall flows show an earlier relaxation to equilibrium. Despite inherent uncertainties of indirect skin friction methods for the rough wall, the effective sandgrain roughness parameter k_s does not show a functional dependency to pressure gradient history. An evaluation of the wall-similarity hypothesis solely based on boundary layer thickness to roughness parameter ratios (δ/k_s) is insufficient and additional parameters such as pressure gradient histories, local roughness Reynolds numbers, and bias uncertainties due to instrument spatial resolution must be considered.

The Resolution and Structure of High Reynolds Number Turbulent Boundary Layers Over Rough and Smooth Walls in Pressure Gradient

Vidya Vishwanathan

(GENERAL AUDIENCE ABSTRACT)

In the interface between a surface and a moving fluid is the boundary layer where high shear and viscous stresses cause the bulk velocity to decrease to zero. When turbulent, this region of fluid is characterized by random, chaotic, and fluctuating motions of varying sizes. Parameters such as pressure gradients and geometric irregularities of the surface, referred to as roughness, can increase fluctuating pressures and velocities within the boundary layer and cause unwanted noise, vibration, and increased drag. Although many studies have evaluated boundary layers with either roughness or pressure gradient independently, most surfaces in practical application are susceptible to the compounding influences of both of these parameters. Thus, it is necessary to expand the current knowledge database to include complex flow fields necessary to improve data driven modeling and vehicle design.

This study focuses on experimental observations of the turbulent velocity field developing in both a rough and smooth wall boundary layer that is induced to a family of bi-directional pressure gradients generated by the pressure field of a rotating airfoil inside in a wind tunnel. Through statistical observations of the velocity field it was found that the varying pressure gradients caused the flow to develop non-local dependencies such that the response of the downstream boundary layer was dependent on the upstream flow history. The principal effect of roughness was to increase the magnitude of turbulent scales, but to show the same qualitative response to the pressure gradient history as seen in a smooth wall flow. However, direct comparison of rough and smooth wall turbulence statistics by means of the "wall-similarity hypothesis" requires careful consideration of multiple parameters including these flow histories, scales prescribed by roughness parameters, and bias errors from experiment under-resolution of the velocity field.

Acknowledgments

Getting a PhD is like turbulence; it's chaotic, random, and dispersed with challenges of many sizes. Although, at times the experience was rough, there were many people who made these seemingly adverse times turn favorable. I am forever grateful to have them in my life and for making this adventure wonderfully unforgettable.

Anyone who knows me knows that my family comes first and above all else. I am blessed to not only have the unwavering love and support of my Amma, Appa, and sister Shriya, but the equal (and if not more) affection from my family in New Jersey and Mumbai.

Next I would like to thank my research advisors Dr. William Devenport and Dr. Todd Lowe for their indispensable mentorship. I am privileged to have learned from the very best in the field and am thankful for the valuable time you gave me whenever I needed it. Your patience and guidance have helped me uncover new skills and abilities that I apply even in life beyond research. I hope that I can embody the same level of optimism and research passion you have shown me with people that I meet in the future. I would also like to thank my research committee members Dr. Karen Flack, Dr. Bhuvana Srinivasan, and Dr. Eric Paterson; your advice on my research and future career have introduced me to paths I would never have thought to consider.

I had the genuine pleasure of finding friendship and mentorship from many colleagues in the CREATe research group. Thank you Dr. Máté Szöke and Dr. Agastya Balantrapu for being the first ones to help me navigate the world of graduate school and wind tunnel testing. Thank you to my many CREATe friends, Dr. Nandita Hari, Dr. Christopher Hickling, Surabhi Srivastava, Jarrod Banks, Humza Butt, Shishir Damani, and Adit Acharya who were always there to support me when I needed an extra hand. Thank you to Dr. Aurélien Borgoltz, Bill Oetjens, and the AOE machine shop for always accommodating my requests for your time and expertise. I must acknowledge Chase Leuchtmann, Emily Sellards, Jared Minionis, Kyle Casey, Mason Fitzsimmons, and Sasha Mintz, the undergraduate researchers without whom this experimental work would not have been possible. Thank you to my best friends Carly Norris and Carson Squibb; it made me so happy to come home after a long

day and enjoy your company.

I started graduate school with three exceptional lab mates who have stuck with me through the end. Thank you Julie Duetsch-Patel for being the best "work wife." You always championed my abilities and reminded me that we could get through anything. Thank you to Aldo Gargiulo for giving me his generous time whenever a seemingly simple question would turn into hour long discussions on the fundamentals of turbulence. I learned so much from our conversations, and am constantly in awe of your ability to explain complex topics in such meaningful ways.

Lastly, I was incredibly fortunate to work with the best colleague on this project, Dr. Danny Fritsch. There is a huge amount of work presented in this dissertation that would not have been possible without you. You, quite literally at times, carried the weight of my PIV experiments, and I am very thankful for your constant enthusiasm as we tackled each challenge. Our days (and nights) in the wind tunnel were the highlights of my PhD experience.

Thank you,

Vidya

Contents

List of Figures x

List of Tables xv

1 Introduction 1

1.1 Motivation 1

1.2 Attributions 2

1.3 Scope and Aim of Present Work 2

1.4 Achievements 4

1.5 Structure and Content 5

2 Background and Literature Review 7

2.1 Turbulent Boundary Layers Over Smooth Walls 7

2.1.1 Fundamentals of the Boundary Layer 7

2.1.2 Boundary Layer Regions & Scaling Parameters 8

2.1.3 Governing Equations for Turbulent Flows 10

2.1.4 Characteristics of a Turbulent Boundary Layer 14

2.1.5 Classes of Turbulent Eddies 18

2.1.6 Turbulence Equations for Stress and Transport 20

2.1.7 Skin Friction on Smooth Walls 21

2.2 Rough Wall Turbulent Boundary Layers 22

2.3 Turbulent Boundary Layers in Pressure Gradient 24

2.3.1 Zero-Pressure Gradient (ZPG) 25

2.3.2 Favorable Pressure Gradient (FPG) 25
2.3.3 Adverse Pressure Gradient (APG) 27
2.4 Non-Equilibrium Turbulent Boundary Layers 27
2.5 Summary and Gaps in Literature 29

3 Spatial Resolution Limitations of Particle Image Velocimetry in High Reynolds Number Turbulent Boundary Layers 32

3.1 Abstract 33
3.2 Introduction 34
3.3 Experimental Facilities & Method 36
3.3.1 Facility 36
3.3.2 Pressure Gradient Conditions 36
3.3.3 Wall Conditions 38
3.3.4 PIV Setup and Processing Parameters 38
3.4 Results 40
3.4.1 Mean Velocity and Turbulence Statistics 40
3.4.2 Two-Point Correlation Coefficients 44
3.4.3 Distribution of Energy Density in Wavenumber Spectra 46
3.5 Conclusion 50

4 History Effects and Wall Similarity of Non-Equilibrium Turbulent Boundary Layers in Varying Pressure Gradient Over Rough and Smooth Surfaces 56

4.1 Abstract 57
4.2 Introduction 57
4.3 Experimental Facility 59
4.4 Roughness Geometry 59

4.5 Mechanism for Wall Pressure Gradient 60
4.6 Measurement Systems 61
4.7 Results and Discussion 62
4.7.1 Boundary Layer Development 62
4.7.2 Mean Velocity Profiles 63
4.7.3 Reynolds Stress Profiles 64
4.7.4 Wall-Similarity of the Rough Wall Flow 65
4.8 Conclusions 66
4.9 Acknowledgements 66

5 Analysis of Coherent Structures In Rough and Smooth Wall Turbulent Boundary Layers in Pressure Gradient 71

5.1 Abstract 72
5.2 Nomenclature 72
5.3 Introduction 73
5.4 Analysis Method 75
5.5 Experimental Facility & Setup 77
5.5.1 Virginia Tech Stability Tunnel 77
5.5.2 Airfoil Geometry 77
5.5.3 Roughness Geometry 78
5.5.4 Experimental Systems 79
5.6 Results & Discussion 81
5.6.1 Mean Flow Behaviors 81
5.6.2 Vortex Structure in Instantaneous Velocity Fields 87
5.6.3 Vortex Structure in SPOD Modes 87

5.7 Conclusions 89

6 Conclusions and Outlook **96**

6.1 Conclusions 96

6.2 List of Publications 98

6.2.1 Peer-Reviewed Journal Proceedings 99

6.2.2 Conference Proceedings 99

6.3 Outlook 99

Bibliography **102**

List of Figures

2.1 Mean velocity profile with regions indicated for a zero-pressure gradient turbulent boundary layer over rough and smooth wall. Data points shown as ∘ adapted from Vishwanathan et al. [89]; Spalding profile shown as (—). . . . 8

2.2 Schematic of a mean velocity profile in a boundary layer (left) against the equivalent "displaced" inviscid profile (right). Red shaded regions have equivalent mass and momentum properties between the viscous and displaced inviscid profiles. 15

2.3 Schematic of a streamwise developing boundary layer on a flat plate showing the transitions from laminar to turbulent flow. 15

2.4 From left to right, transition of a horseshoe vortex to a hairpin vortex. From Head and Bandyopadhyay [39] 19

2.5 TKE budget in a flat plate smooth wall turbulent boundary layer. Adapted from Spalart [81] 20

3.1 Top-down schematic of the test section in experiment configuration. PIV measurements for both the magnified (MFOV) and full (FFOV) fields of view are taken at x = 2.74 m for both the rough and smooth wall configurations. 37

3.2 Coefficient of pressure distribution across the test section wall at three angles of attack, $-10^o, 0^o, +12^o$, represented as red, black, and blue curves respectively. Pressures for the rough wall are shown as 37

3.3 Roughness geometry composed of staggered circular cylindrical elements where $d = 3.14$ mm, $s = 6.93$ mm, $k_g = 2$ mm. Adapted from Vishwanathan et al (2022) [90]. 38

3.4 Mean velocity profiles for the smooth wall and rough wall in inner and outer coordinates for when the airfoil is at -10° (FPG), 0° (ZPG), and $+12^o$ (APG). Open circles indicate data from the FFOV PIV and bullet circles indicate data from the MFOV PIV. 41

3.5 Reynolds normal and shear stresses in wall coordinates over the smooth (left) and rough (right) wall measured using both MFOV and FFOV PIV configurations. Data symbols listed in Table 1. 43

3.6 Ratios of the Reynolds stress profiles for the MFOV PIV data normalized on equivalent FFOV data for the smooth (a) and rough (b) wall measurements at $x = 2.74$ m. Colors of symbols indicate the NACA 0012 airfoil at -10°, 0°, $+12^o$. Profiles for $\overline{u^2}$ ratio shown as $\triangle$ 45

3.7 Ratios of the Reynolds stress profiles for the MFOV PIV data normalized on equivalent FFOV data for the smooth (a) and rough (b) wall measurements at $x = 3.94$ m. Colors of symbols indicate the NACA 0012 airfoil at -10°, 0°, $+12^o$. Profiles for $\overline{u^2}$ ratio shown as $\triangle$, $\overline{v^2}$ ratio shown as $*$. 46

3.8 Streamwise (left) and wall-normal (right), single-sided, two-point correlation coefficients for the smooth wall at a $y^+ = 500$ (a) and $y^+ = 3500$ (b) measured using both the MFOV (- - - - -) and FFOV (.....) PIV configurations. Line color indicates the NACA 0012 airfoil angle of attack at -10°, 0°, $+12^o$. . . . 47

3.9 Streamwise (left) and wall-normal (right), single-sided, two-point correlation coefficients for the rough wall at a $y^+ = 500$ (a) and $y^+ = 3500$ (b) measured using both the MFOV (- - - - -) and FFOV (.....) PIV configurations. Line color indicates the NACA 0012 airfoil angle of attack at -10°, 0°, $+12^o$. . . . 48

3.10 Streamwise (left) and wall-normal (right) length-scales as a function of wall-normal position for the smooth wall. Data symbols listed in Table 1 49

3.11 Streamwise (left) and wall-normal (right) length-scales as a function of wall-normal position for the rough wall. Data symbols listed in Table 1 49

3.12 Smooth wall wavenumber spectra at $\alpha = 12^o$ for the magnified (left) and full (right) fields of view; (a) streamwise, $log(k_x\phi_{uu}/u_\tau^2)$ and (b) wall-normal $log(k_x\phi_{vv}/u_\tau^2)$. 51

3.13 Rough wall wavenumber spectra at $\alpha = 12^o$ for the magnified (left) and full (right) fields of view; (a) streamwise, $log(k_x\phi_{uu}/u_\tau^2)$ and (b) wall-normal $log(k_x\phi_{vv}/u_\tau^2)$. 52

4.1 Top-down schematic of the test section. Boundary layer wall of interest is the "port" wall, seen here as the lower wall,which was either in smooth or rough wall configuration. Measurement locations of the boundary layer rake and TR-PIV are indicated in vertical black and green lines, respectively. 59

4.2 Staggered, circular cylindrical roughness configuration used in this study; s = 6.93mm, d = 3.14mm, kg = 2mm. 60

4.3 Streamwise variation of the Clauser pressure gradient parameter, β, as a function of the NACA 0012 angle of attack shown at the boundary layer rake measurement locations. Solid lines are the rough wall, dashed lines are the smooth wall. Vertical dashed lines indicate locations of the airfoil leading and trailing edge, respectively. Vertical solid lines indicate the locations of the TR-PIV measurements. Color legend is used for subsequent figures unless otherwise noted. 61

4.4 Momentum thickness variation with streamwise distance and NACA 0012 angle of attack. Symbol and color legend same as Figure 3. 63

4.5 Mean velocity profiles normalized on inner coordinates for rough (solid colored lines) and smooth (dashed lines) configurations at (top) x = 2.62 m and (bottom) x = 4.05 m. Solid black line is the Spalding curve (Spalding (1961).) 64

4.6 Rough wall mean velocity profiles in mixed outer-coordinates and logarithmic-law diagnostic function used to select the logarithmic region for regression fit methods to determine skin friction from mean velocity profiles; (top) x = 2.62 m and (bottom) x = 4.05 m. 67

4.7 Reynolds streamwise normal turbulence stress plotted on inner-outer coordinates for the rough ($\circ$) and smooth wall (x); (left) x = 2.74 m and (right) x = 3.69 m, for which the inset shows a zoomed-in view of the profiles. . . . 68

4.8 δ/k_s for the rough wall boundary layer. Symbol and color legend same as Figure 3. 68

4.9 Effective sandgrain roughness parameter (k_s) normalized by roughness height (k_g) computed from a regression fit of the mean velocity profiles. (Top) the selected logarithmic region is custom to each flow condition, and (bottom) the logarithmic region is taken to be between $8680 < yU_e/\nu < 21270$. 69

5.1 Top-down schematic of test section. Boundary layer wall of interest is the "port" wall, seen here as the lower wall. Green lines indicate locations of TR-PIV planes corresponding to stations maximum upstream and downstream $\partial p/\partial x$) at $x = 2.74$ m and $x = 3.94$ m, and at the maximum p at $x = 3.31$ m. 77

5.2 Staggered, circular cylindrical roughness configuration used in this study; $s = 6.93$ mm, $d = 3.14$ mm, $k_g = 2$ mm. Inset shows features of a cylindrical element. 78

5.3 Pressure coefficient (top) and pressure coefficient gradient (bottom) distributions on the research wall due to pressure gradients generated by the NACA 0012 airfoil for the rough (———) and smooth (- - - -) wall flows. Vertical lines indicate the streamwise locations of the leading and trailing edge of the airfoil at 0° angle of attack. 80

5.4 Displacement thickness with streamwise position as a function of pressure gradient. Color and symbol legend same as Figure 3. 82

5.5 Mean velocity profiles in defect coordinates at (left) $x = 2.74$ m, (middle) $x = 3.31$ m, (right) $x = 3.94$ m for the smooth ($\circ$) and rough ($\times$) wall boundary layers. 83

5.6 Streamwise Reynolds stress for the smooth (top) and rough (bottom) wall by streamwise station and airfoil angle of attack. Color legend same as for Figure 5 84

5.7 Wall-normal Reynolds stress for the smooth (top) and rough (bottom) wall by streamwise station and airfoil angle of attack. Color legend same as for Figure 5 85

5.8 Reynolds shear stress for the smooth (top) and rough (bottom) wall by streamwise station and airfoil angle of attack. Color legend same as for Figure 5 86

5.9 See Figure 10 for caption 88

5.10 Instantaneous and Reynolds decomposed fluctuating velocity fields for the smooth wall (Figure 99) and for the rough wall (present figure) flow with the airfoil at $+12^o$ at (a) $x = 2.74$ m, (b) $x = 3.31$ m, and (c) $x = 3.94$ m plotted over the color contour of the mean velocity normalized on local edge velocity ($\overline{U}/U_e$). 89

5.11 SPOD modes for a characteristic frequency corresponding to a $y/\delta = 0.5$ position for the smooth (top) and rough (bottom) wall at $x = 2.74$ m. 90

5.12 SPOD modes for a characteristic frequency corresponding to a $y/\delta = 0.5$ position for the smooth (top) and rough (bottom) wall at $x = 3.31$ m. 91

5.13 SPOD modes for a characteristic frequency corresponding to a $y/\delta = 0.5$ position for the smooth (top) and rough (bottom) wall at $x = 3.94$ m. 92

List of Tables

3.1 Smooth and rough wall flow parameters at $x \approx 2.74$ m. 39

5.1 Smooth and rough wall flow parameters at $x = 2.74$ m. 80

5.2 Smooth and rough wall flow parameters at $x = 3.31$ m. 81

5.3 Smooth and rough wall flow parameters at $x = 3.94$ m. 81

Nomenclature & Abbreviations

β	Clauser pressure gradient parameter
ΔU^+	Roughness function
δ	Boundary layer thickness
δ^*	Displacement thickness
ϵ	Dissipation rate
κ	von Kármán constant
λ	Taylor microscale (denoted with subscript i) or roughness sparseness parameter
ν	Kinematic viscosity
$\overline{U_i}$	Average velocity in the i-coordinate direction
ϕ_{ij}	Spectral density of variables i, j
Π	Wake strength parameter
ρ	Density
τ_w	Wall shear stress
θ	Momentum thickness
C_f	Skin friction coefficient
C_p	Pressure coefficient
k_g	Roughness element height
k_i	Wavenumber in i coordinate direction
k_s	Effective sandgrain roughness
u_τ	Shear velocity

U_e	Boundary layer edge velocity
U_i	Instantaneous velocity in the i-coordinate direction
f	Time frequency
H	Shape factor δ^*/θ
L	Characteristic length scale
P	Dimensional pressure
Re	Reynolds Number
t	Time

Chapter 1

Introduction

1.1 Motivation

Turbulent boundary layers are omnipresent in a wide range of practical applications, such as over an aircraft wing or marine vehicle body. A wide of range of studies have established a fundamental understanding of the uni-directional pressure gradient flow, often this being the canonical zero pressure gradient in the form of a flat plate. However, aside from use in controlled laboratory environments, these simple flows are just the building blocks for flows of practical interest. Real flows are susceptible to complex conditions impacted by roughness and bi-directional pressure gradients (i.e., pressure gradients that switch sign). Surfaces in engineering application are usually not considered hydrodynamically smooth either due to macroscopic defects in the surface finish or due to buildup of natural roughness such as icing on aircraft and barnacles on ship hulls. Roughness can contribute to drag, unwanted vibrations, and noise, which can negatively impact the operation and design of these vehicles. However, these flows are more difficult to model, thus improving the current array of knowledge for flows in non-equilibrium conditions is a relevant field of interest.

This research aims to expand the current knowledge database of complex flow fields entailing roughness and pressure gradient effects on high Reynolds number, wall-bounded turbulence. Knowledge of baseline smooth wall conditions is a necessary precursor to experiments in roughness. Hence, this experimental research is conducted to evaluate the velocity fluctuations of both rough and smooth wall flow conditions. This PhD work largely focuses on the understanding of the instantaneous velocity field using time-resolved particle image velocimetry (TR-PIV), and other measures of mean velocity flow conditions.

By convention, the rough and smooth wall behaviors are compared on the basis of A.A. Townsend's wall-similarity hypothesis [87], which suggests that, outside the immediate vicinity of the roughness sublayer, the rough wall boundary layer behaves similar to a smooth

wall with equivalent scales. The validity of the wall-similarity hypothesis has often been the subject of scrutiny in literature. While this school of thought is convenient in many applications, particularly simplifying roughness modeling to be analogous to smooth wall analysis, there is an insufficient understanding of the multivariable matching necessary to compare rough and smooth wall flows in non-equilibrium flow fields. The current work explains the key features of turbulence structures evolving in a non-equilibrium turbulent boundary layer and evaluates the experiment measurement limitations in accurately representing the flow of interest.

1.2 Attributions

The work presented in this dissertation was completed in collaboration with a partner colleague and two research mentors mentioned below.

Dr. Daniel J. Fritsch has been a close collaborator on this project who was responsible for all computational and experimental work of the fluctuating pressure field. He partnered in the experiment design, setup, and data acquisition. He is a co-author on several of the listed journal and conference publications, and his dissertation on modeling the fluctuating pressure field provides a companion perspective to present investigation of the fluctuating velocity measurements made of the same flow field.

Dr. William J. Devenport and **Dr. K. Todd Lowe** served as the project principal investigators and secured the grant and reseach funding from the Office of Naval Research. They served as co-chairs for the research advisory committee and advised all aspects of the work presented in both in this dissertation and in articles submitted for conference and peer-reviewed publication.

1.3 Scope and Aim of Present Work

The main objective of this work is to improve the fundamental understanding of the behavior and measurement limitations of velocity fields of non-equilibrium turbulent boundary layers over rough and smooth surfaces. Specifically, this experimental work is accomplished by investigating flow developing over the differing wall conditions in a functionally dependent

pressure gradient field generated by the blockage of a NACA 0012 in a wind tunnel test section. This present work has three specific aims which are outlined below.

1. Understand the limitations of multi-point measurement techniques, such as particle image velocimetry, in accurately measuring turbulence statistics of high Reynolds number boundary layers over rough and smooth surfaces. This objective is to,
   (a) Reveal attentuation of turbulence magnitudes with coarse and fine spatial resolution measurements.
   (b) Assess variations in the level of turbulence attenuation with different wall conditions and local Reynolds number.
   (c) Estimate a level of bias uncertainty associated with PIV under-resolution.
2. Challenge the validity of the wall-similarity hypothesis used to compare flow in rough and smooth wall flows, particularly pertaining to flow developing in a non-equilibrium pressure gradient field. Specifically, we will seek to,
   (a) Compare mean velocity and turbulence stress profiles in both wall conditions using conventional forms of scaling.
   (b) Assess non-local tendencies of the flow development that contribute to variations of flow behaviors.
   (c) Suggest a multivariable set of parameters to improve experiment design intended to satisfy wall-similarity.
3. Reveal the distribution and content of energetic turbulence structures in a rough and smooth wall boundary layer induced by a non-equilibrium pressure gradient. The approach to improve this understanding is to:
   (a) Compare mean statistics of the rough and smooth wall to identify flow variations with local Reynolds number.
   (b) Specify regions of specific interest within the boundary layer from assessment of the Reynolds stress profiles.
   (c) Qualitatively compare the instantaneous velocity field using spectral proper orthogonal decomposition to reveal shape and distribution of coherent structures developing at specific wall-normal distances.

1.4 Achievements

- Regardless of wall condition and Reynolds number the flow in a non-equilibrium turbulent boundary layer exhibits increasingly non-local behavior with streamwise development. This is apparent as a lag in the response of the streamwise developing integrated boundary layer parameters (i.e. skin friction, momentum thickness, displacement thickness) to the pressure gradient distribution. This behavior is referred to as a "history effect."

- There is clear evidence that rough wall boundary layers reduces the relaxation time to equilibrium in non-equilibrium flows.

- History effects are also prevalent in the mean velocity and Reynolds stress behaviors. In the mean velocity profiles, this is demonstrated as a "cross-over" of the favorable and adverse pressure gradient profiles in the logarithmic layer. Similar cross-over points are observed in the Reynolds shear and normal stresses, particularly at the streamwise station downstream of the pressure gradient switch. This behavior is indicative of a stress bore which gives indication of a large outward transport of velocities encompassed in these layers.

- For rough wall flows, indirect methods to determine skin friction, specifically using regression fits of the mean velocity profiles, show high sensitivity to of the selected logarithmic region on the computed shear stresses. Direct measurements of skin friction are necessary to accurately compare wall conditions on the basis of wall-similarity.

- The validity of wall-similarity is relevant to a huge range of engineering and modeling applications, but the present study has revealed that multiple criteria pertaining to flow histories, boundary layer thickness to roughness parameter ratios, and local Reynolds numbers must be matched to an equivalent smooth wall case for proper comparison on the basis of this hypothesis. Despite inherent uncertainties of indirect skin friction methods for the rough wall, the effective sandgrain roughness parameter is constant with pressure gradient history.

- Spatial resolution limitations of PIV experiments cause an attenuation of the measured turbulence statistics. There is no discernible impact of the resolution limitation to the resulting mean velocity profiles. However, Reynolds stresses show depressed values

with coarser resolutions, with particular impacts to the wall-normal velocity components. This reduction was shown to be due to the smaller correlation lengthscales occurring the wall-normal direction as opposed to the energy-dominant larger scales occurring in the predominantly streamwise structures.

- A fixed spatial resolution presents limitations for studies in which variable flow conditions are compared. This is because the range of scales of turbulence, dictated by the local Reynolds number, has a threshold of detection based on the instrument resolution. This limitation results in a higher disparity of Reynolds stress magnitudes of measurements made with a coarse and fine resolution when the flow is an initially adverse pressure gradient, a disparity that is comparably lower in flows in an initially zero or favorable pressure gradient.

- A comparison of the same variable quantities between the rough and smooth wall boundary layers show that the a coarse resolution can attenuate the computed Reynolds stresses for both rough and smooth wall flows. However, this stress magnitude reduction is more prevalent in the smooth wall flow, while the rough wall flow shows attenuation at certain local Reynolds numbers. Nevertheless, an evaluation of biases from under-resolution of non-dominant stress components is still necessary in the design of rough and smooth wall experiments.

- Qualitative analysis of the instantaneous smooth wall velocity fields shows evidence of Townsend's attached eddy hypothesis with the enlargement of eddy scales with wall-normal distance under adverse pressure gradient conditions.

- Both spectral proper orthogonal decomposition on the velocity fields and an evaluation of the instantaneous flow field shows that, although the rough wall qualitatively responds to the pressure gradient histories as the smooth wall, there are fundamental differences in the velocity field structure and shape, again emphasizing the need to match multiple variables for comparison of rough and smooth wall boundary layers on the basis of wall-similarity.

1.5 Structure and Content

This dissertation is organized as follows.

Chapter 1 introduces the research project and motivation and summarizes the key findings from the dissertation work.

Chapter 2 provides a summary of the fundamental flow physics of a turbulent boundary layer as well as a review of the relevant literature pertaining to non-equilibrium rough and smooth wall conditions.

Chapter 3 contains a manuscript titled "Spatial Resolution Limitations of Particle Image Velocimetry in High Reynolds Number Turbulent Boundary Layers," to be submitted for peer-review to *Experiments in Fluids*. This chapter provides an evaluation of measurement limitations of particle image velocimetry in resolving turbulence statistics below the instrument spatial resolution.

Chapter 4 contains a manuscript titled "History Effects and Wall Similarity of Non-Equilibrium Turbulent Boundary Layers in Varying Pressure Gradient Over Rough and Smooth Surfaces" to be submitted to the *International Journal for Heat and Fluid Flow*. The contents of this chapter investigate the wall-similarity hypothesis and non-equilibrium behaviors of rough and smooth wall turbulent boundary layers.

Chapter 5 contains a manuscript titled "Analysis of Coherent Structures Over a Smooth Wall Turbulent Boundary Layer in Pressure Gradient." This chapter contains an analysis of coherent structures identified using the spectral proper orthogonal decomposition (SPOD) technique applied to the time-resolved PIV data measured over smooth and rough surfaces.

Chapter 6 provides a summary of the dissertation work and discusses future avenues for continued investigation.

The formatting of this dissertation varies across chapters as the manuscripts for journal submission are in the format prescribed by the publisher.

Chapter 2

Background and Literature Review

2.1 Turbulent Boundary Layers Over Smooth Walls

This section will provide a fundamental review of the flow physics and governing equations related to turbulent boundary layers, particularly over smooth walls. The subsequent section discussing turbulent boundary layers over rough walls will build from the fundamentals examined in this section.

2.1.1 Fundamentals of the Boundary Layer

As flow passes over a body, the interface of the solid surface and the fluid is a region of high viscous and shear frictional forces; this region is known as a boundary layer. On a molecular level, there is still friction on the surface resulting in a velocity gradient where the flow within the boundary layer is slower than that of the freestream. At the surface, the fluid loses all its momentum, thus resulting in a zero-flow condition, often referred to as the "no-slip condition," and is represented as a sink for fluid momentum [76]. The flow at the edge of the region of high shear will follow a value dependent on the free-stream condition, typically determined by the inflow velocity conditions or the surface curvature (i.e., presence of pressure gradients). The point at which the velocity profile with gradient blends into the freestream is referred to as the boundary layer thickness, δ. Often, this point is approximated as the wall-normal distance corresponding to the point at which the mean velocity reaches 99% of the edge velocity, U_e.

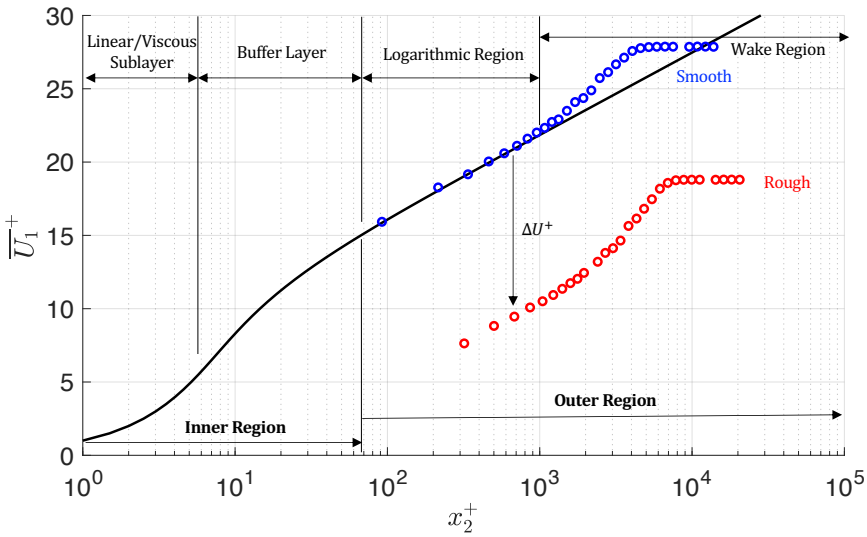

Figure 2.1: Mean velocity profile with regions indicated for a zero-pressure gradient turbulent boundary layer over rough and smooth wall. Data points shown as ∘ adapted from Vishwanathan et al. [89]; Spalding profile shown as (—).

2.1.2 Boundary Layer Regions & Scaling Parameters

Although a thin shear layer, the boundary layer itself can be decomposed into several regions where the flow conditions dictate certain behaviors of the flow such as the presence and magnitude of turbulent eddies and relative velocities depending on the proximity to either the freestream or the surface. The classical separation of these regions for a mean velocity profile in inner coordinates is shown in Figure 2.1. The regions are often identified using scaling parameters, classically broken down into the "inner" and "outer" regions, which collapse the profiles to a single curve in the respective regions. The inner region, close to the wall, is largely affected by viscosity and the velocity scales on the friction velocity, u_τ and the lengths scale on the parameter $\frac{\nu}{u_\tau}$. The friction velocity is defined in terms of the wall shear stress, τ_w and the fluid density ρ as:

$$u_\tau = \sqrt{\frac{\tau_w}{\rho}} \tag{2.1}$$

The region closest to the wall is referred to as the linear sublayer at which point the turbulence is largely dominated by dissipation due to the overwhelming viscous effects in this region and the mean velocity is directly proportional to the distance from the wall. Moving away

away from the wall, the velocity gradient starts becoming independent from the viscous effects near the wall and the linear sublayer merges into the logarithmic region by means of an "overlap" or a "buffer" layer. Here, the mean velocity exhibits behaviors common to both the linear sublayer and the logarithmic regions. As its name implies, the mean velocity in the logarithmic region follows a logarithmic profile defined by the law of the wall, given in equation 2.3, where parameters with superscripts of "+" are normalized on the inner scaling parameters. The constants κ (von Kármán constant) and C typically taken to be around $\kappa = 0.41$ and $C = 5.0$. Further subdivisions of the boundary layer have been a topic of interest in literature. For instance, in their work of a zero-pressure gradient (ZPG) turbulent boundary layer, George and Castillo [35] established a region called the mesolayer above which turbulence dissipation is dominated by inertial effects, and below which viscous effects are dominant [35]. They describe the mesolayer as another overlap region that merges into the outer layer of the boundary layer. However, the divisions shown in Figure 2.1 are used in practice for purposes of most studies, including the present one.

The outer region is scaled on parameters indicative of the larger scales of the boundary layer which are the edge velocity, U_e and the boundary layer thickness, δ. In this region, the law of the wall amasses an additional term describing the wake effect of the mean velocity and is renamed the "law of the wake" given in equation 2.4, first introduced by Coles, in which the wake parameter is a function of wall distance shown in equation 2.4b [21].

$$\overline{u^+} = y^+ \tag{2.2}$$

$$\overline{u^+} = \frac{1}{\kappa} ln(y^+) + C \tag{2.3}$$

$$\overline{u^+} = \frac{1}{\kappa} + C + \frac{\Pi}{\kappa} W\left(\frac{y}{\delta}\right) \tag{2.4a}$$

Where

$$W(0) = 0, W(1) = 0, \int_0^2 \frac{y}{\delta}\, dW \ = 1 \tag{2.4b}$$

2.1.3 Governing Equations for Turbulent Flows

The Reynolds-Averaged Navier-Stokes Equations

The Navier-Stokes equations, which entail the conservation of mass and momentum, serve as the governing equations of motion for fluid flows. We will consider an incompressible, two-dimensional mean flow, with the density (ρ) and fluid kinematic viscosity (ν) assumed constant. Thus, the Navier-Stokes equations are simplified and are written in differential from as shown below:

$$\frac{\partial u_i}{\partial x_i} = 0 \tag{2.5}$$

$$\frac{\partial u_i}{\partial t} + \frac{\partial u_i u_j}{\partial x_j} = -\frac{1}{\rho}\frac{\partial p}{\partial x_i} + \nu\frac{\partial^2 u_i}{\partial x_j^2} \tag{2.6}$$

Where p is the instantaneous fluid pressure and u_i is the instantaneous velocity in the i-coordinate direction, where i varies as 1, 2, and 3 for streamwise, wall-normal, and spanwise directions respectively.

The flow outside the boundary layer (i.e. the freestream) is irrotational and thus a further simplification to the Navier-Stokes equations can be made as the viscous term in the conservation of momentum is identically zero; these equations for the inviscid flow are known as the Euler equations. The limitations of satisfying both the no-slip condition for the boundary layer and the inviscid freestream approximations to the Navier-Stokes equations were recognized by Ludwing Prandtl in 1905, who reasoned that for flows with a sufficiently high Reynolds number, the flow could be subdivided into a region of high shear (i.e., the boundary layer), and the freestream [71].

Due to the unsteady nature of turbulence, it is difficult to predict or make assumptions on the flow field in terms of its instantaneous values. And for a steady mean flow, the time-average of turbulence properties are stationary. So, it is more convenient to treat the boundary layer equations as the expected value of its Reynolds decomposed form, which separates the instantaneous components into its mean (denoted as an uppercase variable or an overbar) and fluctuating (denoted with an apostrophe) parts. For instance, the Reynolds decomposition for the velocity is written as, $u_i = U_i - u_i'$. Noting that the time-average

of a fluctuating component is zero, the expected value of the Reynolds decomposed steady, two-dimensional, conservation of mass and momentum is simplified as follows:

$$\frac{\partial U_i}{\partial x_i} = 0 \tag{2.7}$$

$$U_i \frac{\partial U_j}{\partial x_j} = -\frac{1}{\rho}\frac{\partial P}{\partial x_i} - \frac{\partial \overline{u_i' u_j'}}{\partial x_j} + \nu \frac{\partial^2 U_i}{\partial x_j^2} \tag{2.8}$$

This form of the incompressible conservation laws is referred to as the Reynolds-Averaged Navier-Stokes (RANS) equations. Note that the decomposition of the convective term explicitly introduces a term for the velocity correlations $\overline{u_i' u_j'}$, also known as the Reynolds shear and normal stresses. The trace of the diagonals of the Reynolds stress tensor is referred to as the turbulent kinetic energy (TKE), k, and is defined in equation 2.9 below:

$$k = \frac{1}{2}\overline{u_i^2} \tag{2.9}$$

However, with this additional Reynolds stress term, there are now a large number of unknowns and insufficient equations when attempting to solve for the TKE from the Navier-Stokes equations, the disparity for which only increases for higher order terms. This is referred to as the closure problem. The solution to the closure problem comes from a variety of turbulence models that make assumptions with regards to the turbulent viscosity and the TKE. Thus, turbulence models, such as the Boussinesq eddy viscosity model or Prandtl's mixing-length model must be implemented to solve these equations requiring a statistical evaluation of the Navier-Stokes equations [70]. More practical and advanced turbulence models exist (i.e., Spalart-Almaras, Menter k_ω SST, etc...), the discussion for which is beyond the scope of this PhD.

The Turbulent Boundary Layer Equations

As the boundary layer encompasses only a thin region of the flow, the RANS equations can be further simplified by means of scale-analysis, a method that compares the scales of the variables with respect to fixed reference values, such as the streamwise freestream velocity, U_∞ and largest length scales, L, in each component direction, and neglects the

trivial terms. The boundary layer thickness, δ, is taken to be the predominant length scale in the wall-normal direction, which is still a small percentage of the predominant length scale L. Thus, the normalized variables, denoted with a $*$ superscript, are defined as $U_i^* = U_i/U_\infty$, $u_i^* = u_i'/U_\infty$, $x_1^* = x_1/L$, $x_3^* = x_3/L$, $x_2^* = x_2/\delta$, and $P^* = P/\rho U_\infty^2$. Applying these normalizations to the RANS equation for continuity:

$$\frac{\partial U_1^*}{\partial x_1^*} + \frac{L}{\delta}\frac{\partial U_2^*}{\partial x_2^*} + \frac{\partial U_3^*}{\partial x_3^*} = 0 \tag{2.10}$$

With this normalization it is shown that the ratio of U_1 and U_3 on the reference velocity is on the order of 1 and the U_2 velocity component is on the order $U_\infty\delta/L$. The normalization performed and simplified for the x_1 momentum equation is shown below:

$$\begin{aligned} U_1^*\frac{\partial U_1^*}{\partial x_1^*} + U_2^*\frac{L}{\delta}\frac{\partial U_1^*}{\partial x_2^*} + U_3^*\frac{\partial U_1^*}{\partial x_3^*} = -\frac{\partial P^*}{\partial x_1^*} - \frac{\partial \overline{u_1^{*2}}}{\partial x_1^*} - \frac{L}{\delta}\frac{\partial \overline{u_1^* u_2^*}}{\partial x_2^*} - \frac{\partial \overline{u_1^* u_3^*}}{\partial x_3^*} + \\ \frac{\nu}{U_\infty L}\left[\frac{\partial^2 U_1^*}{\partial x_1^{*2}} + \frac{L^2}{\delta^2}\frac{\partial^2 U_1^*}{\partial x_2^{*2}} + \frac{\partial^2 U_1^*}{\partial x_3^{*2}}\right] \end{aligned} \tag{2.11}$$

As observed earlier for in equation 2.10, we see that the convective terms and the pressure gradient term in equation 2.11 are also of order 1. However, the $\overline{u_1^{*2}}$ and $\overline{u_1^* u_3^*}$ are small when non-dimensionalized on the characteristic velocity and can be neglected. The normalization of $\nu/U_\infty L$ is noted to be the inverse of the Reynolds number, a non-dimensional parameter describing the ratio of inertial to viscous forces. For large Reynolds numbers, which will be the case for turbulent flows analyzed in this work, the first and third diffusion terms are considered negligble when compared to terms normalized on the length scales. Applying the same process for the x_3 momentum equation, the streamwise and spanwise expressions are approximated as:

$$U_1\frac{\partial U_1}{\partial x_1} + U_2\frac{\partial U_1}{\partial x_2} + U_3\frac{\partial U_1}{\partial x_3} \approx -\frac{1}{\rho}\frac{\partial P}{\partial x_1} - \frac{\partial \overline{u_1' u_2'}}{\partial x_2} + \nu\frac{\partial^2 U_1}{\partial x_2^2} \tag{2.12}$$

$$U_1\frac{\partial U_3}{\partial x_1} + U_2\frac{\partial U_3}{\partial x_2} + U_3\frac{\partial U_3}{\partial x_3} \approx -\frac{1}{\rho}\frac{\partial P}{\partial x_3} - \frac{\partial \overline{u_2' u_3'}}{\partial x_2} + \nu\frac{\partial^2 U_3}{\partial x_2^2} \tag{2.13}$$

There are slight differences for the x_2 momentum equation due to the length scale normalizations and a different process for scale analysis occurs. The non-dimensional x_2 momentum equation is given as:

$$\begin{aligned} U_1^*\frac{\partial U_2^*}{\partial x_1^*} + U_2^*\frac{L}{\delta}\frac{\partial U_2^*}{\partial x_2^*} + U_3^*\frac{\partial U_2^*}{\partial x_3^*} = -\frac{L}{\delta}\frac{\partial P^*}{\partial x_2^*} - \frac{\partial \overline{u_1^* u_2^*}}{\partial x_1^*} - \frac{L}{\delta}\frac{\partial \overline{u_2^{*2}}}{\partial x_2^*} - \frac{\partial \overline{u_2^* u_3^*}}{\partial x_3^*} + \\ \frac{\nu}{U_\infty L}\left[\frac{\partial^2 U_2^*}{\partial x_1^{*2}} + \frac{L^2}{\delta^2}\frac{\partial^2 U_2^*}{\partial x_2^{*2}} + \frac{\partial^2 U_2^*}{\partial x_3^{*2}}\right] \end{aligned} \tag{2.14}$$

Here, the pressure gradient and wall-normal Reynolds stress are scaled against a term of order L/δ they are significant. For a high Reynolds number flow the viscous terms are insignificant in comparison to the pressure gradient and wall-normal stress term. Thus, on the basis of the relative insignificance of small terms in a high Reynolds number turbulent boundary layer, the dimensional x_2 momentum equation is simplified and approximated as:

$$0 \approx -\frac{1}{\rho}\frac{\partial P}{\partial x_2} - \frac{\partial \overline{u_2'^2}}{\partial x_2} \tag{2.15}$$

Together, equations 2.10, 2.12, 2.15, and 2.13 are referred to as the "boundary layer equations."

Now that we have fully discussed the approximations made for the turbulent boundary layer, we can discuss characteristics of the boundary layer and quantities typically used to describe its properties. If a control volume is taken across an infinitesimal streamwise surface, which extends in the wall-normal direction, we can see that the boundary layer must follow the no-slip condition at the wall and follow a smooth gradient until the velocity reaches the free stream conditions at the boundary layer edge. Due to viscous effects, the velocity gradient through the boundary layer control volume also results in a loss of momentum and mass when compared to that of an ideal, inviscid flow. These losses are represented as the momentum thickness, θ and the displacement thickness, δ^*. These terms appear in the integral form of

the wall-parallel momentum equation given in equation 2.16a.

$$\frac{\partial \theta}{\partial x_1} + \frac{1}{U_e}(2\theta + \delta^*) = \frac{C_f}{2} \tag{2.16a}$$

Where

$$\theta = \int_0^\delta \left(1 - \frac{\overline{U_1}}{U_e}\right) \frac{\overline{U_1}}{U_e}\, dx_2 \tag{2.16b}$$

And

$$\delta^* = \int_0^\delta \left(1 - \frac{\overline{U_1}}{U_e}\right) dx_2 \tag{2.16c}$$

Where the overline indicates time-averaged values. Additional terms appearing in the momentum integral equation are the skin friction, C_f and the edge velocity U_e. Further discussion regarding the momentum integral method to determine skin friction from experimental mean velocity profiles is provided in section 2.1.7. Both δ^* and θ can be physically interpreted as the loss of momentum and the displacement of mass, respectively, in the viscous flow. Essentially, they are the distances that the inviscid fluid surface would need to be *displaced* to produce the same mass and momentum as the viscous flow. This concept is depicted in Figure 2.2, where the red shaded regions show equivalent mass and momentum properties between the viscous and displaced inviscid profiles. Aside from understanding the physical impacts of shear stresses on a flow near a surface, this comparison to the equivalent invsicid flow behavior allows us to fairly compare the mass and momentum losses due to varying external perturbations of the boundary layer.

2.1.4 Characteristics of a Turbulent Boundary Layer

The following section will discuss the characteristics of turbulence and the turbulent boundary layer. At a sufficiently high Reynolds number, referred to as the critical Reynolds number, the boundary layer flow transitions from laminar (i.e., flow in which streamlines follow a smooth pattern) to turbulent (i.e., flow with an increased presence of random, vortical motion) as shown in the schematic of Figure 2.3. The Reynolds number is defined as the ratio of the inertial forces to viscous forces and is a function of the characteristic length, L, and velocity U.

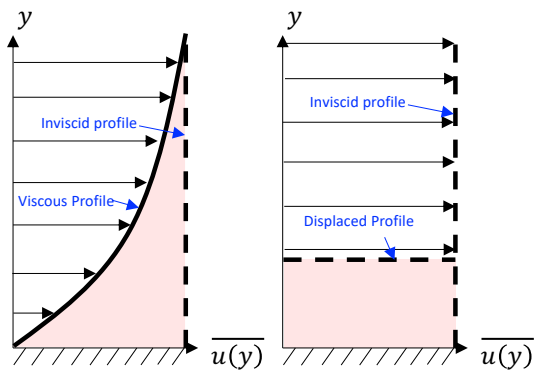

Figure 2.2: Schematic of a mean velocity profile in a boundary layer (left) against the equivalent "displaced" inviscid profile (right). Red shaded regions have equivalent mass and momentum properties between the viscous and displaced inviscid profiles.

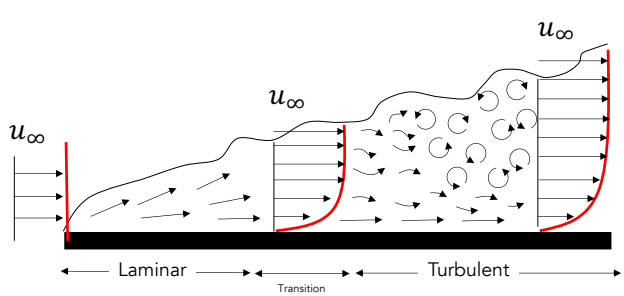

Figure 2.3: Schematic of a streamwise developing boundary layer on a flat plate showing the transitions from laminar to turbulent flow.

$$Re = \frac{UL}{\nu} \tag{2.17}$$

In boundary layer application, the characteristic Reynolds number is often written in terms of the integrated boundary layer parameters described in equations 2.16b and 2.16c. For instance, a momentum-thickness based Reynolds number would take the characteristic length-scale as θ, and the characteristic velocity to be the local freestream velocity.

In general, the distinctive qualitative characteristics of turbulence are:

1. General swirling nature of the flow due to a collection of eddies, which are coherent lumps of vortical fluid.
   (a) These eddies can vary in size and velocity magnitudes over the range of the turbulent boundary layer. The relation of the size and velocity are often related to Townsend's attached eddy hypothesis which states that turbulent eddy sizes are proportional to the distance from the wall [86].
   (b) There is mixing between regions, thus resulting in the transfer of mass, momentum, and energy on a much larger scale than laminar flow [54].
2. The region of turbulence and the inviscid freestream are still distinct and can be described using the boundary layer equations.
3. Turbulence is an unsteady process, and is stochastic and random, and is fundamentally three-dimensional [76].
4. Turbulent boundary layers have higher skin friction than laminar boundary layers are generally more unstable. Because of the higher shear near the wall, the mean velocity profiles in a turbulent flow have a much steeper velocity gradient in the boundary with wall-normal distance [54, 76].

The behavior within a turbulent boundary layer is dependent on the scales and magnitudes of structures developing in the inner and outer regions. The range of scales is set by the Reynolds number; the higher the Reynolds number, the wider the separation between the smallest and largest scales of turbulence. The smallest of the scales are known as the Kolmogorov scales or the "dissipative scales," for which the viscous effects completely takeover and the turbulent kinetic energy is dissipated into heat [70]. On the larger end of the scale

spectrum are eddies that are within the "energy containing range," and for a boundary layer, the largest lengthscale is on the order of multiple boundary layer thicknesses. Between the energy-containing and dissipative scales is the "inertial subrange" where the motions are primarily determined by inertial effects [70]. The interaction and production of eddies of various scales has been a topic of interest since the recognition of energy content based on scale size. Lewis Fry Richardson was the first to relate the size of the eddies to their energy distributions, an idea which is referred to as the "energy cascade" [53, 74]. Some of the early experiments of flow between concentric cylinders by G. I. Taylor (1923) revealed vortical structures that were characterized by the viscous and inertial forces within the boundary layer. An intermediate lengthscale, known as the Taylor microscales, are used to describe eddies where viscous forces dominate over inertial forces [58, 70]. Although the various scales of turbulence are dispersed throughout a boundary layer, various studies have found that the dominant scales of turbulence occurring within each region of the boundary layer can be scaled as a function of wall distance, an idea that is known as Towsend's attached eddy hypothesis [87]. The smaller scale eddies are greatly affected by viscous stresses which are dominant in regions near the wall, but wall conditions, such as roughness, can exacerbate the total stresses by increasing the overall wall shear stress [32]. The extent to which the wall condition continues to affect the outer regions is not yet entirely understood, however a few studies suggest the viscous forces remain dominant above the roughness canopy and rather than be a sole function of wall distance, is more so a function of the dominance of inertial forces [46, 62]; this will be explored in further detail in section 2.2. The majority of the energy within a boundary layer is contained within the larger eddy structures which are significantly influenced by the inertial forces such as pressure gradient, which in an equilibrium turbulent boundary layer has a pronounced and immediate impact to the momentum, and resulting eddy structures, of the inner region. Part of the lack of concrete understanding of the dispersion of scales and their impacts on the overall energy distributions derives from the difficulty in directly measuring the whole range scales due to the spatial resolution limitations of experiment hardware. Several investigations, including one completed as part of the present dissertation work, have found that the spatial resolution limitations of experiment hardware can inadvertently misrepresent the true range of separation of dissipative and the energy containing scales, simply because the hardware is not able to capture the energy contained below the limits of its resolution [34, 56, 72, 80].

2.1.5 Classes of Turbulent Eddies

The previous section introduced the idea of the "energy cascade" which suggests a distribution of energy that depends on the size of the eddy structures. A physically intuitive method to understanding turbulent flows is to observe and analyze the response of coherent structures to the developing flow fields, and how the various size of structures interact with each other to either contribute to or break down the energy containing structures. The hierarchy of eddy classifications is a qualitatively useful mechanism when depicting the range of turbulent scales within a boundary layer. The most distinctive of these eddy shapes is the horseshoe vortex, first introduced by Theodorsen [86], which characterized by an arch shaped vortex filament, where the legs of the filament are oriented parallel to the flow direction. Depending on the exact size, elongation, and separation of the legs creating the arch, this feature shape has been dubbed by many terms including the "hairpin vortex," as shown in Figure 2.4. The flow visualization work by Robinson [75], Kline [52], amongst others, have shown the dominance of hairpins in the wake or outer region of the boundary layer, thus associating these structures as the larger, energy containing features. The concept of the hairpin vortex has since been evaluated and experimentally and computationally exhibited in turbulent flows [2, 22, 28, 38, 38, 50, 60, 92]. The hairpin paradigm entails a streamwise/wall-normal cross-section of the flow, where the hairpin is characterized by a compact vortical region (the head), a region of ejection (i.e., Q2 flows in quadrant analysis) perpendicular to the plane of the vortex head, and a low-speed streak, parallel to the flow direction [1, 2, 50]. Low-momentum, "quasistreamwise" vortices exist in near-wall regions, followed by a mixture of both features in the logarithmic layer. The Reynolds shear stresses play a huge role in the hierarchy of hairpin packets appearing in the turbulent boundary layer; thus, they largely follow the parameters associated with the inner and outer regions. For instance, within the hairpin paradigm, there exists the "horseshoe" vortex with a much larger, wider head, that gets elongated by shear stresses into streaks with lower streamwise momentum into a shape resembling the hairpin vortex closer to the wall; the evolution of which is seen in Figure 3 [2]. Yet, as alluded earlier, the identification of the hairpin seems a bit arbitrary and up for judgement, and the exact development of these flow features remains to be universally agreed upon. Thus, quantitative identifications of these vehicles of momentum transport and TKE are necessary, such as model order-reducing methods. Turbulent eddies are the principal mechanisms for momentum transport via Reynolds shear stresses and produce and dissipate turbulent kinetic energy (TKE).

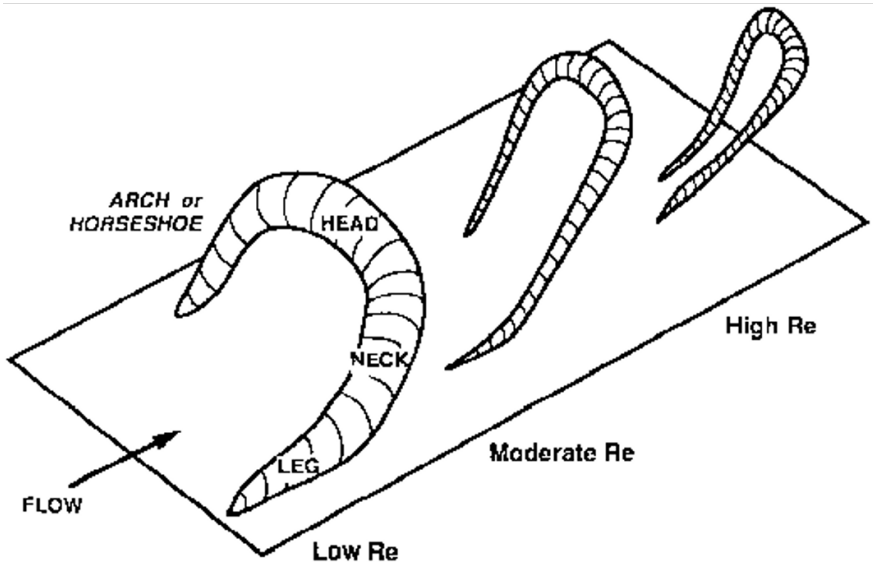

Figure 2.4: From left to right, transition of a horseshoe vortex to a hairpin vortex. From Head and Bandyopadhyay [39]

The mechanisms generating these structures have been widely discussed in literature. Zhou et al.[93] suggests that initial hairpin vortices are formed by a self-induced "kinks" in the flow which then connect and generate the secondary and tertiary structures. Smith et al. [78] refers to this behavior as "offspring" vortices and that low-speed streaks do not contribute to the development of the hairpin vortices. However, there are contrasting opinions on the source of vortex generation. Jimenez & Pinelli [45] use DNS to show that the instability and subsequent break-up of low-speed streaks result in the generation of streamwise vortices near the wall. Regardless of the agreement between these studies, the common theme is that the generation of streamwise vortices appears to be independent of the outer flow conditions, however the scale and distribution of the vortices are dependent on external influences [49]. Recent studies of turbulence structures have attempted to identify flow structures based on energy signatures using spatial and temporal correlations of the velocity field. Principal component analysis such as proper orthogonal decomposition (POD), spectral POD (SPOD), and linear stochastic estimation (LSE) have been performed on turbulent boundary layers showing energetic structures corresponding to large scale motions [36, 61, 89].

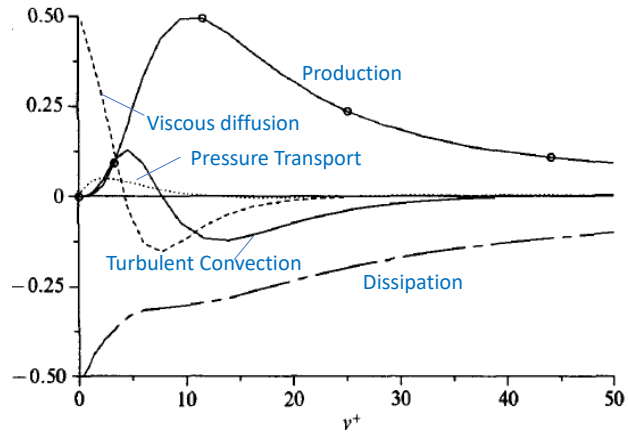

Figure 2.5: TKE budget in a flat plate smooth wall turbulent boundary layer. Adapted from Spalart [81]

2.1.6 Turbulence Equations for Stress and Transport

As shown in section 2.1.3, it is convention to treat the boundary layer equations in their Reynolds decomposed form due to the unsteady nature of turbulence, thus primarily dealing with the mean and fluctuating components of the velocity and pressure. This decomposition resulted in the Reynolds-Averaged Navier-Stokes (RANS) equations shown in equations 2.7 and 2.8. The time evolution of the Reynolds stress transport reveals the energy budget due to various forces related to turbulence production, dissipation, and transport. The transport equation is derived from the Navier-Stokes by subtracting the RANS equations and taking the correlation with velocity. The exact Reynolds stress transport equation is as follows:

$$\underbrace{\frac{D\overline{u_i u_j}}{Dt}}_{\text{Mean Convection}} + \underbrace{\frac{\partial}{\partial x_k}\overline{u_i u_j u_k}}_{\text{Turbulent Convection}} = \underbrace{-\overline{u_i u_k}\frac{\partial U_j}{\partial x_k} - \overline{u_j u_k}\frac{\partial U_i}{\partial x_k}}_{\text{Production}} + \underbrace{\nu\nabla^2\overline{u_i u_j}}_{\text{Viscous Diffusion}} - \underbrace{-\frac{1}{\rho}u_i\frac{\partial p}{\partial x_j} + u_j\frac{\partial p}{\partial x_i}}_{\text{Pressure Transport}} - \underbrace{2\nu\overline{\frac{\partial u_i}{\partial x_j}\frac{\partial u_j}{\partial x_k}}}_{\text{Dissipation}} \quad (2.18)$$

The balance between the production and dissipation terms are crucial in differentiating an equilibrium and non-equilibrium flow, where in the former, the two components are equivalent, and the net rate of energy gain or loss is zero.

The TKE balance for a turbulent smooth-wall flat plate is shown in Figure 2.5. It is interesting to note that the peak dissipation occurs near the wall, and the peak production occurs in the inner regions of the boundary layer. As we will see in the following sections, the outer region flow conditions appears to move the production peak location within the boundary layer, and overall, the production magnitudes are dependent on the near-wall conditions.

2.1.7 Skin Friction on Smooth Walls

The skin friction is arguably one of the most important parameters describing the growth of the boundary layer. Obviously, a direct measurement of skin friction is preferred, but not always feasible, especially in the case of flows with roughness. Oil flow inferometry, Preston tubes, and other instruments have been used in flow studies [25, 40, 67]. However, these methods are either intrusive, or not feasible with roughness. Thus, an analytical method of computing skin friction using experimental velocity measurements is necessary. Several approaches are explored in literature to determine the skin friction using analytical methods [11, 14, 17, 24, 30, 67, 68, 91]. One is using a direct manipulation of the integral form of the conservation of momentum (equation 2.16a). For turbulent flows in zero or mild pressure gradient, the conventional Clauser-chart method is often implemented. This method takes advantage of the law of the wall to regressively fit mean velocity profiles to the logarithmic region. Often empirical fits of the law of the wall such as the Spalding curve and the Musker profile are used in the Clauser-chart method [24, 64, 83]. However, this method fails in strong-pressure gradient conditions, often under-predicting results, and yields unsatisfactory results for non-equilibrium conditions [24]. As will be discussed in the later sections, conventional methods of skin friction derivation using regression fits often fail in the presence of strong and/or non-equilibrium flow conditions. [91] suggest an analytical method making use of Reynolds shear stress profiles and streamwise gradients that applied to a direct manipulation of the Reynolds-averaged streamwise momentum equation. This method has been shown to result in accurate skin friction estimates applied to flows on rough and smooth walls and in pressure gradient [91].

2.2 Rough Wall Turbulent Boundary Layers

Although the number of studies regarding smooth wall turbulent boundary layers are greater than those in rough wall turbulence, real flows of practical interest are rarely considered hydronamically smooth due to even macroscopic surface deficiencies or the build-up of natural roughness such as icing on an aircraft wing or biological debris on ships and wind turbines. Roughness can contribute to increased drag and unwanted noise due to higher pressure fluctuations. Thus, understanding the turbulent flow behaviors in flows with roughness can provide insight on bettering vehicle design and operation under rough conditions. This section provides insight on the current knowledge of the behaviors of turbulent boundary layers in rough wall conditions. The earliest peer-reviewed research regarding rough wall turbulence is by Johann Nikuradse and his pipe experiments [66]. In these experiments, Nikuradse explored the effect of different sand-grain surfaces on the behavior of a turbulent boundary layer. He established a quantity referred to as the "effective sand-grain roughness," that would essentially serve as a comparison factor for other roughness configurations. This parameter is a measure of the roughness disruption to the mean velocity profiles as shown in the comparison of smooth and rough wall mean velocity profiles in Figure 10. This disruption is accounted for in the modified law of the wall for roughness given as:

$$U^+ = \frac{1}{\kappa} ln(y^+) + C - \Delta U^+ \tag{2.19}$$

Where ΔU^+ is a downward shift of the mean velocity profile normalized on inner coordinates, corresponding to the increase in skin friction (see the shift of the rough wall mean velocity profile with respect to the smooth wall profile in Figure 2.1). This term, referred to as the roughness function was introduced independently by Clauser [20] and Hama [37] is also written in terms of the effective sand grain roughness as:

$$\Delta U^+ = \frac{1}{\kappa} ln(k_s^+) - 3.5 \tag{2.20}$$

k_s^+ is also used to define the roughness Reynolds number which quantifies the extent to which the roughness disrupts the flow and is defined as follows:

$$k_s^+ = k_s u_\tau / \nu \tag{2.21}$$

Typically, a roughness Reynolds number, $k_s^+ < 5$ is considered as a smooth flow indicating that the viscous sublayer is undisturbed by the roughness effects. The point at which the roughness effects such permeating to the logarithmic region, typically occurring when $k_s^+ > 50$, the flow is considered to be fully rough. In between these conditions, the flow is considered as transitionally rough where molecular viscous effects and the presence of roughness both have an impact on the flow behaviors [46, 73]. An in-depth review of the effects of roughness are summarized in papers by Jiménez [46] and Raupach et al. [73]. However, these reviews do not consider the effect of pressure gradient and external conditions outside of a constantly rough regime. Like a smooth wall boundary layer, a rough wall boundary layer can be divided into regions depending on the structure scaling and flow behaviors. In the direct vicinity of the roughness layer, often referred to as the roughness canopy, the flow behaviors are largely a result of the flow interactions shedding off the different roughness elements. Above the roughness canopy, several studies have shown that the roughness effects are confined to the inner region of the boundary layer, above which the flow is independent of the roughness, and behaves as a smooth wall outer region flow, aside from setting the magnitude of length and velocity scales [30, 31, 32]. This concept is referred to as the "wall similarity hypothesis" and was first introduced by Townsend [87]. The measure of the point at which the roughness ceases to influence the boundary layer structures is disputed. Studies by Raupach et al. [73], Flack et al. [32], and Jiménez [46] suggest that the wall similarity is a function of roughness geometry and distance from the wall, typically suggested as $5k_s$. Other studies seem to suggest more fundamental dependency from the momentum integral equations 2.16a. Although there exists several studies that contradict the principle of wall-similarity due to differences in the mean velocity defect and structures appearing in the outer region and in which case there are challenges to modeling capabilities specific to rough wall boundary layers [8, 11, 55]. For flows in pressure gradient and with roughness, studies have shown that wall-similarity continues to hold as the pressure gradient effects are typically affecting the outer regions of the boundary layer [18, 19, 68]. Perry and Joubert [68] demonstrate the effectiveness of a similarity defect law to be a function of the roughness Reynolds number. In the experiments discussed in this paper, cylindrical k-type roughness is used, designed in collaboration with Dr. Joseph Katz at Johns Hopkins University. In experiments of different roughness shapes, densities, and orientations, Joseph [47] demonstrated that the main geometrical factors influencing a rough flow were the roughness height and density. Research has shown that near-wall structures in a rough wall boundary layer are dependent on the sparseness ratios (ratio of roughness element frontal, A_f projected

area over its planform area, A_w) defined in equation 2.22 below of the roughness elements [9, 10, 39, 47].

$$\lambda = \frac{A_f}{A_w} \tag{2.22}$$

Although carrying higher magnitudes of energy, the structures appearing in the outer region of the rough wall appears to be consistent with the wall-similarity hypothesis, in that the large-scale structures of the rough wall boundary layer follow the same behaviors as those in a smooth wall boundary layer [31, 47, 55, 57, 84, 85]. Typically, these are large-scale hairpin vortices. Thus, in the case of flows with pressure gradient, the external forces largely dictate the structures appearing in the outer regions.

2.3 Turbulent Boundary Layers in Pressure Gradient

This section will describe the behaviors differentiating flows in favorable, adverse, and zero pressure gradient. The distinction between an equilibrium and non-equilibrium flow conditions is also introduced and how these terms relate to flows with a unidirectional or bidirectional pressure gradient. Current literature is biased towards reviewing pressure gradients evolving with the same sign or zero pressure gradient conditions, the latter for which has been thoroughly reviewed. Although, relevant flows over vehicles of interest often experience the effect of compounding or mixing pressure gradient conditions. Thus, an improved, fundamental understanding of flows with varying pressure gradient is necessary.

The concept of quantifying the pressure gradient can be traced to Clauser [20] who first established the parameter β which is a measure of the magnitude of the pressure gradient applied on the flow.

$$\beta = \frac{\delta^*}{\tau_w}\frac{dp}{dx} \tag{2.23}$$

It is the ratio of the pressure and the shear force acting on the boundary layer defect. For $\beta < 0$, flows are in a favorable pressure gradient (FPG). For $\beta = 0$, flows are in zero pressure gradient (ZPG). And for $\beta > 0$, flows are in adverse pressure gradient (APG). Clauser established that for a constant parameter, the outer-region of the boundary layer

can be self-preserving, and thus considered to be in equilibrium [20]. The question of self-similarity across the entire boundary layer comes into question, and thus results in Clauser creating a criterion that the similarity laws are preserved for high Reynolds numbers and would thus encompass a large area of the boundary layer [20]. Discussions of self-similarity and equilibrium conditions in turbulence are explored further in section 2.4.

2.3.1 Zero-Pressure Gradient (ZPG)

The simplest of flows is the zero-pressure gradient turbulent boundary layer, often synonymous with flow over a flat plate, and is considered a canonical case to which all non-equilibrium conditions are frequently compared. One of the most well-known studies of the flat plate boundary layer was explored by Phillip Klebanoff in 1955 who used hot-wire anemometry to measure the turbulent energy, shear stress, and dissipation, with which he argued against the concept of local isotropy [51]. Klebanoff's anisotropy factors were continued to be used in modelling and empirical efforts [35]. The flat plate boundary layer follows the behaviors already outlined in section 2.1.2 describing boundary layer turbulence in its canonical form. The inner region contains the most productive and dissipative energy due to the interaction of the smallest scales of turbulence and the cascade of energy from the large outer region vortices [23]. Work by De Graaff and Eaton [23] provided the research community with a well-documented database of an equilibrium, high Reynolds number, smooth wall, flat-plate turbulent boundary layer data using laser-Doppler anemometry (LDA). Their work showed Reynolds number independency of inner scaling for the turbulence stresses, mean velocity, and TKE, as well as singled out the classical log law fitting to provide a universal profile of the mean velocity in the inner region with a significant momentum Reynolds number range, suggesting that for the ZPG boundary layer, the log law is inferior only to an accurate, independent, direct measurement of the shear stress [23].

2.3.2 Favorable Pressure Gradient (FPG)

A favorable pressure gradient is characterized by the decreasing coefficient of pressure and increasing velocity field gradients, resulting in an increase in wall shear stress. Large enough favorable pressure gradients can accelerate the flow to an extent that the flow relaminarizes [49]. Generally, on inner-scalings, the pressure gradient region of major influence tends

exhibit variations in the outer regions of the turbulent boundary layer. In any pressure gradient flow, a feature of significant interest is the existence of "organized eddies" that bring high-momentum fluid to the wall and eject low momentum fluid from the wall. Finnicum and Hanratty [29] also found that the difference of net turbulence production in the viscous wall region between the favorable and zero pressure gradient conditions was negligible. This implies that the difference between the dissipation and the production in the boundary layer remains constant, except for at the peak, where the inertial forces in the FPG dictate the level of production. Overall, the FPG case has a lower turbulence peak in the outer regions of the boundary layer than flows in either zero or uni-directional adverse pressure gradient due to the higher inertial forces [29].

Investigations by several researchers have shown that with the Reynolds shear stress decreases in most of the outer layer, and collapse in the outer regions when scaled on outer coordinates, but the main discrepancy comes near the wall [49]. Near the wall, there is an increase in the Reynolds shear stress in the downstream parts of the favorable pressure gradient. An increase of turbulence near the wall indicates slow diffusion of near wall turbulence from the outer region [49]. The existence of low-speed streaks contributing to the turbulence dynamics in the wall-region have been observed in several FPG studies [42, 82]. Hutchins and Marusic [41] observed that the FPG has much longer "meandering" streaks in the logarithmic region when compared with the ZPG flows, consistent with the instantaneous velocity fields shown in the study by Joshi and Katz [48]. In a study of boundary layers in FPG, Joshi et al. [49] found that although the locally-scaled Reynolds stress profiles were Reynolds number independent and were weaker than the ZPG stresses, the un-scaled stresses showed higher magnitudes of turbulence near the wall and lower magnitudes in the outer region. This was due to higher streamwise and wall-normal velocity gradients that resulted in weaker turbulence structures when compared with the ZPG boundary layer. Structurally, in a favorable pressure gradient, the structures are more inclined and tend to remain near the wall, due to the distortion associated with inertial forces of acceleration [29]. Due to the higher acceleration, the FPG is also associated with large-scale ejections which contain horizontal trains of vortices. Although many studies exist on flows in a favorable pressure gradient, much of this work is in equilibrium or on the verge relaminarization [12, 15, 27, 38]. Existing literature have also discussed the transition from a FPG to APG, but there is an insufficient number of in-depth studies that have explored the opposite flow field, but they leave to question the concept of wall-similarity and criteria to evaluate the physical parameters relevant to non-equilibrium flows [7, 82].

2.3.3 Adverse Pressure Gradient (APG)

As adverse pressure gradients are typically considered as undesirable occurrences in flows of practical interest, as they are associated with an increase in flow instability, deceleration of flow, and higher drag. Some contrary behaviors are seen in the APG when compared with the FPG condition. For instance, mean flow is decelerated near the wall, thus decreasing the turbulent shear stress. In an APG, the large-scale turbulent structures appear more in the outer regions of the flow (as opposed to the FPG where most of the structures are small-scale and confined closer to the wall due to higher inertial forces). This is because in an APG, the scales and structures are more energized throughout the boundary layer [38, 38]. The APG profile is distinguished by the presence of a second turbulence stress peak in the logarithmic region. Aside from mild pressure gradients, several studies have found that the APG effect on mean velocity propagates down to the logarithmic region, at which point classical regression fits using Clauser method are no longer valid for computations of skin friction [13, 59]. The adverse pressure gradient mean velocity can be characterized by three regions due to theoretical and experimental grounds [69, 77, 86], which is consistent with TKE peaks occurring with distance from the wall [26]. In a study of constant ZPG, APG, and FPG, Harun et al. [38] showed shows that for all pressure gradient conditions, the production levels rapidly decrease in the inner region. In an APG, the large scales in the outer region have little impact to the near wall Reynolds shear stress [16, 86]. Several studies have shown that the turbulent kinetic energy in the outer region of the boundary layer is increased in an APG [7, 38, 89]. This indicates that the large-scale motions have not changed in behavior or character but have simply increased in strength and quantity in the APG [38].

2.4 Non-Equilibrium Turbulent Boundary Layers

To understand the concept and behaviors of flows in non-equilibrium, it is useful to first establish what is considered to be a flow in equilibrium. Equilibrium conditions are idealized states in which flow properties are only dependent on local flow conditions, and evolution of mean velocity and turbulence quantities with streamwise position can be collapsed by scaling on the basis of self-similarity. In an equilibrium flow, the transport of kinetic energy reduces to an equation where the production and dissipation energy terms are equivalent (refer to

equation 2.18). In the non-equilibrium flow, the imbalance of the advection and production terms against the dissipative forces results in an increase of the mixing length near the wall. The local flow conditions are now also dependent on the history of conditions that the flow has experienced, of which the effects persist and affect the local flow behaviors. Several studies have shown that given sufficient streamwise distance and uninterrupted boundary conditions, a non-equilibrium flow will eventually relax towards equilibrium conditions [4, 5, 6, 43, 44]. Although the relaxation time is somewhat dependent on the streamwise timing of the perturbation within the developing flow, studies of roughness impulses on a flat plate have established that distance to be on the order of 10δ [3, 5, 44, 79]. In a non-equilibrium pressure gradient, Bobke et al. [13] found this streamwise length requirement for self-preservation to be 6.5δ.

The Clauser pressure gradient parameter β (equation 2.23) has often been used to be a measure of the non-equilibrium pressure gradient flow behaviors in the boundary layer. Clauser suggested that if the pressure gradient non-dimensionalized on shear stress remains constant, then the flow is in equilibrium conditions [20]. Townsend [86] and Mellor and Gibson [63] followed Clauser's work and added an additional criterion to describe an equilibrium flow as having a power law relation for the edge velocity developing on the boundary layer. However, in studies of bi-directional pressure gradient, Fritsch et al. [33] and Vishwanathan et al. [89] have shown the existence of history effects downstream of pressure gradient switches. This is evidenced by a delayed response to the pressure gradient switch (i.e. integrated boundary layer curves show a crossover that occurs downstream of the PG switch), and in the turbulence stresses with response to peaks of Reynolds shear stresses occurring at different points in the boundary layer. Vinuesa et al. [88] recognized the existence of history effects, but noted that the effects from APG must be differentiated from the "well-behavedness" of the wind tunnel flow and claim that this finding is only relevant for relatively simple flows. In the study of a non-constant APG, Bobke et al. [13] showed that the boundary layer does not necessarily develop based on a local pressure gradient condition, but rather as a function of the streamwise pressure gradient development. Essentially, they found that the inner layer seems to adapt to the local pressure gradient conditions, but the outer region statistics continue to show behavior influenced by the upstream station.

For the most part, studies that have explored the effects of pressure gradient signs independently [23, 26, 29, 35, 49] or of ZPG and FPG flows transitioning to APG [7, 65, 82]. These studies, along with the current work, have consistently seen an increase of turbulence stresses

in the outer region of the boundary layer when the flow transitions to an APG. Overall, little work has provided an in-depth exploration of the transition from a positive pressure gradient. As mentioned in section 2.2, the measure of non-equilibrium conditions in roughness is the satisfaction of wall-similarity such that the outer regions of the boundary layer collapse to the equivalent conditions in a smooth wall flow. A number of studies have shown that roughness effects remain independent of pressure gradient, thus satisfying the question of wall-similarity. But enough studies, such as that by Aubertine and Eaton [7] suggest that the current evaluation of wall similarity to deem a flow in equilibrium is insufficient, and addition parameters relating to the pressure gradient conditions are necessary.

2.5 Summary and Gaps in Literature

The summary of literature thus far has shown that there are many parameters that affect the behavior of the turbulent boundary layer, namely wall conditions (i.e. roughness) and pressure gradient. These variables have been independently investigated in great capacity, but flows of practical interest are more complex and often consist of the compounding influences of varying pressure gradient histories and wall conditions. When a flow is impacted by both local and upstream flow development, the flow is considered to be in non-equilibrium. There is a lack of sufficient understanding on the compounding effects of both roughness and non-equilibrium pressure gradient on the velocity field of a turbulent boundary layer.

The current array of literature has provided a strong foundational understanding of the independent variables; it is commonly accepted that, compared to the canonical zero pressure gradient flow (i.e. flow across a smooth flat plate), the effect of an adverse pressure gradient is to increase the turbulence intensity and outer layer scaling parameters whereas the tendency of a favorable pressure gradient is to accelerate the flow, increase the shear velocity, and reduce the turbulence intensities such that the flow approaches relaminarization.

It is also commonly observed that the effect of roughness is to increase the magnitude of the boundary layer and its characteristic properties compared to the smooth wall. But, there are disputed opinions regarding the comparative differences between the wall conditions by means of the of the wall-similarity hypothesis, which is the notion that the extent of the roughness effects are limited within the immediate vicinity of the roughness elements and that outside of this region, the boundary layer behaves as an equivalent smooth wall with

the same outer layer properties. Much of this debate comes from differing criteria for qualifying flow regimes and roughness properties to which the wall-similarity hypothesis can be applied. Some studies suggest bounds based on the physical geometry and distribution of the roughness element with respect to the overall boundary layer thickness, versus other studies suggest scale ratios based on the characterization of the flow itself. The flow characterizing parameter for rough walls is often taken to be dimensionless effective sandgrain roughness parameter k_s^+ based on the early studies of pipe flows by Nikuradse [66]. However, challenges arise in practice as it is difficult to identify an *a priori* estimate of the k_s parameter given a roughness geometry, and in the absence of direct measurements of the wall shear stress, introduces uncertainty when indirectly determining its magnitude. The basis of criteria for flow comparison between a rough and smooth wall is also unclear. There is also insufficient discussion on non-local dependencies for both rough and smooth wall flow development.

In addition to an understanding of these fundamental flow behaviors, there is a lack of sufficient research regarding limitations of multi-point measurement techniques of turbulence. Particle image velocimetry (PIV) is increasingly becoming a standard measurement technique for turbulence studies, thus an assessment of the bias uncertainties associated with under-resolved measurements is necessary. Spatial resolution limitations have been found to attenuate measurements of the turbulence statistics. Also, the comparative effect to measurements made over a rough wall versus a smooth wall are not discussed in detail. In an anisotropic turbulent boundary, the scales in the dominant streamwise direction of correlation are much larger versus in the wall-normal directions, and therefore must have an impact on the measured quantities. Variations in component-wise attenuation could result in misinterpretations of comparative statistics between flow conditions. It is unclear whether the smooth and rough wall discrepancies come from variations in the fundamental flow behavior, or if there are false judgements in the measurement of the flow field. For the present study, this has major implication when comparing turbulent statistics in varying local Reynolds numbers and wall conditions.

There are three main gaps in the literature that are addressed in this dissertation:

1. An improved fundamental understanding of the combined effects of roughness and non-equilibrium pressure gradients on the velocity fields.

2. The limitations of practical measurements in representing true turbulence statistics for comparative purposes.

3. The validity of the wall-similarity hypothesis for rough wall flows with varying pressure gradient histories and comparative differences between rough and smooth wall turbulence characteristics.

Chapter 3

Spatial Resolution Limitations of Particle Image Velocimetry in High Reynolds Number Turbulent Boundary Layers

The contents of this chapter contain a manuscript in the Springer journal submission format that has been submitted and in-review for publication to the *Experiments in Fluids* journal. This chapter presents an investigation of the effect of under-resolved spatial fields measured with particle image velocimetry under-resolution on the magnitudes of the measured turbulence statistics.

Spatial Resolution Limitations of Particle Image Velocimetry in High Reynolds Number Turbulent Boundary Layers

Vidya Vishwanathan[1*], Daniel J. Fritsch[1†], William J. Devenport[1†] and K. Todd Lowe[1†]

[1*]Crofton Department of Aerospace & Ocean Engineering, Virginia Tech, 660 McBryde Hall, Blacksburg, 24060, VA, USA.

*Corresponding author(s). E-mail(s): vidya418@vt.edu; Contributing authors: dannyf96@vt.edu; devenport@vt.edu; kelowe@vt.edu;

[†]These authors contributed equally to this work.

Abstract

Particle image velocimetry (PIV) has become a standard technique in turbulence experiments for its non-intrusive ability to simultaneously measure multiple points in a flow field. However, inherent volume averaging of the interrogation windows as well as fixed limitations of camera spatial resolution and related hardware set the minimum and maximum scales of structures that can be resolved with this measurement technique. Resolution limitations present themselves as an attenuation of the measured turbulence statistics, seen particularly in the Reynolds wall-normal stress components. This experimental study investigates the impact of hardware-level resolution limitations on the resolved turbulence statistics of PIV measurements made of both rough and smooth wall turbulent boundary layers influenced by external pressure gradients. Velocity fields are measured with PIV using two lens magnifications; one with a baseline lens and one with the addition of a teleconverter lens to view the same flow-field with double magnification (i.e. a finer spatial resolution). A comparison of the turbulence statistics between the rough and smooth wall, components of velocity, and pressure gradient magnitudes are analyzed. The smooth wall turbulence data consistently show a much higher sensitivity to the spatial resolution, particularly for the wall-normal component, due to the smaller

eddy length-scales. A fixed camera resolution limits the measured range of scales which affects comparative magnitudes of turbulence for flows with different local Reynolds numbers. The rough wall data measurements show a variable sensitivity to the camera resolution depending on local Reynolds number and streamwise flow history. A statistical convergence study based on the anistropy of turbulence scales is necessary in experimental design for the study of turbulent boundary layers.

Keywords: Turbulent Boundary Layers, Particle Image Velocimetry, Pressure Gradients, Spatial Resolution

1 Introduction

One of the many challenges of experimental work in turbulence is accurately capturing the relevant physical phenomena occurring in the diverse length-scale ranges. Very often the limitations of measurement hardware restrict the resolution to which the behaviors of these turbulent features can be captured. Thus, a compromise is often made in the test setup to sacrifice the focus on fine-scale features in exchange for a larger measurement area or vice versa. This issue is especially relevant to multi-point, planar measurement techniques such as particle image velocimetry (PIV), where the pixel resolution and working distance of the camera and lens hardware prescribe the minimum and maximum extents of the size of resolved turbulence features. An attenuation of turbulence statistics due to coarse instrument resolution has been observed in many experimental studies, not just in PIV [1–4]. However, comparisons of data measured via PIV and single-point measurement techniques such as hot-wire anemometry (HWA) have shown that PIV requires a much stricter tolerance of resolution to match that equivalent in single-point measurement techniques, in part due to the finite-volume averaging done within the interrogation windows of the PIV images [3]. In fact, according to Saarenrinne et al. (2001) [5], in order to measure even 65% of the predicted true turbulent kinetic energy (TKE), any instrument spatial resolution needs to be on the order of 90η, where η represents the smallest of the dissipative structures known as the Kolmogorov scales. This criteria is very stringent, especially given current technological limitations for camera resolutions used in high Reynolds number experiments. This PIV specific resolution and volume-averaging issue concerning on resolving turbulence statistics is not a new problem. Gamba & Clemens (2011) determined that, without an anti-aliasing filter, the spatial averaging inherent of the PIV algorithm results in a rapid decrease of the energy spectrum, where the effects are more prominent in the higher wavenumber limits of the resolved spectrum [6]. The effect of control-volume size in measurements made with Doppler global velocimetry (DGV) (akin to the interrogation window size in PIV) by Saltzmann et al. (2021) showed similar attenuation in the higher wavenumber portion of their spectra, but concluded that the impact to

the larger scales was minimal and mostly depended on inherent measurement uncertainties [2]. Several studies have offered insight into correction methods, typically using computational fluid dynamics (CFD), usually in the form of direct numerical simulations (DNS), for a priori estimates of the flow behavior ([7–10]). However, these corrections often only address the large-scale component of velocity in zero or constant pressure gradient flows, which although useful, do not directly translate to the vast majority of non-equilibrium, anisotropic, and rough wall turbulence studies. In fact, very few investigations of spatial resolution effects on measuring rough wall flows exist, most recently by Gatti et al. (2022), who applied spatial filtering to mimic instrument resolution limitations to their DNS of a rough wall flow [11]. Although they did not explore the impacts to all stress components, the authors observed an attenuation of the streamwise Reynolds normal stress component when simulated with a coarser grid and concluded that existing methods for post-measurement correction are best applied for smooth wall flows [11].

As the range of turbulent scales increases at higher local Reynolds numbers, the energy-containing eddies become present in smaller scales, and a fixed instrument resolution may not be able to capture this increase in range. For flows with varying pressure gradients, such as over any curved geometry, a comparison of streamwise turbulence magnitudes may be distorted due to the inability to capture all relevant energy containing scales occurring at higher wavenumbers. A major gap in the understanding of the spatial resolution problem is characterizing the size of turbulence structures with Reynolds number, but also in each velocity component direction. In a turbulent boundary layer the streamwise convecting structures have a much larger energy presence than those occurring predominately in the transverse direction. This anisotropy is critical when considering Reynolds shear stresses that depend on the correct magnitudes in two velocity directions. From a purely logistical point of view, it may be impractical to adjust PIV camera lens configurations to account for all eddy scale ranges, especially for high Reynolds number experiments occurring in commercial-scale facilities, such as the one used in the present study, where the boundary layer thicknesses grow to ranges that necessitate a compromise between measurement area (to capture the large scale features) and small-scale resolution. Thus, an understanding of the limitations of PIV in measuring a variety of flow conditions is necessary to improve experiment design for turbulent boundary layer measurements.

This paper addresses the effects of PIV spatial resolution on the attenuation of turbulence statistics at various wall-normal positions within the logarithmic region of a boundary layer in both rough and smooth wall configurations. Turbulent length-scale variations along the boundary layer are compared with the minimum PIV spatial resolution to identify the wall-normal threshold where attenuation of the turbulence measurement becomes an impressed issue. The present investigation compares PIV data acquired with two different lens magnifications that are post-processed with the same PIV image processing parameters to address issues at the experiment setup and hardware level.

Constancy in post-processing parameters also reduces variations in overall uncertainty due to PIV window averaging schemes between the different experiment configurations. Data are measured over rough and smooth wall turbulent boundary layers with varying external pressure gradients to also characterize the effect of wall conditions. The effect of pressure gradient and the corresponding separation of turbulent length-scales due to varying local Reynolds number are investigated to provide further insight on the physical properties of the turbulent boundary layer requiring a finer resolution to resolve the energy statistics at a comparable level. In addition, the impact of the spatial resolution to the resolved features in both the streamwise and wall-normal directions are compared to improve experiment design for anisotropic flow measurements. The objective of this investigation is to offer an explanation of the physical anisotropic turbulence behaviors that cause the attenuation of statistics given a fixed spatial resolution in an attempt to provide a reference point for the setup of PIV camera lens configurations for turbulence measurements.

This paper is organized as follows. Section 2 provides details on the experiment configuration and the PIV databases presented in this study. Comparative results and analyses are presented in section 3. Finally, section 4 provides a conclusive summary of the investigation as well as comments on future outlooks of such a study.

2 Experimental Facilities & Method

2.1 Facility

All measurements discussed in this paper were performed in the Virginia Tech Stability Wind Tunnel (VT SWT). The VT SWT includes a $1.85 \times 1.85 \times 7.32\ m^3$ test section where the bounding walls consist of carefully leveled, modular aluminum panels, $0.61 \times 0.61\ m^2$ in size; this modular design allows the test section wall to be configured with custom instrumentation and wall conditions. The flow is tripped in the contraction, 3.54 m upstream of the test section coordinate origin (see Figure 1), such that the measured flow is fully turbulent and free from any transitional effects. Further information regarding the specifics of the wind tunnel facility and experiment configurations can be found in [12–14]. The coordinate system is set such that x is streamwise, y is wall-normal, and z is spanwise with corresponding u, v, w velocity components.

2.2 Pressure Gradient Conditions

A systematically varying family of bi-directional pressure gradients was generated on the measurement wall by a 0.914 m chord, full-span NACA 0012 airfoil that was placed at the center of the test section with the aerodynamic center located at the airfoil quarter chord at x = 3.45 m. The airfoil was rotated to three angles of attack, -10°, 0°, and $+12^o$ to investigate the impacts of favorable, zero, and adverse pressure gradients, respectively, on the resolved scales within the boundary layer given a consistent PIV measurement setup.

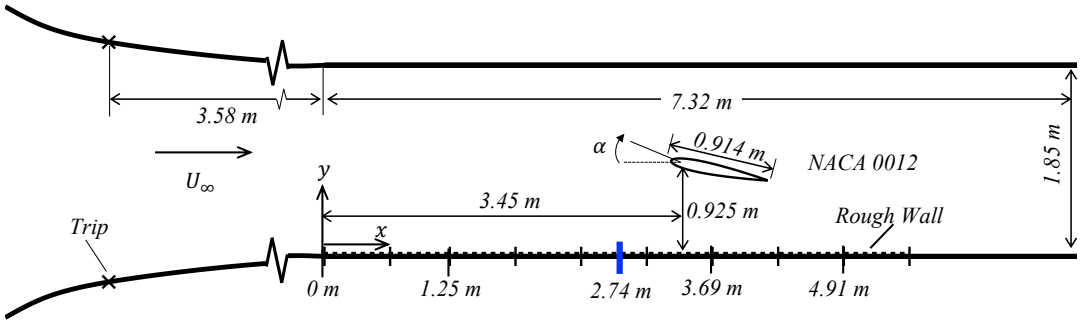

Fig. 1: Top-down schematic of the test section in experiment configuration. PIV measurements for both the magnified (MFOV) and full (FFOV) fields of view are taken at x = 2.74 m (station indicated as a blue line) for both the rough and smooth wall configurations.

PIV measurements were made at a streamwise station upstream of the airfoil leading edge at x = 2.74 m on the measurement wall (the lower wall in the schematic shown in Figure 1). The normalized pressure distributions as a function of the airfoil angle of attack for both the rough and smooth wall measurements are shown in Figure 2. Any deviations of the coefficient of pressure distribution between the wall conditions is attributed to the increase in drag on the rough wall which results in a streamwise drop in pressure along the test section. The flow was measured at a reference Reynolds number based on airfoil chord of 2 million, which corresponded to an inflow reference velocity ranging between 33 – 36 m/s at the time of data acquisition. The momentum thickness based Reynolds number, Re_θ varied between 14182 – 19228 for the smooth wall, and 24874 – 27395 for the rough wall. Specific flow parameters for each experiment and run configuration are also listed in Table 1.

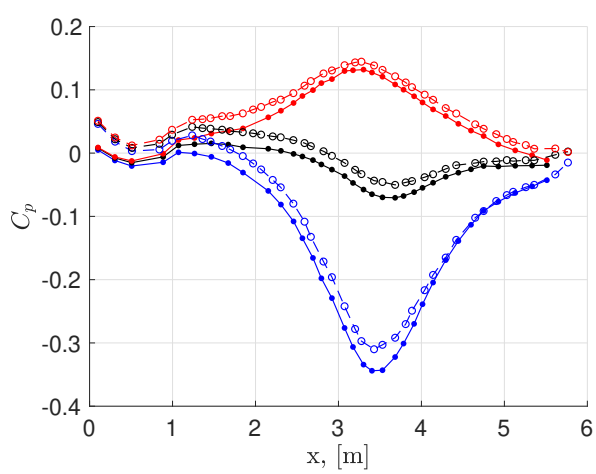

Fig. 2: Coefficient of pressure distribution across the test section wall at three angles of attack, -10°, 0°, $+12^o$. Pressures for the rough wall are shown as ○, and for the smooth wall as •.

2.3 Wall Conditions

The impact of spatial resolution limitations on the attenuation of turbulence statistics from both rough and smooth wall turbulent boundary layers was investigated. The smooth wall consisted of carefully leveled, bare aluminum wall panels for which the flow behaviors have have been investigated in detail in [15, 16]. The rough wall consisted of 2 mm tall and 3.14 mm diameter circular cylindrical roughness elements in a staggered pattern that were periodic on a $0.61 \times 0.61\ m^2$ scale. The distance between elements in the streamwise direction was twice that in the spanwise direction, as shown in Figure 3. The rough wall produced flows in the fully rough regime with roughness Reynolds number parameters detailed in Table 1. Skin friction values for the smooth wall measurements were estimated from the Clauser fit of the Spalding curve [17]. On the rough wall, the skin friction values were estimated using a modified Clauser method as established by Perry & Joubert (1963) [18]. Due to the inherent uncertainty associated with a regression fit of the logarithmic region for rough walls (see investigation by Vishwanathan et al. (2022) [19]), the skin friction estimates were computed from mean velocity profiles of a boundary layer rake that provided sufficient streamwise data such that the skin friction for the present results were interpolated to the streamwise location of the PIV measurements. This ensured a consistent normalization for comparison between the fields of view.

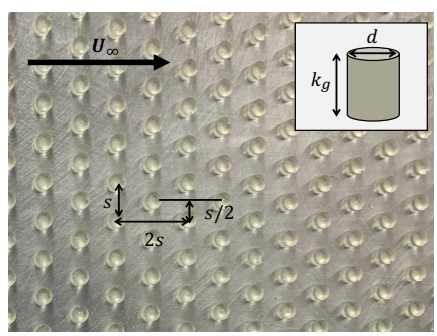

Fig. 3: Roughness geometry composed of staggered circular cylindrical elements where d = 3.14 mm, s = 6.93 mm, k_g = 2 mm. Adapted from Vishwanathan et al. (2022) [19].

2.4 PIV Setup and Processing Parameters

Data in the present work were obtained using stereoscopic PIV to investigate the effect of image spatial resolution limitations on resolved turbulence energy statistics. The PIV arrangement utilized two Phantom v2512 cameras (1280×800 pixels), each equipped with a Nikon AF-S Nikkor 300mm f/4D IF-ED lenses to provide the baseline "full" field of view (FFOV) of the entire boundary layer. For the magnified field of view (MFOV) configurations the

Table 1: Smooth and rough wall flow parameters at $x \approx 2.74$ m.

Wall Condition	α, [^{o}]	β	δ [mm]	θ [mm]	δ^* [mm]	$C_f \times 10^3$	Re_θ	k_s^+	ΔU^+	Δh [mm]	Symbol
Smooth	-10	-0.48	62.18	5.97	7.54	2.70	14182	-	-	1.09	×
							14348			2.27	○
	0	-0.11	65.59	7.01	9.07	2.53	15441	-	-	1.09	×
							15549			2.27	○
	12	0.58	77.80	9.47	12.75	2.19	19223	-	-	1.09	×
							19228			2.27	○
Rough	-10	-0.55	87.38	10.38	16.14	6.27	24874	429	11.27	1.09	+
							24884			2.29	□
	0	-0.20	97.79	11.35	17.96	5.48	24907	390	11.05	1.09	+
							24837			2.29	□
	12	0.47	109.33	13.71	23.76	4.25	27270	328	10.62	1.09	+
							27395			2.29	□

lenses were supplemented with Vivitar 2X Series 1 MC4 AF teleconverter lenses that multiplied the focal length of the base lenses by two times to increase their spatial resolution capabilities. The flow-field was seeded using an MDG Max 3000 APS fog-generator that uses a neutral fog fluid composed of a highly refined and filtered mineral oil base with particle diameters between $0.5 - 0.7\ \mu m$.

The seed particles were illuminated using a Photonics Nd:YAG dual cavity diode pumped solid state, high repetition rate laser emitting 532 nm light at 15 mJ/pulse, which was emitted as a laser sheet through and normal to the research boundary layer wall. Due to the staggered roughness pattern the laser was aligned in between the roughness elements at a 25.6^o angle with respect to the streamwise axis. The streamwise and spanwise velocity components were coordinate corrected in post-processing using a rotation matrix, with the assumption that the flow does not exhibit mean three-dimensional behaviors in the outer layer within the confines of the laser sheet. The laser sheet was aligned parallel to the streamwise axis for the smooth wall experiments. The cameras recorded $24,839$ realizations at a 1 kHz sampling rate. The raw images were processed in LaVision's DaVis10 using two initial passes of a 64×64 pixel^2 interrogation window with 50% overlap followed by two final passes of a 24×24 pixel^2 interrogation window with a 75% overlap. Both interrogation windows used 2:1 elliptical weighting schemes. These processing conditions were kept common across all conditions, and were selected after a detailed process to determine the DaVis10 processing methods that would retain relevant flow behaviors while removing spurious vectors. The selected processing parameters resulted in interrogation window resolutions (denoted as δh) of 1.09 mm for the MFOV and $2.27 - 2.29$ mm for the FFOV, which are detailed in Table 1 for each angle of attack and wall configuration.

3 Results

3.1 Mean Velocity and Turbulence Statistics

Comparisons are made of the turbulence statistics computed from the velocity fields of the magnified and full field of view PIV vector fields. The statistics discussed in this section are computed by ensemble averaging the PIV velocity fields across independent realizations. The statistics are also streamwise averaged across the image plane by noting the streamwise homogeneity within the PIV measurement field. The normalization parameters on inner and outer coordinates are listed in Table 1.

3.1.1 Mean Velocity Profiles

Figure 4 show the mean velocity profiles for the smooth and rough wall data normalized on inner and outer coordinates for the MFOV and FFOV data at varying pressure gradient conditions. Shear velocities for each data set are estimated using the Clauser method and modified Clauser method for the smooth

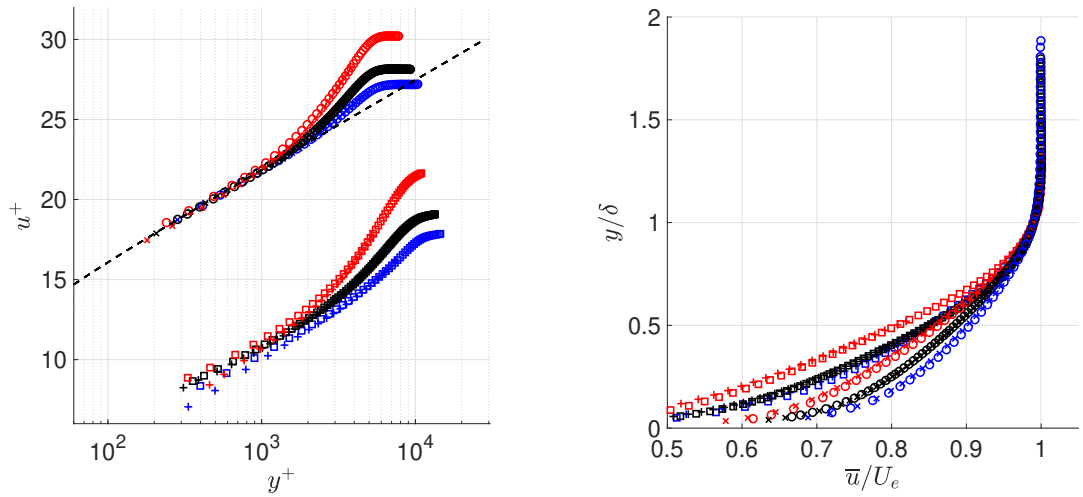

(a) (b)

Fig. 4: Mean velocity profiles for the smooth wall and rough wall in inner (a) and outer (b) coordinates. Data symbols listed in Table 1 with the Spalding profile shown as (- - - - -).

and rough wall data respectively, details for which are discussed in Fritsch et al. (2021) and Vishwanathan et al. (2022) [15, 19]. The collapse of the streamwise mean velocity profiles measured by both camera magnifications shows that the resolution limitations does not impact the magnitudes of mean velocity quantities. What is apparent however, is the limited wall-normal field of view with an increased magnification, which decreases the reach of outer-layer measurements. A fixed field of view across pressure gradient conditions means a greater portion of the outer boundary layer is measured for the comparatively thinner boundary layer formed under favorable pressure gradient conditions (blue curves) than for one under adverse pressure gradient conditions (red curves). For instance, with the MFOV configuration, the smooth wall APG data are measured up to a $y/\delta = 0.72$ versus $y/\delta = 0.90$ for the FPG conditions. With a thicker overall boundary layer thickness over the rough wall this distance is reduced further where the maximum measured distance from the wall in outer-coordinates decreases to only a $y/\delta = 0.52$ for the APG and a $y/\delta = 0.63$ for the FPG condition. This limitation is more obvious in the x-axis of the length-scale profiles shown Figure 10 and 11, which are discussed in detail in 3.2. Although the FFOV measurement is appealing for its larger field of view, an evaluation of resolution limitations on turbulence measurements based on only mean velocity profiles is insufficient.

3.1.2 Reynolds Stress Profiles

Contrary to the mean velocity profiles shown in the previous section, there is a discernible impact of the PIV spatial resolution on the resulting Reynolds stress profiles, shown for both the rough and smooth wall cases in Figure 5.

In general, the FFOV profiles are depressed compared to the MFOV profiles, but the level of impact varies between stress components and is more obvious in the smooth wall measurements. For instance, the coarser streamwise Reynolds stress profiles deviate from the finer resolution profiles with closer proximity to the wall, whereas the wall-normal stress profiles show a consistent attenuation of the stress magnitudes throughout the measured boundary layer profile. The comparatively larger impact of the resolution on the wall-normal component also results in an overall decrease (as opposed to a near-wall concentrated attenuation) in the represented shear stress magnitudes. The difference in attenuation magnitudes between the two stress components demonstrates an anistropy in the scales of energy-containing eddy structures, where the wall-normal fluctuating scales are much smaller than the streamwise turbulence scales. This comparison implies that in order to capture the full-extent of all directional flow contributions, an instrument spatial resolution requires an even tighter tolerance to accurately measure the wall-normal and shear stress contributions in a turbulent boundary layer. The increase in measured turbulence stress with a finer resolution is better illustrated in Figure 6 which shows the ratio of the FFOV to MFOV Reynolds stress profiles by component. The Reynolds stress ratios shown in this figure were produced by a linear interpolation of the measured data to a common grid in order to compare the relative change in stress magnitudes at an equivalent y^+. Due to the limited wall-normal field of view captured using the MFOV PIV configuration, only a portion of stress ratios along the boundary layer are calculable. For the smooth wall profiles in Figure 6a it shown that a finer spatial resolution increased the $\overline{u^2}$ stress magnitudes by only $1.05-1.12$ times the coarse resolution magnitude, whereas the $\overline{v^2}$ profile magnitudes were increased by upwards of $1.8-1.9$ times, and as a result, the shear stress magnitudes were also improved by a factor of $1.39-1.45$ with the finer resolution. Physically, this shows that the smaller-scale structures contributing to the wall-normal turbulence has a significant impact to the overall shear stress magnitudes.

The wall-normal position at which the $\overline{u^2}$ FFOV profiles deviates from the equivalent MFOV profile also depends on the pressure gradient condition. Although the attenuation of the Reynolds stresses due to resolution is observed in all the pressure gradient conditions, an increase in attenuation based on local Reynolds number is observed. For both the streamwise and wall-normal Reynolds stresses, the profiles in adverse pressure gradient (indicated by the red markers in the figures) show a much more significant gap between the MFOV and FFOV PIV measurements, which decreases as the flow approaches a more favorable pressure gradient (black and blue curves in the figures).

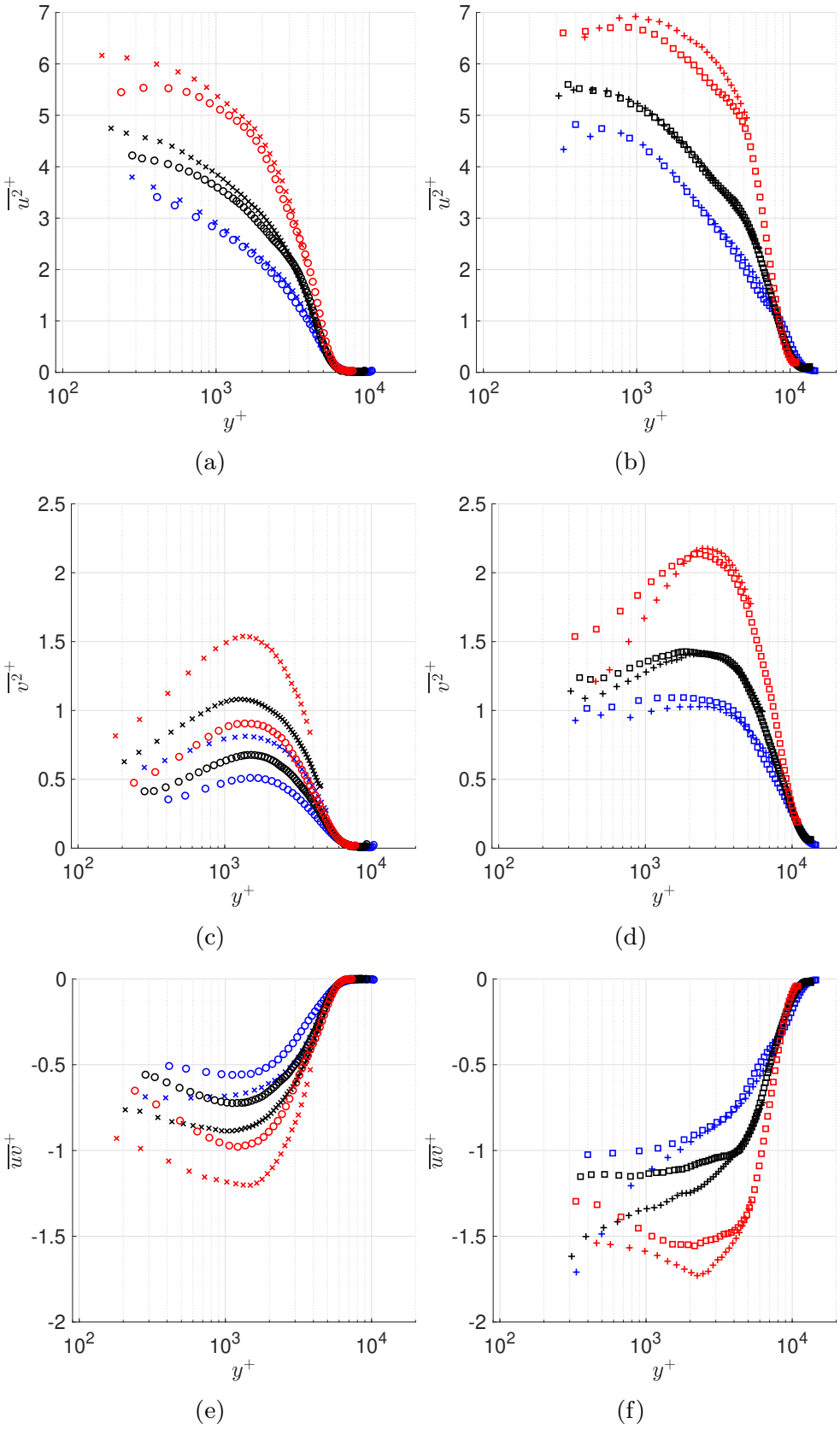

Fig. 5: Reynolds normal and shear stresses in wall coordinates over the smooth (left) and rough (right) wall measured using both MFOV and FFOV PIV configurations. Data symbols listed in Table 1.

A comparison of the stress ratio magnitudes shown in Figure 6a generally shows an increase to the measured turbulence magnitude for the adverse pressure gradient profile, especially at the turbulence peak at $y \approx 2000$, whereas the favorable and zero pressure gradient turbulence peaks, although improved, show a comparatively lower ratio magnitude. This difference in the ratio of stress magnitudes between pressure gradients shows that the limitations of a constant instrument spatial resolution for studies with varying ranges of turbulence scales can cause misleading comparisons of flows with a variation of local Reynolds number; the turbulence magnitudes could very well be much higher than shown, and the comparative increase between the zero, favorable and adverse pressure gradients could also be more significant. The considerations for Reynolds number effect are especially relevant for studies on functional dependencies of pressure gradients in both experimental and computational modeling.

The discussion in this section thus far has focused mostly on the smooth wall profiles, as the apparent effect of spatial resolution on the measured turbulence profiles over the rough wall appears to be less prominent for this station. Contrary to the stress ratios for the smooth wall, the profiles for the rough wall profiles shown in 6b do not show a clear component-wise improvement in stress magnitudes and are conglomerated around a ratio of 1, where the deviations in the near-wall are not consistent with stress-component. However, the stress ratios of a velocity field measured at $x = 3.94$ m, as shown in Figure 7b, indicates an increase in the measured turbulence magnitude with finer resolution. The inconsistency in the measured turbulence magnitudes for the rough wall, indicates a more complicated function of the β history and local Reynolds number on the rough wall resolution problem. There does appear to be a local Reynolds number effect in the turbulence magnitudes represented by the two PIV resolutions, where the APG MFOV profiles show a slightly higher magnitude especially near the turbulence peak at $y^+ \approx 2240$. As such, it is difficult to distinguish the exact improvement to the measured rough wall turbulence magnitudes with the finer resolution. This reduced improvement of a finer resolution on the measured rough wall stresses at $x = 2.74$ m is presumably due to an increase in magnitude of outer parameter scales under rough wall conditions which shifts the dominant energy-containing structures to even larger eddy sizes. Thus, the overall tolerance of resolution necessary to capture the relevant turbulence behaviors for the rough wall is less sensitive than that required for the smooth wall measurements.

3.2 Two-Point Correlation Coefficients

The previous section suggests an increased attenuation of measured stress magnitudes for the wall-normal component of the smooth wall conditions due to relatively smaller scales of the eddies present in the flow. This idea of length-scale variations can be explored further by analyzing the two-point correlation, which is a useful statistical tool to understand the spatial relation of a set

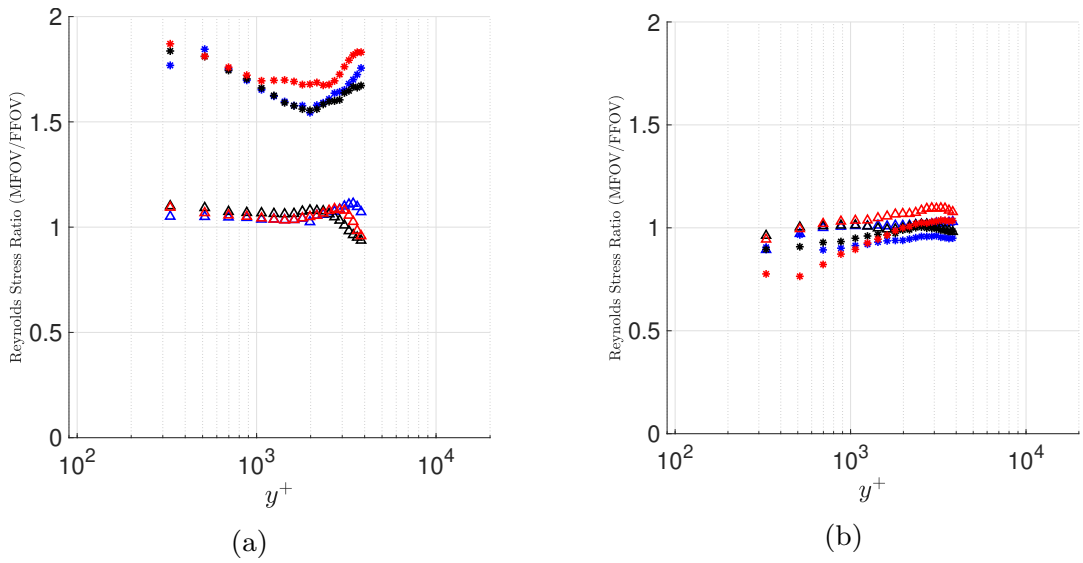

Fig. 6: Ratios of the Reynolds stress profiles for the MFOV PIV data normalized on equivalent FFOV data for the smooth (a) and rough (b) wall measurements at x = 2.74 m. Colors of symbols indicate the NACA 0012 airfoil at -10°, 0°, $+12^o$. Profiles for $\overline{u^2}$ ratio shown as $\triangle$, $\overline{v^2}$ ratio shown as $*$.

of variables at two points in a velocity field. The two-point correlation coefficient with streamwise separation (Δx) as a function of wall-normal position is computed as:

$$\rho_{ij}(\Delta x, y) = \frac{\overline{u_i'(x,y)u_j'(x+\Delta x, y)}}{\sigma_i(y)\sigma_j(y)} \tag{1}$$

where u_i is the fluctuating velocity component of interest and σ_i is the component standard deviation. In equation 1, the flowfield statistics are assumed homogenous in the x-direction. Figures 8 and 9 show the one-dimensional, two-point correlation coefficients of the streamwise and wall-normal velocity components correlated in the streamwise direction at a y^+ = 500 and at y^+3500 for both the smooth and rough wall flows computed from data measured with the MFOV and FFOV PIV configurations.

As observed in the Reynolds stress profiles, the rough wall correlations in Figure 9 are less sensitive to the spatial resolution as evidenced by an overlap of the correlations in both the fine and coarse resolution measurements at both wall-normal positions. In contrast, there is a clear distinction between the MFOV and FFOV profiles for the smooth wall correlations, especially at the point closer to the wall at y^+ = 500. The correlation length for an equivalent correlation magnitude appears to be shorter for the magnified PIV condition, a behavior that is consistent for all pressure gradient magnitudes. The correlation lengths are also, in general, much shorter for the wall-normal component, where the flow appears to rapidly decrease to near zero-correlation by the point at which separations exceed $+/-\Delta x/\delta \approx 0.3$. The discrepancy

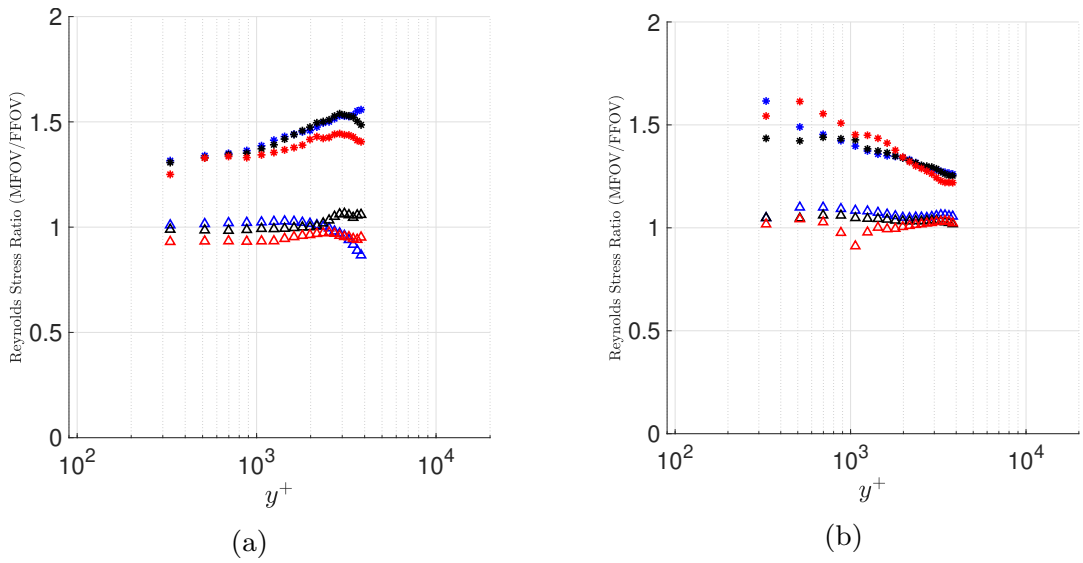

Fig. 7: Ratios of the Reynolds stress profiles for the MFOV PIV data normalized on equivalent FFOV data for the smooth (a) and rough (b) wall measurements at $x = 3.94$ m. Symbols and colors same as for Figure 6.

between the MFOV and FFOV profiles is reduced with increasing wall-normal distance, but is still present for the wall-normal correlation at $y^+ = 3500$ as seen in Figure 8b. This again shows that the wall-normal correlations are dependent on smaller structures and are correlated for shorter streamwise lengths.

This behavior is better quantified in Figures 10 and 11 which show integral length-scales normalized on boundary layer thickness, which are computed from the correlation coefficient profiles integrated to a fixed correlation of $\rho_{ij} = 0.5$ for both wall conditions. First, comparing the component length-scales for the smooth wall in Figure 10, we see that even the minimum streamwise length-scale observed with the MFOV PIV is still larger by at least one tenth of the normalized wall-normal length-scale measured with the FFOV PIV. Additionally, a rapid decrease in the computed length-scale is observed in both directional components and both wall conditions approaching the wall, but the decline starts at a position further away from the wall for the wall-normal component at $y/\delta = 0.2$. Even at a magnified resolution, the observed streamwise length-scales are larger than those measured with a coarse resolution for the wall-normal component which further impresses the limitation of the instrument resolution in accurately capturing turbulent boundary layer behaviors due to the inherent flow anisotropy.

3.3 Distribution of Energy Density in Wavenumber Spectra

The comparisons of the turbulence stresses and correlation coefficients in the previous sections have demonstrated the limitation of instrument spatial resolution in accurately measuring the turbulence statistics at eddy scales smaller

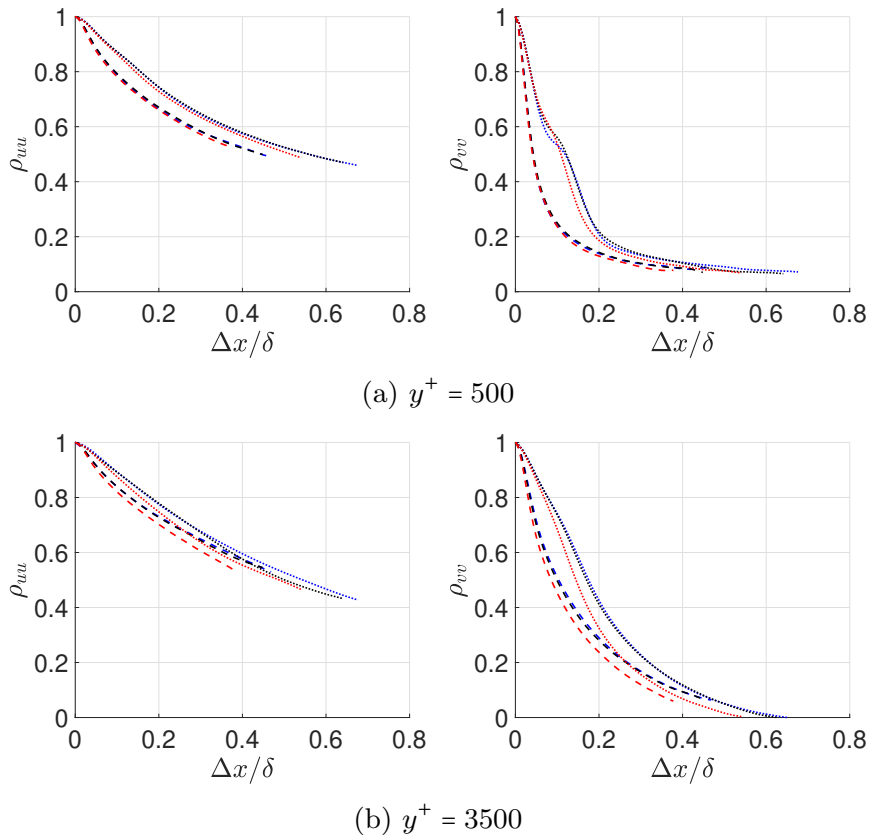

(a) $y^+ = 500$

(b) $y^+ = 3500$

Fig. 8: Streamwise (left) and wall-normal (right) component, single-sided, two-point correlation coefficients for the smooth wall at a $y^+ = 500$ (a) and $y^+ = 3500$ (b) measured using both the MFOV (- - - - -) and FFOV (.....) PIV configurations. Line color indicates the NACA 0012 airfoil angle of attack at -10°, 0°, $+12^o$.

than the resolution, an issue that particularly affects the wall-normal measurements made over smooth surfaces. Thus, an investigation of the wavenumber velocity spectra can be used to relate the measurement spatial resolution to the range of wavenumbers measured in the turbulent boundary layer. The premultiplied spectral maps for the streamwise and wall-normal velocity components are shown as logarithmic contours for the smooth and rough wall conditions in Figures 12 and 13, respectively. As discussions in previous sections have already established the limitations of a coarse resolution on measuring local Reynolds number differences due to pressure gradient, spectral contours for only flow conditions generated with the airfoil at $+12^o$ are shown. The wavenumber spectra were computed from the fluctuating velocity components from $24,839$ realizations with a rectangular window weighting and are presented in terms of the streamwise wavenumber k_x. The magnified PIV results are plotted on the left columns and the full field of view results are plotted on the right columns of the provided figures.

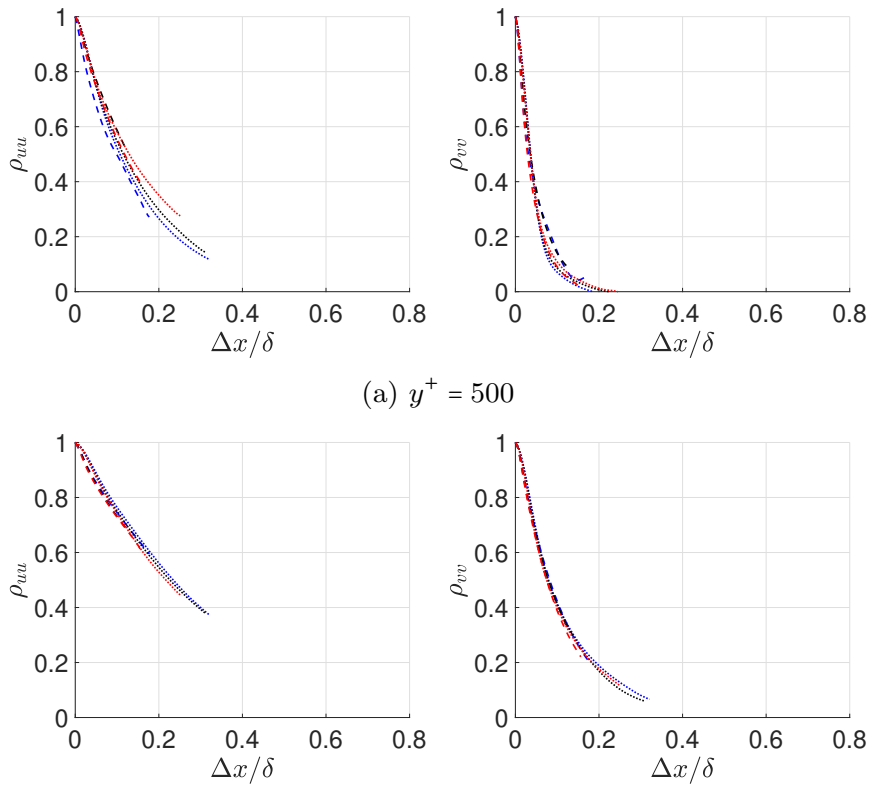

(a) $y^+ = 500$

(b) $y^+ = 3500$

Fig. 9: Streamwise (left) and wall-normal (right) component, single-sided, two-point correlation coefficients for the rough wall at a $y^+ = 500$ (a) and $y^+ = 3500$ (b). Color and line legend same as in Figure 8.

The compromise between field of view and spatial resolution of each measurement configuration is further illustrated in these contour plots. Due to the larger image field of view, the FFOV data is able to measure the energy distributions at higher wall-normal distances as compared to a partial view captured with the MFOV PIV. However, the magnified PIV is able to measure spectral densities at higher wavenumbers and shows a higher magnitude of energy density at an equivalent measured wavenumber for the smooth wall, consistent with the earlier findings. Instead, the FFOV data succumbs to the effects of aliasing at a larger wavenumber as seen in the hitch occurring at about $k_x^+ \approx 10^{-2}$ in the spectra. Visually, the increase in energy density magnitude in the MFOV measurements appears as a vertical shift in the represented energy for the smooth wall spectral densities. This shift is particularly obvious for the $\overline{v^2}$ spectra (Figure 12b) where the color bands show higher energy contributions for higher wavenumbers (implying smaller-scale structures) as compared to the streamwise spectra (Figure 12a). For instance, the band of spectral density magnitudes occurring between a $4 \times 10^{-3} < k_x^+ < 6 \times 10^{-3}$ for the FFOV data shown in Figure 12b is shifted to a higher wavenumber range between $1.5 \times 10^{-2} < k_x^+ < 2.5 \times 10^{-2}$. The streamwise wavenumber spectra are

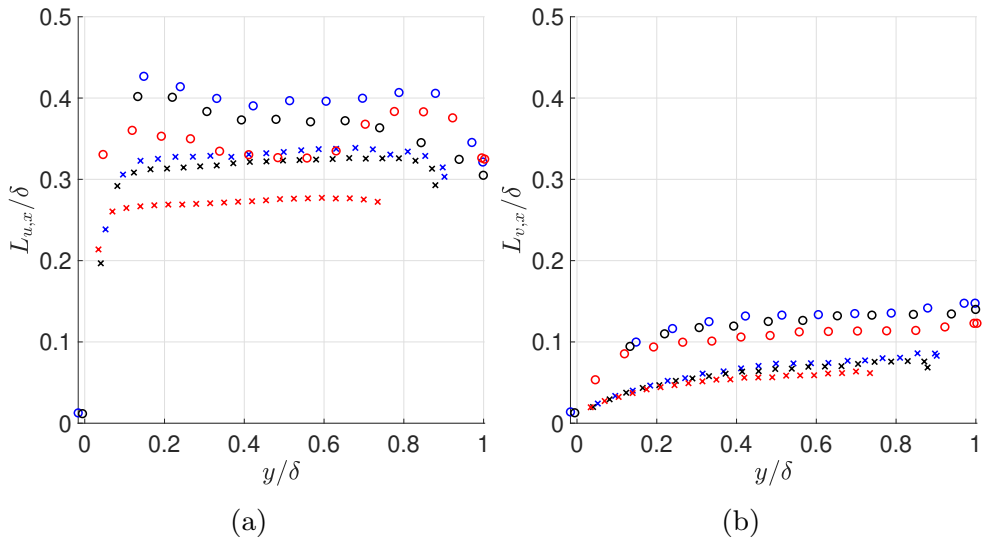

Fig. 10: Streamwise (left) and wall-normal (right) length-scales as a function of wall-normal position for the smooth wall. Data symbols listed in Table 1.

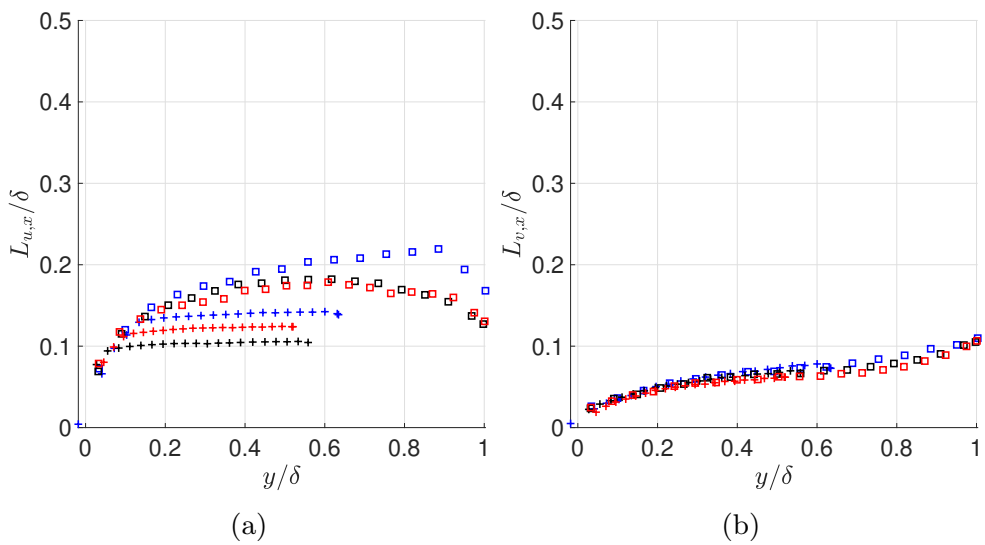

Fig. 11: Streamwise (left) and wall-normal (right) length-scales as a function of wall-normal position for the rough wall. Data symbols listed in Table 1.

less affected. The same color-bands in the streamwise spectra are represented by near identical wavenumber ranges for both spatial resolution measurements. The component-level difference in the response to an improved spatial resolution again emphasizes the necessity for a tighter measurement resolution to accurately reflect the anisotropy of large-scale turbulent eddies occurring in the boundary layer.

Concurrent with the behaviors seen in the Reynolds stresses and correlation coefficients, there is no discernible impact of the spatial resolution on the

represented energy for the rough wall conditions in both velocity component directions (see Figure 13, where the spectral contours show qualitative behaviors similar to that observed in the streamwise spectra for the smooth wall, where the energy magnitudes at each contour band are represented by near equivalent wavenumber ranges for both magnifications and component directions. Thus, the rough wall turbulence measurements are less susceptible to resolution limitations than those measured over a smooth wall for measurements made a this station. The variation in response to the spatial resolution between wall conditions must be considered when evaluating the wall-similarity hypothesis, which is the idea that, outside of the immediate roughness vicinity, the rough wall boundary layer behaves much like an equivalent smooth wall flow. The Reynolds stress profiles between wall conditions are not directly compared as part of the current investigation as the commonly accepted criteria for wall-similarity is not met (i.e. $\delta/k_s < 40$). However, the authors caution the reader to consider the bias uncertainty due to an under sampling of the spatial resolution which can cause a higher attenuation of the smooth wall Reynolds stresses well, into the logarithmic region and, when compared to a rough wall flow, could falsely imply a larger effect of the roughness sublayer on the outer turbulence characteristics.

4 Conclusion

Access to a larger measurement field of view with simultaneous multi-point measurement techniques such as particle image velocimetry (PIV) is often not without a compromise in spatial resolution. A lack of sufficient resolution attenuates the represented turbulence magnitudes due to the inability to accurately capture the behaviors of eddy features smaller than the instrument resolution. This study investigated the impact of hardware level PIV spatial resolution limitations on measurements made of turbulent boundary layers by comparing mean and fluctuating turbulence statistics computed from velocity fields measured with baseline (coarse resolution) and doubly magnified (finer resolution) camera lenses. Measurements were conducted on boundary layers developing over rough and smooth walls in pressure gradient to also evaluate the effect of wall and local Reynolds number effects on the resolved turbulence statistics using a fixed instrument resolution across all conditions. The mean velocity profiles across all flow conditions show an indifference to the spatial resolution. However, Reynolds stress profiles, for the wall-normal component of the smooth wall in particular, show a higher attenuation of turbulence magnitudes throughout the boundary layer. An evaluation of the correlation coefficients shows that the comparatively larger impact to wall-normal stress attenuation is due to the shorter correlation lengths of the wall-normal eddy structures, thus requiring a finer resolution to capture the behaviors at the relevant smaller scales. Additionally, due to the larger of separation of scales in a flow with higher local Reynolds number, PIV measurements made with a

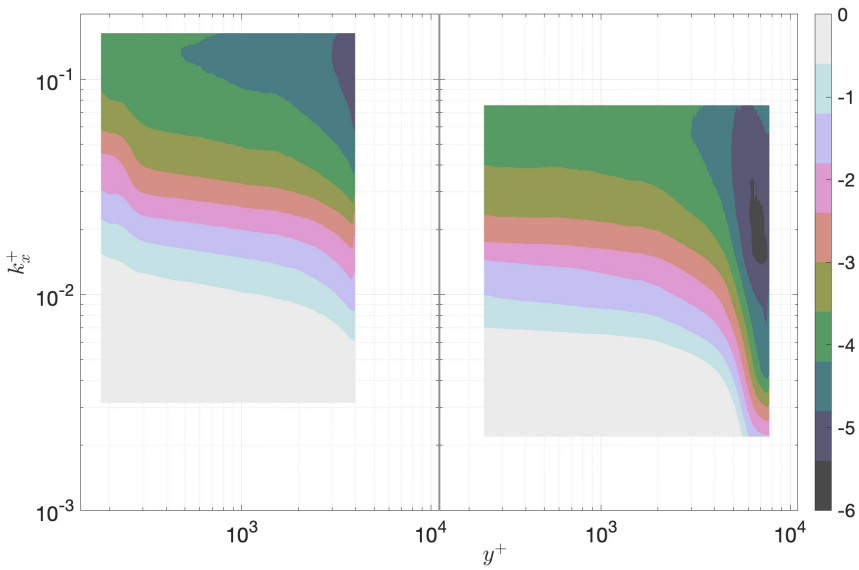

(a)

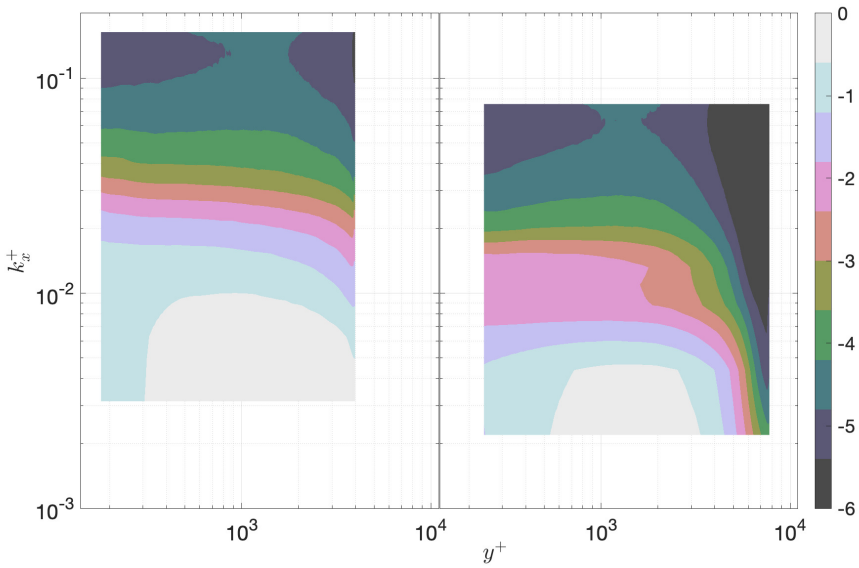

(b)

Fig. 12: Smooth wall wavenumber spectra at $\alpha = 12^o$ for the magnified (left) and full (right) fields of view; (a) streamwise, $log(k_x\phi_{uu}/u_\tau^2)$ and (b) wall-normal $log(k_x\phi_{vv}/u_\tau^2)$.

fixed spatial resolution of a common streamwise station under different pressure gradient conditions resulted in unequal measurements of the boundary layer both in terms of wall-normal field of view and stress magnitudes. This compromise for finer resolution and a truncated wall-normal field of view is best illustrated in the wavenumber spectra which show a larger magnitude of

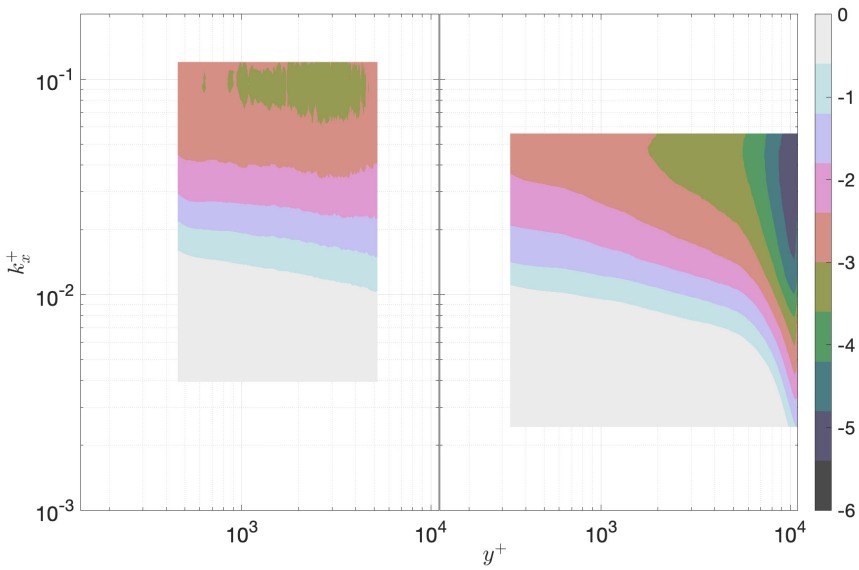

(a)

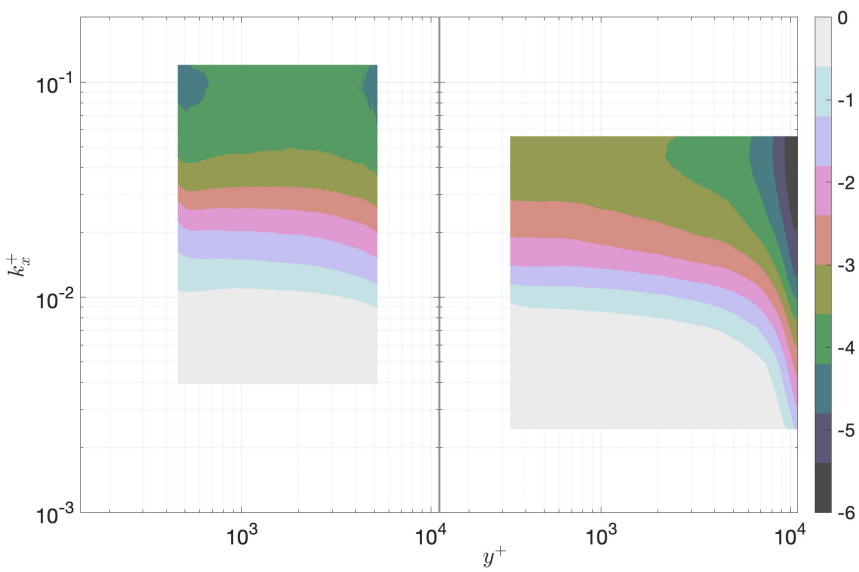

(b)

Fig. 13: Rough wall wavenumber spectra at α = 12° for the magnified (left) and full (right) fields of view; (a) streamwise, $log(k_x\phi_{uu}/u_\tau^2)$ and (b) wall-normal $log(k_x\phi_{vv}/u_\tau^2)$.

energy for equivalent wavenumbers with a magnified resolution, but only for a focused region within the boundary layer. Due to the enlarged eddy structure length-scales of rough wall flows, the resolution impacts are less severe when compared to equivalent measurements made over smooth walls, however, flow history and local Reynolds number changes to the rough wall boundary

layer indicate an improvement to the turbulence magnitudes. Although it is impractical to capture all relevant scales of turbulence due to the stringent resolution requirements necessary, this study has shown that the prevalence of anisotropy in a turbulent boundary layer suggests the need for multi-resolution measurements to study statistical convergence across all velocity components, regardless of wall condition. An evaluation of instrument resolution based only mean streamwise velocity parameters is insufficient in high Reynolds number turbulence studies. Suggestions to correct under-resolved data are beyond the scope of the current paper, but inspiration from CFD grid convergence studies based on the principles of grid extrapolation is a potential method for a posteriori corrections of experimental measurements.

Acknowledgments

The authors would like to thank the Office of Naval Research, Dr. Peter Chang, and Dr. Julie Young for support under grants N00014-19-1-2109, N00014-18-1-2455, and N0014-20-1-2821. The authors are also grateful to the VT Stability Wind Tunnel research staff and faculty, AOE Machine Shop, and fellow research students Jarrod Banks, Surabhi Srivastava, Humza Butt, Mason Fitzsimmons, and Sasha Mintz for their support and assistance in the experimental preparation and testing.

Supplementary information

Funding. This work was sponsored by Office of Naval Research. The authors are grateful to Dr. Peter Chang, and Dr. Julie Young for support under grants N00014-19-1-2109, N00014-18-1-2455, and N0014-20-1-2821.

Ethics Approval. Not applicable

Conflict of interest/Competing interests. Not applicable

Consent for Publication. Not applicable

References

[1] Johansson, A.V., Alfredsson, P.H.: Effects of imperfect spatial resolution on measurements of wall-bounded turbulentbx shear flows. Journal of Fluid Mechanics **137**, 409–421 (1983). https://doi.org/10.1017/S0022112083002487

[2] Saltzman, A.J., Lowe, K.T., Ng, W.F.: Finite control volume and scalability effects in velocimetry for application to aeroacoustics. Experiments in Fluids **62**(2), 33 (2021). https://doi.org/10.1007/s00348-021-03138-2

[3] Lavoie, P., Avallone, G., De Gregorio, F., Romano, G.P., Antonia, R.A.: Spatial resolution of piv for the measurement of turbulence.

Experiments in Fluids **43**(1), 39–51 (2007). https://doi.org/10.1007/s00348-007-0319-x

[4] Saddoughi, S.G., Veeravalli, S.V.: Local isotropy in turbulent boundary layers at high reynolds number. Journal of Fluid Mechanics **268**, 333–372 (1994). https://doi.org/10.1017/S0022112094001370

[5] Saarenrinne, P., Piirto, M., Eloranta, H.: Experiences of turbulence measurement with piv. Measurement Science and Technology **12**(11), 1904 (2001)

[6] Gamba, M., Clemens, N.: Requirements, Capabilities and Accuracy of Time-Resolved PIV in Turbulent Reacting Flows. https://doi.org/10.2514/6.2011-362

[7] Smits, A., Monty, J., Hultmark, M., Bailey, S.C.C., Hutchins, N., Marusic, I.: Spatial resolution correction for wall-bounded turbulence measurements. Journal of Fluid Mechanics **676**, 41–53 (2011)

[8] Chin, C.C., Hutchins, N., Ooi, A.S.H., Marusic, I.: Use of direct numerical simulation (dns) data to investigate spatial resolution issues in measurements of wall-bounded turbulence. Measurement Science and Technology **20**(11), 115401 (2009). https://doi.org/10.1088/0957-0233/20/11/115401

[9] Lee, J., Monty, J., Hutchins, N.: Validating under-resolved turbulence intensities for piv experiments in canonical wall-bounded turbulence. Experiments in Fluids **57**(8), 1–11 (2016)

[10] Rahgozar, S., Maciel, Y., Schlatter, P.: Spatial resolution analysis of planar piv measurements to characterise vortices in turbulent flows. Journal of Turbulence **14**(10), 37–66 (2013)

[11] Gatti, D., Stroh, A., Frohnapfel, B., Örlü, R.: Spatial resolution issues in rough wall turbulence. Experiments in Fluids **63**(3), 63 (2022). https://doi.org/10.1007/s00348-022-03412-x

[12] Duetsch-Patel, J.E., Vishwanathan, V., Minionis, J.B., Totten, E., Gargiulo, A., Fritsch, D.J., Szoke, M., Borgoltz, A., Roy, C.J., Lowe, K.T., Devenport, W.J.: Aerodynamic Design and Assessment of Modular Test Section Walls for CFD Validation in Hybrid Anechoic Wind Tunnels, (2020). https://doi.org/10.2514/6.2020-2214

[13] Remillieux, M., Crede, E., Camargo, H., Burdisso, R., Devenport, W., Rasnick, M., Van Seeters, P., Chou, A.: Calibration and Demonstration of the New Virginia Tech Anechoic Wind Tunnel, (2008). https://doi.org/10.2514/6.2008-2911

[14] Vishwanathan, V., Szoke, M., Duetsch-Patel, J.E., Gargiulo, A., Fritsch, D.J., Borgoltz, A., Roy, C.J., Lowe, K.T., Devenport, W.J.: Aerodynamic Design and Validation of a Contraction Profile for Flow Field Improvement and Uncertainty Quantification in a Subsonic Wind Tunnel, (2020). https://doi.org/10.2514/6.2020-2211

[15] Fritsch, D.J., Vishwanathan, V., Lowe, K.T., Devenport, W.J.: Fluctuating pressure beneath smooth wall boundary layers in nonequilibrium pressure gradients. AIAA Journal **0**(0), 1–19 (2022). https://doi.org/10.2514/1.J061431

[16] Vishwanathan, V., Fritsch, D., Lowe, T.K., Devenport, W.J.: Analysis of Coherent Structures over a Smooth Wall Turbulent Boundary Layer in Pressure Gradient Using Spectral Proper Orthogonal Decomposition, (2021). https://doi.org/10.2514/6.2021-2893

[17] Clauser, F.H.: The turbulent boundary layer **4**, 1–51 (1956). https://doi.org/10.1016/S0065-2156(08)70370-3

[18] Perry, A.E., Joubert, P.N.: Rough-wall boundary layers in adverse pressure gradients. Journal of Fluid Mechanics **17**(2), 193–211 (1963). https://doi.org/10.1017/S0022112063001245

[19] Vishwanathan, V., Fritsch, D.J., Lowe, K.T., Devenport, W.J.: History effects and wall similarity of non-equilibrium turbulent boundary layers in varying pressure gradient over rough and smooth surfaces. In: 12th International Symposium on Turbulence and Shear Flow Phenomena (TSFP12), Osaka, Japan (19-22 July, 2022)

Chapter 4

History Effects and Wall Similarity of Non-Equilibrium Turbulent Boundary Layers in Varying Pressure Gradient Over Rough and Smooth Surfaces

The contents of this chapter contain a manuscript in the Elsevier journal submission format to be submitted and in-review for publication to the *International Journal of Heat and Fluid Flow*. This work was invited to publication to the journal after being presented at the 12th International Symposium on Turbulence and Shear Flow Phenomena (TSFP12). This paper presents an evaluation of the parameters necessary to determine the validity of the wall-similarity hypothesis for rough wall turbulent boundary layers in non-equilibrium pressure gradient.

History Effects and Wall-Similarity of Non-Equilibrium Turbulent Boundary Layers in Varying Pressure Gradient Over Rough and Smooth Surfaces

Vidya Vishwanathan[a], Daniel J. Fritsch[a], K. Todd Lowe[a], William J. Devenport[a]

[a]*Virginia Tech, 225 Stanger St., Blacksburg, 24060, VA, USA*

Abstract

The effect of non-equilibrium pressure gradients and roughness on the behavior of turbulent boundary layers over rough and smooth surfaces was experimentally investigated. A NACA 0012 airfoil was systematically rotated to generate a family of bi-directional pressure fields on the research wall. The rough surface consisted of 2 mm tall, staggered, circular cylindrical elements producing flow conditions that were in the fully rough regime. The velocity fields were measured using a custom Pitot-probe boundary layer rake and time-resolved particle image velocimetry (TR-PIV). The results show that the primary effect of the roughness is to increase the magnitude of the outer layer parameters, but retain the same qualitative response to the variations in pressure gradient histories as the smooth wall conditions. One such common flow behavior is the presence of history effects, apparent in the integrated boundary layer parameters, which indicates that rough and smooth wall flows are affected by both local and historical flow conditions. It is shown that indirect skin friction methods in rough wall analysis are sensitive to regression fits of the mean velocity profiles. Within the uncertainty of these empirical methods, the effective sandgrain roughness parameter, k_s, appears to remain independent of pressure gradient flow history. Varying levels of wall-similarity in the Reynolds stress profiles on inner-outer coordinates is observed. A comparative inspection of multiple flow parameters, such as pressure gradient flow history, boundary layer thickness to roughness parameter ratios, friction Reynolds number, and measurement resolution indicates that an evaluation of the wall-similarity condition requires consideration of multiple parameters.

Keywords: Rough wall turbulent boundary layers, non-equilibrium pressure gradients, wall-similarity hypothesis

1. Introduction

Turbulent boundary layers are omnipresent in a wide range of practical applications, such as over an aircraft wing or marine vehicle body. These surfaces in common engineering application are also not considered to be hydrodynamically smooth, either due to macroscopic defects in the surface finish or due to naturally occurring roughness, such as dirt, ice or biofouling. Roughness can contribute to drag, unwanted vibrations, and noise, which can negatively impact the operation and design of vehicles. A wide range of studies have established a fundamental understanding of rough wall turbulent boundary layers in uni-directional pressure gradient flows, most of whom have found that the flow behavior in the outer region is most susceptible to changes in

pressure gradient magnitude and direction (e.g., Finnicum and Hanratty (1988); Cal et al. (2009); Krogstad et al. (1992); Perry and Joubert (1963)). Aside from use in controlled laboratory environments, these simple flows are just the building blocks for flows of practical interest. Real flows are susceptible to complex conditions impacted by both roughness and bi-directional pressure gradients (i.e., pressure gradients that switch sign). However, these flows are more difficult to model; thus improving the current array of knowledge for flows in non-equilibrium conditions is a relevant field of interest.

To understand the concept and behaviors of flows in non-equilibrium, it is useful to first establish what is considered to be a flow *in* equilibrium. Equilibrium conditions are idealized states in which flow properties are only dependent on local flow conditions, and the evolution of mean velocity and turbulence quantities with streamwise position can be collapsed by scaling on the basis of self-similarity (Devenport and Lowe (2022)). Although a boundary layer flow in true equilibrium is rare in application, it considered to be a flow that shows constancy of some form of pressure gradient parameter, usually a function of a characteristic length scale, streamwise pressure gradient, and wall shear stress. In this study, the variation of the Clauser pressure gradient parameter, β, is used to determine the behaviors of pressure gradient history, where a positive value indicates a flow in an adverse pressure gradient (APG), a negative value indicates a flow in favorable pressure gradient (FPG), and a zero-value (or for the purpose of a practical experiment, near-zero) indicates a zero-pressure gradient (ZPG) flow.

Compared to a canonical ZPG flow, the effect of a uni-directional APG is to thicken the boundary layer, thus increase both the energy of the outer region and the local characteristic Reynolds number. In contrast, the effect of the FPG is to decrease the size of the boundary layer and the corresponding length scales, and an increase of velocity gradient results in a proportional increase in the wall shear stress. In a non-equilibrium turbulent flow, the local flow conditions are now also dependent on the history of conditions that the flow has experienced. In studies of smooth wall turbulent boundary layers induced by bi-directional pressure gradients, Fritsch et al. (2022) and Vishwanathan et al. (2021) found impacts of history effects on the behavior of the fluctuating pressure and velocity fields. Notably, these history effects were evidenced by a streamwise delayed response of the integrated boundary layer parameters and mean turbulence statistics with respect to the location of the pressure gradient switch. The importance of considering flow history is detailed in a study by Bobke et al. (2017), whose simulation work showed that regardless of a common local pressure gradient parameter, the flow behaviors were dependent on its origin and history.

The main objective of this investigation is to understand if the same response to non-equilibrium pressure gradient conditions are exhibited in rough wall flows. A key standard of comparison is the validity of the wall-similarity hypothesis, a concept first introduced by Townsend (1980), which suggests that, on certain velocity parameter scalings the boundary layer regions outside of the immediate roughness vicinity collapse with an equivalent smooth wall flow. Jiménez (2004) refined the criteria for wall-similarity to specify roughness height (k_g) limitations with respect to either the effective sandgrain roughness (k_s) or the boundary layer thickness (δ). Although the exact regimes of validity of this hypothesis continues to be refined, a number of studies (i.e., Raupach et al. (1991); Flack et al. (2005); Perry and Joubert (1963); Schultz and Flack (2005)) have developed a minimum criteria for boundary layer thickness to k_s or k_g ratios in order for wall-similarity to be considered (the exact factor varies between authors, but is typically taken as $\delta/k_s \geq 40$). But enough studies, such as those by Castillo and Wang (2004); Aubertine et al. (2004); Mehdi et al., suggest that the current criteria for wall similarity is insufficient, and additional parameters relating the local flow to the pressure gradient history

are necessary to account for behaviors in non-equilibrium pressure gradient fields. Additionally, studies by Krogstad et al. (1992); Acharya and Escudier (1987) demonstrated anisotropy in the rough wall Reynolds stress profiles due to directional variations in the outer-layer extent of roughness effects. As a majority of the earlier referenced studies have been conducted in equilibrium flow conditions, an evaluation of multiple parameters, aside from just the δ/k_s parameter, is necessary to determine the extent of roughness influences in the boundary layer.

The present work aims to understand the behavior of high Reynolds number wall-bounded turbulence induced under a systematically varying family of pressure gradients and discuss its compounding effects with roughness. In particular, investigations of the wall-similarity hypothesis of non-equilibrium rough wall flows are made by comparing behaviors across in streamwise developing flows with matching upstream flow histories. Traditional analytical methods to determine roughness parameters are scrutinized to understand the impact of methodologies on resulting interpretations of the flow behavior. This experimental work largely uses the results from mean and instantaneous velocity fields measured using time-resolved particle image velocimetry (TR-PIV) and a custom boundary layer rake.

2. Experimental Facility

All measurements discussed in this paper were conducted in the Virginia Tech Stability Wind Tunnel (VT SWT), which is a closed-circuit facility. The empty tunnel freestream turbulence levels vary between 0.01% and 0.023% depending on the flow speed, owing to seven turbulence reducing screens in the settling chamber. The test section extends 7.32 m and has a square cross section 1.85 m on edge. The test section side walls consist of 0.61 m length modular square aluminum panels that are carefully levelled to produce a continuous boundary layer flow surface. These panels were arranged in a grid pattern that were removed and replaced with panels with custom instrumentation and wall conditions. The coordinate origin is located at the start of the roughness substrate and the boundary layer was tripped 3.58 m upstream of origin. By the first measurement plane, at x = 1.25 m, the boundary layer developed to 52 mm thick in smooth wall and 62 mm thick in rough wall configurations. The data discussed in this paper were measured at a Reynolds number per meter of 2.18 million based on the inflow freestream velocity, which at the time of the rough and smooth wall experimental studies was between $U_\infty = 33 - 36$ m/s.

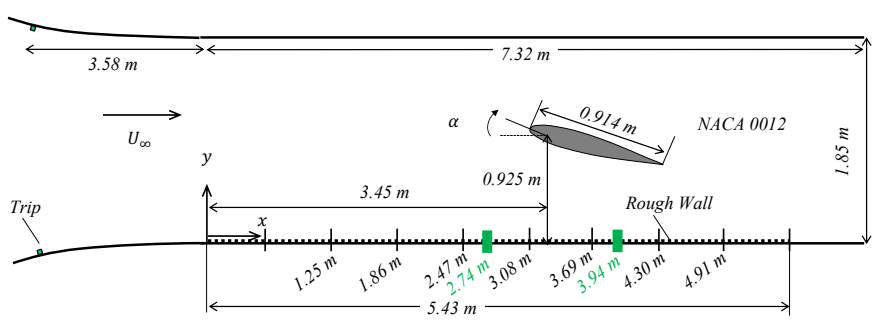

Figure 1: Top-down schematic of the test section. Boundary layer wall of interest is the "port" wall, seen here as the lower wall, which was either in smooth or rough wall configuration. Measurement locations of the boundary layer rake and TR-PIV are indicated in vertical black and green lines, respectively.

3. Roughness Geometry

A portion of the rough surface used in this study is shown in Figure 2. The surface entails a staggered pattern array of circular cylindrical elements that have a roughness height of $k_g = 2$ mm and diameter of 3.14 mm and are periodic on a 0.61 m x 0.61 m pattern (corresponding to the size of the removable test section panels). As shown in the test schematic in Figure 1, the rough wall starts at the test section origin and extends 5.43 m downstream covering the entire port side test section wall. The elements are spaced $s = 6.93$ mm apart in the streamwise direction, and half this distance in the spanwise direction. The roughness elements were fabricated from epoxy using high-density polyethylene (HDPE) molds that were CNC milled with insets in the element shape. The mold was then overlaid on an aluminum test section panel and vacuum bag sealed for 24 hours of cure time. For ease of fabrication, the cylindrical element tips were tapered by 1°. Given current skin friction estimates computed from regression fits of the rough wall law of the wall, the roughness Reynolds number ranges between $k_s^+ = 243 - 488$. Thus, this flow is in the fully rough regime.

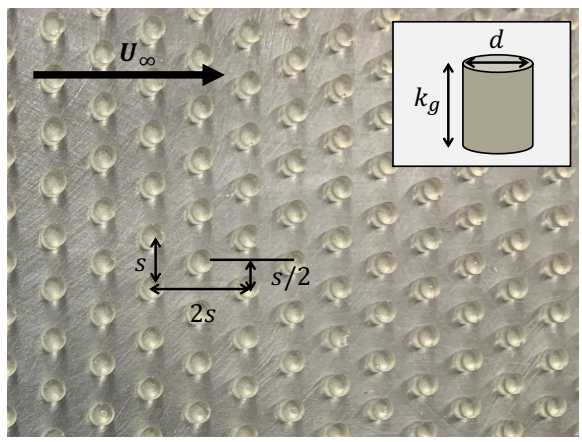

Figure 2: Staggered, circular cylindrical roughness configuration used in this study; $s = 6.93$ mm, $d = 3.14$ mm, $k_g = 2$ mm. Inset shows features of a cylindrical element.

4. Mechanism for Wall Pressure Gradient

A 0.914 m chord NACA 0012 airfoil, swept to both positive and negative angles of attack, generated a systematically varying family of closely two-dimensional pressure gradients on the test section walls. The airfoil quarter chord was positioned at $x = 3.45$ m and $y = 0.925$ m with respect to the coordinate origin. Figure 1 shows a top-down schematic, of the test section configuration. Because of the nominally symmetric airfoil and test section, both of the side walls experience the same flow families. However, for ease of measurement access, the boundary layer wall of interest considered in this study was the "port" side wall corresponding to the lower wall in Figure 1. The boundary layer wall experiences both an adverse and favorable pressure gradient, for which the initial condition depends on the airfoil angle of attack.

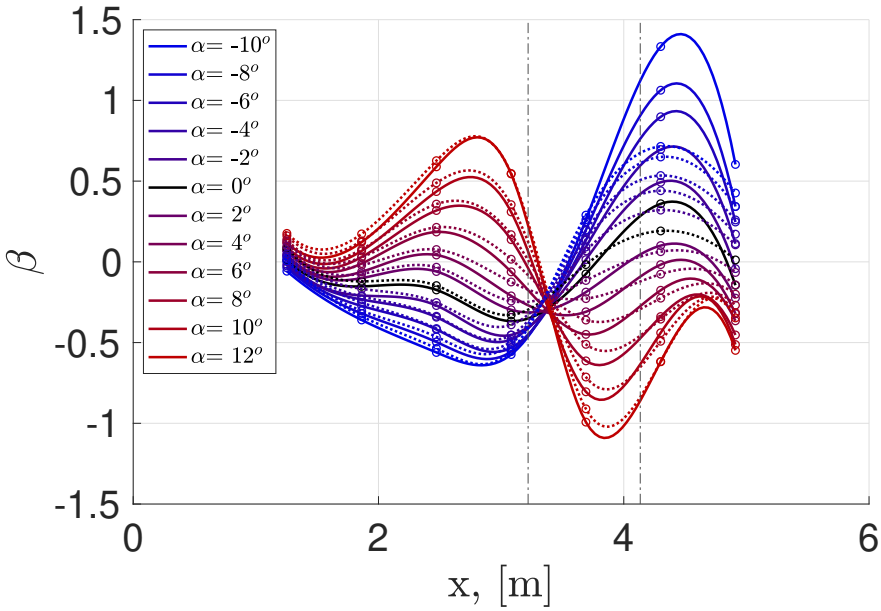

Figure 3: Streamwise variation of the Clauser pressure gradient parameter, β, as a function of the NACA 0012 angle of attack shown at the boundary layer rake measurement locations. Solid lines are the rough wall, dashed lines are the smooth wall. Vertical dashed lines indicate locations of the airfoil leading and trailing edge, respectively. Vertical solid lines indicate the locations of the TR-PIV measurements. Color legend is used for subsequent figures unless otherwise noted.

Figure 3 shows the distribution of β, on the instrumented portion of the center streamline on the boundary layer wall of interest. The magnitude of the pressure gradient was computed using the Clauser pressure gradient parameter defined as $\beta = (\partial p/\partial x)\delta^*/\tau_w$, where δ^* is the displacement thickness. In this experiment the pressure gradients were mild (i.e. no relaminarization nor separation), and ranged between $-0.91 < \beta < +0.71$ for the smooth wall, and between $-1.06 < \beta < +1.29$ for the rough wall, where the minimum and maximum pressure gradient magnitudes are reached after the pressure gradient sign change. A comparison of the rough and smooth wall pressure gradient distributions is shown in solid and dashed lines, respectively, where both walls experience similar histories upstream of the pressure gradient switch, occuring at approximately the streamwise station adjacent to the airfoil quarter chord. Downstream of this station, the pressure gradients switch sign and the rough and smooth wall flows start to show markedly different behavior, with significantly greater positive β excursions for the rough wall. At positive angles of attack the boundary layer wall experiences an APG which switches to a FPG at a streamwise location approximately adjacent to the airfoil quarter-chord. The opposite phenomena are experienced by the wall when the airfoil is at negative angles of attack. However, the switch to an adverse pressure gradient significantly deters this pressure gradient development in the rough wall, while the switch to the favorable pressure gradient, although different, does not result in as drastic of a change.

5. Measurement Systems

The two sidewalls of the test section were equipped with 82 static pressure taps each. The taps were carefully flush mounted to the inner wall/roughness substrate and had a 0.1 mm inner diameter. The mean surface pressure distributions were measured using an Esterline 9816/98RK pressure scanner with a range of ± 10" H_2O and a 32-channel DTC Initium scanner with a range of ± 4" H_2O. The reference pressure was measured as the ambient pressure in the control room.

A custom 30-Pitot probe boundary layer rake was used to measure the mean velocity profiles at the streamwise locations indicated by the black stations labeled on Figure 1. The probes extend 178 mm from the wall, a sufficient length for capturing the full rough and smooth wall boundary layer thicknesses. The probe ports were connected to a 20" H_2O pressure range DTC ESP 32HD pressure scanner. The velocity profile was inferred from Bernoulli's equation using the rake stagnation pressures and the test wall surface static pressures. All mean velocity profiles and integrated boundary layer parameters discussed in this paper were measured using the boundary layer rake.

Time-resolved PIV measurements were made at two streamwise planes corresponding to the upstream and downstream locations of maximum pressure gradient, measured at approximately $x = 2.74$ m and $x = 3.94$ m. The TR-PIV measurement locations are labeled in green in Figure 1 and indicated by the vertical green lines in Figure 3. Both the rough and smooth wall measurements were made in a stereoscopic 2D three-component configuration, in which 24,839 time realizations were recorded at a 1 kHz sampling rate. A 300 mm Nikon lens was used for full-profile measurements of the boundary layer, which was supplemented with a $2x$ Vivitar teleconverter lens for measurements made approximately $y/\delta < 0.5$ to improve measurements of finer scale features occurring near the wall. The two wall-normal measurement fields were then concatenated to create a cohesive profile for the turbulence stresses shown. The magnified PIV resolution varied between 1.06 – 1.09 mm while the baseline lens resolution was upwards of 2.24 – 2.29 mm. The conversion from raw image to velocity field was completed in LaVision's DaVis10 and then the data were post-processed for statistics in MATLAB. All turbulence stress profiles discussed in this paper were measured using the TR-PIV system.

6. Results and Discussion

6.1. Boundary Layer Development

Figure 4 shows the streamwise and pressure gradient dependent progression of the momentum thickness θ for the rough and the smooth wall. As expected, the effect of the roughness is to increase the magnitudes of the integrated boundary layer parameters. Although a similar functional trend of pressure gradient response is seen in both the smooth and rough wall flows, the slope of the curves appears to be steeper for the rough wall, indicating that in addition to the absolute thicknesses, the rate of the boundary layer growth is increased due to the pressure drag from the roughness elements. At positive angles of attack, the naturally occurring flat plate boundary layer thickness is increased due to the presence of the initial APG flow. This is followed by a decrease in growth rate after the flow has transitioned to the FPG downstream of the airfoil quarter chord. At negative angles of attack, the flow is initially accelerated due to the FPG. This is followed by flow deceleration and an increase in the boundary layer growth rate due to the transition to APG. The integrated boundary layer parameters for the rough wall also show a crossover downstream of the pressure gradient transition, a behavior attributed to a delayed response to the upstream flow history, which was previously observed in studies of the smooth wall by Fritsch et al. (2022)

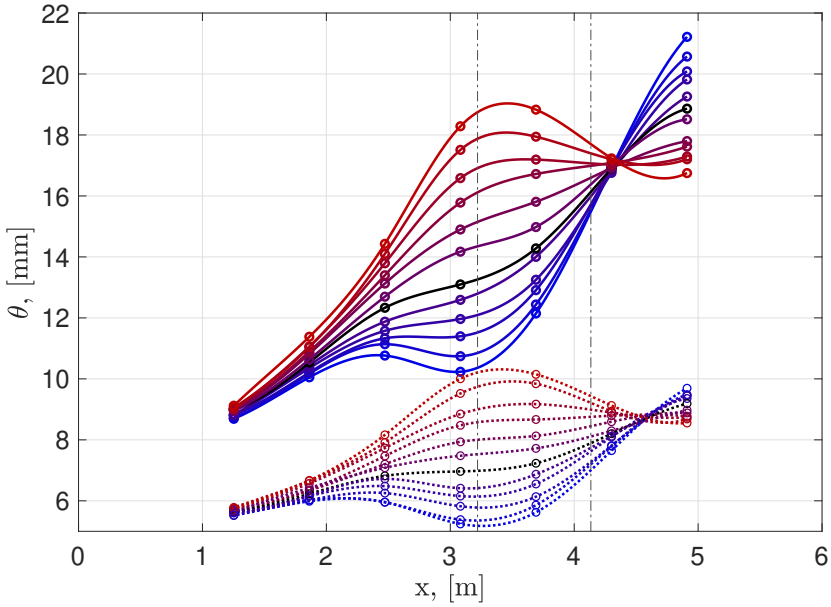

Figure 4: Momentum thickness variation with streamwise distance and NACA 0012 angle of attack. Symbol and color legend same as Figure 3.

and Vishwanathan et al. (2021) However, as the cross over occurs at at earlier streamwise station, the rough wall shows a tendency to relax to equilibrium conditions earlier than the smooth wall.

6.2. Mean Velocity Profiles

Figure 5 shows mean velocity profiles, measured using the boundary layer rake, for both the rough wall and smooth wall at $x = 2.62$ m (before the pressure gradient sign change) and at $x = 4.05$ m (after the pressure gradient sign change). The varying pressure gradient magnitudes cause the wake strength to increase with progressive streamwise locations. The effect of the roughness is to increase the shear velocity, thus causing a downward shift of the mean velocity profiles, which appears as the extra term, ΔU^+ in the law of the wall for rough wall flows. Under the outer coordinate normalization of the rough wall mean velocity profiles shown in Figure 6, the mean velocity deficit due to the impacts of the initially APG (red curves) become apparent, especially at the $x = 4.05$ m station (see bottom set of mean velocity profiles in Figure 6). At this condition, the mean velocity gradient is decreased, and the logarithmic region develops a dip in the profile shape, a deficit that is larger when the upstream APG magnitude is higher. The slope of the logarithmic region is decreased which introduces sensitivities to the mean velocity regression fits used to indirectly determine skin friction. Although not shown here, Vishwanathan et al. (2021), saw similar velocity deficit trends in the smooth wall mean velocity profiles as well.

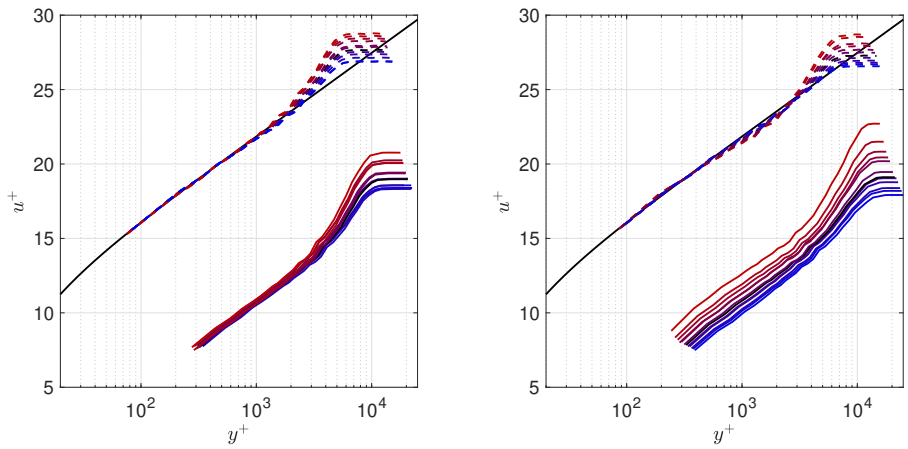

Figure 5: Mean velocity profiles normalized on inner coordinates for rough (solid colored lines) and smooth (dashed lines) configurations at (left) x = 2.62 m and (right) x = 4.05 m. Solid black line is the Spalding curve (Spalding (1961).)

6.3. Reynolds Stress Profiles

Streamwise Reynolds normal stresses measured using TR-PIV for locations before and after the pressure gradient switch (i.e. x = 2.74 m and x = 3.94 m, respectively) are shown for the rough and smooth wall flows in Figure 7. Conditions at the most adverse, favorable, and nominally zero pressure gradient conditions are plotted ($\alpha = +12^o, 10^o, 0^o$, respectively). Uncertainty bands show a combined estimate of the averaging and instrument bias uncertainty due to the under-resolution of turbulence statistics inherent to PIV measurements. At x = 2.74 m, the turbulence stress magnitudes for the initially APG flow are higher than when the flow is initially in the FPG. This trend reverses after the pressure gradient sign switch as the flow approaches the station at x = 3.94 m. In both the rough and smooth wall flows, the Reynolds normal stress magnitude is increased as the flow switches from a FPG to an APG (blue curves), and decreased as the flow switches from an APG to a FPG (red curves). For the latter pressure gradient history, a prominent outer layer peak is developed in the profiles for both wall conditions.

Varying levels of outer-layer similarity are observed at both streamwise stations. At x = 2.74 m, the β histories between the rough and smooth wall are similar, but only the initially FPG and ZPG shows profile collapse until y/δ = 0.2. However, at this station the δ/k_s parameter, plotted for the rough wall in Figure 8, is lower than minimum threshold of 40 for wall-similarity as established by Flack et al. (2005) and Jiménez (2004). For the initially APG condition (red curves), the δ/k_s parameter increases by the second PIV measurement station. The flow history for this pressure gradient is similar to that exhibited in the smooth wall, although there are variations in the absolute minimum β. At x = 3.94 m, the Reynolds stress profiles collapse very well below y/δ = 0.5, above which there are discrepancies which are hypothesized to be a combination of PIV bias uncertainty and lack of sufficient wall-normal field of view for the rough wall. The inconsistency of rough and smooth wall stress profile collapse under varying local Reynolds numbers indicates that the wall-similarity hypothesis requires multi-variable consideration, such as matching pressure gradient history between wall conditions and ensuring a sufficiently large boundary layer thickness with respect to the roughness parameters.

6.4. Wall-Similarity of the Rough Wall Flow

As direct measurements of wall shear stress are not always feasible, particularly with rough wall flows, empirical methods, such as mean velocity profiles fits and momentum integral analyses to determine skin friction from velocity field data have often been used in the literature instead. It is commonly agreed that these methods inherently have their flaws and result in high uncertainty for the computed shear velocities, u_τ (Aubertine et al. (2004)). However, in the absence of direct measurements and with the acknowledgement of these uncertainties, these methods can still provide an estimate of the shear stress in the flow. Their validity in a non-equilibrium flow environment is yet to be thoroughly evaluated. The present study uses the regression fit method by Perry and Joubert (1963) to estimate skin friction from the mean velocity profiles. In this method, the law of the wall for rough walls is rearranged in terms of the velocity normalized on the boundary layer edge velocity, U_e, such that the slope and intercept of the curve are functions of the skin friction and roughness parameter, ΔU^+. Then, the effective sandgrain roughness is computed from the following relation:

$$\Delta U^+ = \frac{1}{\kappa} ln(k_s^+) - 3.5$$

Where κ is the von Kármán constant and is taken to be 0.41.

Like many mean velocity fit methods, the resulting skin friction depends on the selection of the logarithmic region, which relies upon on engineering judgement. In an attempt to provide quantitative feedback on the selected region used for the regression fits, the logarithmic law (log-law) diagnostic function, introduced for the smooth wall by Österlund et al. (2000), is used. Due to the independence of the roughness function parameters from wall-normal position, the rough wall form of log-law diagnostic function remains the same as that of the smooth wall:

$$\Xi = \left(\frac{yU_\infty}{\nu}\right) \frac{d(U/U_\infty)}{d(yU_\infty/\nu)}$$

Figure 6 shows the log-law diagnostic function for flow conditions before and after the pressure gradient switch. The logarithmic region is considered to be within the region of constant Ξ, and provides the basis for selecting the points used in the mean velocity regression fits. By varying the number of logarithmic points, it was shown that the resulting skin friction, and by extension the roughness parameter, was sensitive to the selection of the logarithmic region. In this analysis, the number of points in the regression fit was selected by visual inspection of the log-law diagnostic function for each profile and a corresponding k_s was recomputed. The number of permutations for points considered was limited to only include points taken from the near-wall to the furthest point with constant Ξ. A 95% confidence interval using a Student's t-distribution is plotted as the error bars on Figure 9, which shows a variation of the k_s normalized on the roughness height k_g depending on the selected logarithmic region. The location that appears to have a higher sensitivity to this log-region selection is the location immediately after the flow has switched from APG to FPG, which can be attributed to the more pronounced mean velocity deficit that reduces its logarithmic shape. However, despite a lower than expected estimate of the uncertainty, there is no discernible functional dependence of the local or historical effects on the normalized sandgrain roughness parameter. This suggests that the effect of the roughness is contained within the roughness sublayer and that the non-equilibrium flow features do not impact the roughness function. Thus, within the uncertainty of the empirical method used to determine the skin friction, the k_s/k_g ratio appears to remain constant at an average value of $k_s/k_g \approx 1.60$

with pressure gradient. The response of the flow statistics on a variation of k_s/k_g magnitudes was tested such that the k_s/k_g was kept constant between the average $k_s/k_g = 1.60$ value found using the modified Clauser method discussed earlier and iterated to a $k_s/k_g = 4$, a value estimated in a simulation of the same flow. A larger k_s/k_g value resulted in higher skin frictions, but changed the estimated β history behaviors. This iterative process emphasizes the uncertainty range of possible k_s values, demonstrating that an evaluation of the k_s parameter requires direct measurements of skin friction and the criteria of the wall-similarity hypothesis must be extended to consider flow history matching between rough and smooth wall flows.

7. Conclusions

An experimental study of non-equilibrium turbulent boundary layers over rough and smooth surfaces was conducted in the Virginia Tech Stability Wind Tunnel. A NACA 0012 airfoil was used as a mechanism to induce a systematically varying family of pressure gradients on the boundary layer walls. Mean and instantaneous measurements of the velocity field were made using a boundary layer rake and time-resolved particle image velocimetry. The trend of the momentum thickness variation with streamwise development and non-equilibrium pressure gradient is very similar between the rough and smooth wall flows. However, the effect of the roughness is to increase the boundary layer magnitude and growth rate. Streamwise normal turbulence stresses show an increase in the outer layer energy after the pressure gradient switch. Indirect methods to determine skin friction, specifically using regression fits of the mean velocity profiles, show high sensitivity of the selected logarithmic region on the computed shear stresses. Despite the inherent uncertainties of such methods, there is no clear functional dependence of the effective sandgrain roughness on the flow history. It is also shown that an assessment of the wall-similarity hypothesis for rough wall flows requires a multi-variable evaluation which includes ensuring a sufficiently large boundary layer thickness to effective sandgrain roughness ratio, at least $\delta/k_s \geq 40$, as well as matching flow histories between the rough and smooth wall flows.

8. Acknowledgements

The authors would like to thank the Office of Naval Research, Dr. Peter Chang, and Dr. Julie Young for support under grants N00014-19-1-2109, N00014-18-1-2455, and N0014-20-1-2821. The authors are also grateful to VT Stability Wind Tunnel research staff and faculty, AOE Machine Shop, and fellow research students for their support and assistance in the experimental preparation and testing.

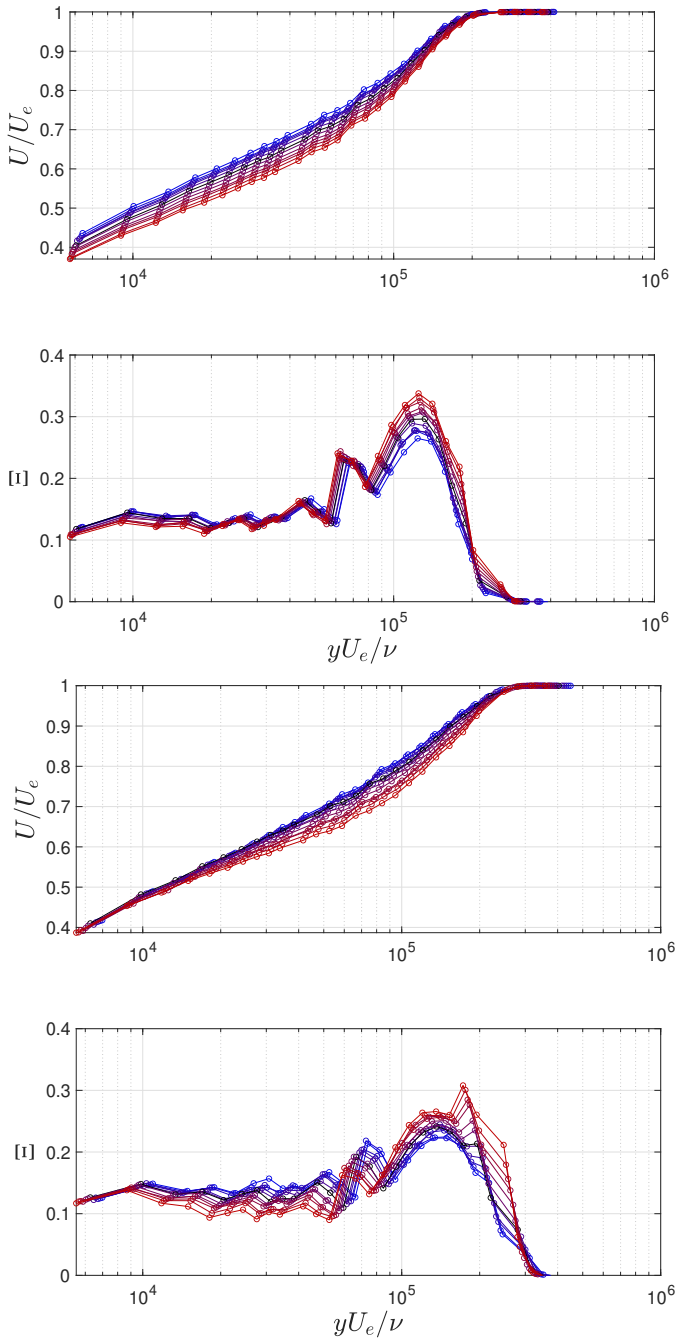

Figure 6: Rough wall mean velocity profiles in mixed outer-coordinates and logarithmic-law diagnostic function used to select the logarithmic region for regression fit methods to determine skin friction from mean velocity profiles; (top) x = 2.47 m and (bottom) x = 3.69 m.

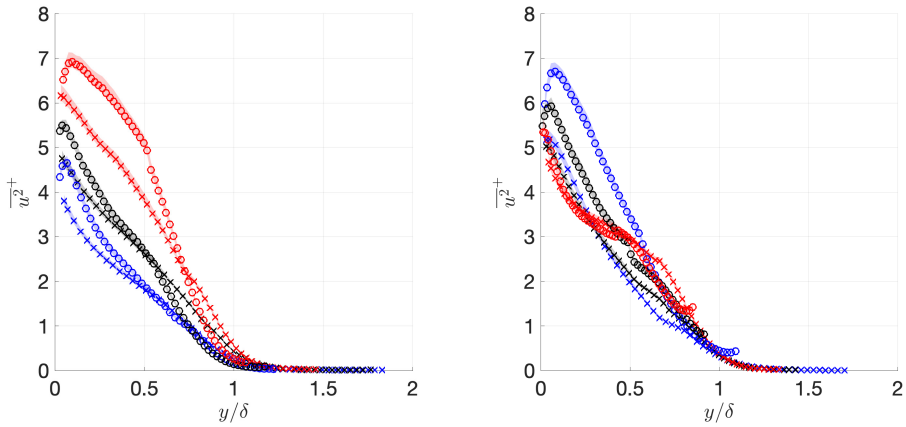

Figure 7: Reynolds streamwise normal turbulence stress plotted on inner-outer coordinates for the rough (∘) and smooth wall (x); (left) x = 2.74 m and (right) x = 3.69 m, for which the inset shows a zoomed-in view of the profiles.

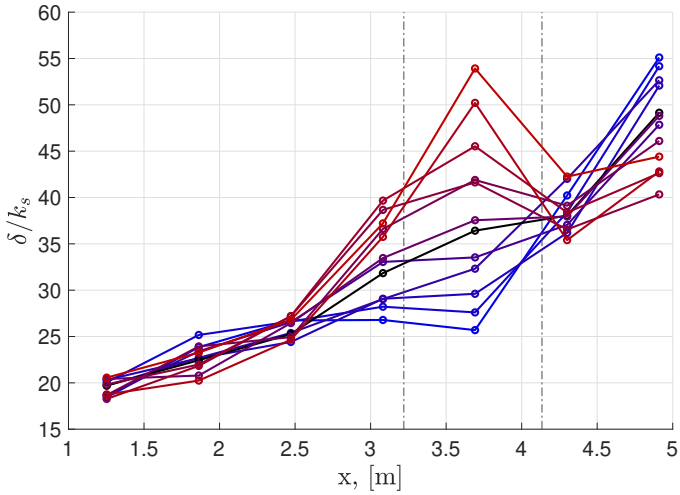

Figure 8: δ/k_s for the rough wall boundary layer. Symbol and color legend same as Figure 3.

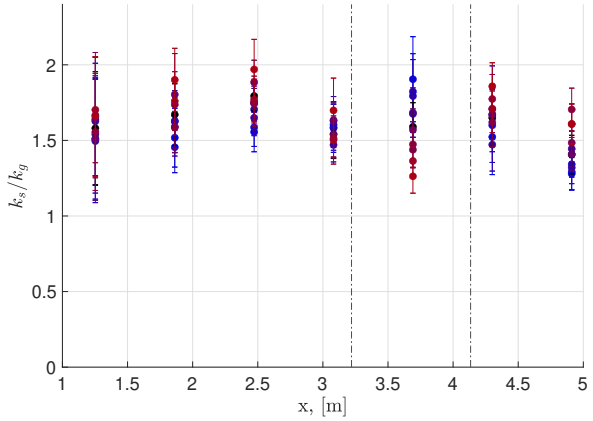

Figure 9: Effective sandgrain roughness parameter (k_s) normalized by roughness height (k_g) computed from a regression fit of the mean velocity profiles. (Top) the selected logarithmic region is custom to each flow condition, and (bottom) the logarithmic region is taken to be between $8680 < yU_e/\nu < 21270$.

References

Acharya, M., Escudier, M., 1987. Turbulent flow over mesh roughness. Springer. pp. 176–185.

Aubertine, C.D., Eaton, J.K., Song, S., 2004. Parameters controlling roughness effects in a separating boundary layer. International Journal of Heat and Fluid Flow 25, 444–450. doi:https://doi.org/10.1016/j.ijheatfluidflow.2004.02.007.

Bobke, A., Vinuesa, R., Örlü, R., Schlatter, P., 2017. History effects and near equilibrium in adverse-pressure-gradient turbulent boundary layers. J. Fluid Mech 820, 667–692.

Cal, R.B., Brzek, B., Johansson, T.G., Castillo, L., 2009. The rough favourable pressure gradient turbulent boundary layer. Journal of fluid mechanics 641, 129–155.

Castillo, L., Wang, X., 2004. Similarity analysis for nonequilibrium turbulent boundary layers. J. Fluids Eng. 126, 827–834.

Devenport, W.J., Lowe, K.T., 2022. Equilibrium and non-equilibrium turbulent boundary layers. Progress in Aerospace Sciences 131, 100807. doi:https://doi.org/10.1016/j.paerosci.2022.100807.

Finnicum, D.S., Hanratty, T.J., 1988. Effect of favorable pressure gradients on turbulent boundary layers. AIChE Journal 34, 529–40. doi:10.1002/aic.690340402.

Flack, K.A., Schultz, M.P., Shapiro, T.A., 2005. Experimental support for townsend's reynolds number similarity hypothesis on rough walls. Physics of Fluids 17, 035102. doi:10.1063/1.1843135.

Fritsch, D.J., Vishwanathan, V., Lowe, K.T., Devenport, W.J., 2022. Fluctuating pressure beneath smooth wall boundary layers in nonequilibrium pressure gradients. AIAA Journal 0, 1–19. doi:10.2514/1.J061431.

Jiménez, J., 2004. Turbulent flows over rough walls. Annual Review of Fluid Mechanics 36, 173–196. doi:10.1146/annurev.fluid.36.050802.122103.

Krogstad, P., Antonia, R.A., Browne, L.W.B., 1992. Comparison between rough- and smooth-wall turbulent boundary layers. Journal of Fluid Mechanics 245, 599–617. doi:10.1017/S0022112092000594.

Mehdi, F., Klewicki, J.C., White, C.M., . Mean momentum balance analysis of rough-wall turbulent boundary layers, Elsevier B.V.. pp. 1329–1337. doi:10.1016/j.physd.2009.06.008.

Perry, A.E., Joubert, P.N., 1963. Rough-wall boundary layers in adverse pressure gradients. Journal of Fluid Mechanics 17, 193–211. doi:10.1017/S0022112063001245.

Raupach, M.R., Antonia, R.A., Rajagopalan, S., 1991. Rough-wall turbulent boundary layers. Applied Mechanics Reviews 44, 1–25. doi:10.1115/1.3119492.

Schultz, M.P., Flack, K.A., 2005. Outer layer similarity in fully rough turbulent boundary layers. Experiments in Fluids 38, 328–340. doi:10.1007/s00348-004-0903-2.

Spalding, D.B., 1961. A single formula for the "law of the wall". Journal of Applied Mechanics 28, 455–458. doi:10.1115/1.3641728.

Townsend, A., 1980. The structure of turbulent shear flow. Cambridge university press.

Vishwanathan, V., Fritsch, D.J., Lowe, T.K., Devenport, W.J., 2021. Analysis of Coherent Structures over a Smooth Wall Turbulent Boundary Layer in Pressure Gradient Using Spectral Proper Orthogonal Decomposition. doi:10.2514/6.2021-2893.

Österlund, J.M., Johansson, A.V., Nagib, H.M., Hites, M.H., 2000. A note on the overlap region in turbulent boundary layers. Physics of Fluids 12, 1–4. doi:10.1063/1.870250.

Chapter 5

Analysis of Coherent Structures In Rough and Smooth Wall Turbulent Boundary Layers in Pressure Gradient

The contents of this chapter contain a manuscript in the *AIAA* submission format. The main objective of this paper is to reveal the distribution and content of energetic turbulence structures in a rough and smooth wall boundary layer induced by a non-equilibrium pressure gradient using spectral proper orthogonal decomposition.

Analysis of Coherent Structures In Rough and Smooth Wall Turbulent Boundary Layers in Pressure Gradient

Vidya Vishwanathan *, Daniel J. Fritsch †, K. Todd Lowe‡, and William J. Devenport§
Virginia Tech, Blacksburg, VA, 24060, USA

Results from time-resolved PIV data of high Reynolds number turbulent boundary layers over rough and smooth walls in a systematically varying non-equilibrium pressure gradient family are analyzed. A novel approach to systematically generate a family of pressure gradients on a flat wind tunnel wall adjacent to an airfoil, is done by rotating an airfoil at varying angles of attack ranging from -10° to $+12^o$. The mean velocity, integrated boundary layer parameters, and Reynolds shear and streamwise wall-normal stresses show delayed outer layer responses due to the impact of the upstream flow histories. Qualitative analysis of the instantaneous and fluctuating velocity features reveal existence of commonly recognized hairpin vortex packets which increase in size with distance from the wall, consistent with Townsend's attached eddy hypothesis. Qualitative observations of the spectral modal shapes and instantaneous velocity fields indicate effects of shear stresses acting on the boundary layers at the different pressure gradient conditions, but do not immediately give indication of the stress bore behaviors observed in the Reynolds stresses. The rough and smooth wall boundary layers are qualitatively similar in their response to pressure gradient flow history, but exhibit significant differences in velocity structure for equivalent streamwise and wall-normal locations.

Nomenclature

β	=	Clauser pressure gradient parameter normalized on displacement thickness, $\frac{\delta^*}{\tau_w}\frac{\partial p}{\partial x}$
C_p	=	Coefficient of pressure
N_b	=	Number of bins per window
Q	=	Snapshot data matrix
S_k	=	Cross-spectral density tensor at frequency f_k
Δt	=	Time between data snapshots
U_∞	=	Inflow freestream velocity

*Graduate Research Assistant, Crofton Department of Aerospace & Ocean Engineering, and AIAA Student Member.
†Graduate Research Assistant, Crofton Department of Aerospace & Ocean Engineering, and AIAA Student Member.
‡Professor, Crofton Department of Aerospace & Ocean Engineering, AIAA Associate Fellow.
§Professor, Crofton Department of Aerospace & Ocean Engineering, AIAA Associate Fellow.

u	=	Streamwise fluctuating velocity
v	=	Wall-normal fluctuating velocity
δ	=	Boundary layer thickness
ν	=	Kinematic viscosity
κ	=	von Kármán constant
k_g	=	Roughness height
k_s	=	Effective sandgrain roughness
u_k	=	Snapshot data vector for the $k^t h$ entry
w	=	Scalar weighting constants
Λ	=	SPOD eigenvalue (mode)
Ψ	=	SPOD mode energy

I. Introduction

Turbulent boundary layers are ubiquitous phenomena in nature and in any flows of practical interest. A physically intuitive method to understanding these flows is to observe and analyze the response of coherent structures to the boundary conditions imposed on the flow fields. Turbulent eddies, (i.e. stochastic vortical motions of varying lengthscales), are principal mechanisms for momentum transport via Reynolds shear stresses which help produce and dissipate turbulent kinetic energy (TKE). However, due to the random and chaotic motions, turbulence visualization and simulation is often a process of identifying the dominant motions responsible for energy containing features that largely contribute to the flow characteristics. Through the years, several experimental and computational studies have identified common eddy features and shapes and the change in their structure depending on position with respect to a wall boundary and outer layer forcing conditions, but most of these boundary layer visualizations have occurred in relatively simple flows, i.e. smooth, flat plates, or flows with uni-directional pressure gradient, which rarely exist outside of controlled laboratory environments. Improvement of the physical intuition of turbulence behaviors in flow conditions of practical interest such as over roughness and varying pressure gradients will assist in a quantitative reasoning in flow analysis.

One of earliest cited works in turbulence visualization is often attributed to Theodorsen [1] who is known to have been the first to introduce the concept of a horseshoe vortex which he characterized as an arch shaped vortex filament oriented streamwise to the flow direction. The hairpin paradigm entails a streamwise/wall-normal cross-section of the flow where the hairpin is characterized by a compact vortical region (the head), a region of ejection (i.e. Q2 flows in quadrant analysis) perpendicular to the plane of the vortex head, and a low-speed streak, parallel to the flow direction [2, 3]. Depending on the exact size, elongation, and separation of the legs creating the arch, this feature shape has

been dubbed by many terms including the “hairpin vortex.” The hierarchy of turbulent boundary layer flow features established by the flow visualization work by Robinson [4], Kline et al. [5], amongst others, explain the dominance of hairpins in the wake or outer region of the boundary layer. Low-momentum, “quasistreamwise” vortices exist in near-wall regions, followed by a mixture of both features in the logarithmic layer. The concept of the hairpin vortex has since been evaluated and experimentally and computationally exhibited in turbulent flows [6–10]. Yet, as alluded earlier, the identification of the hairpin seems a bit arbitrary and up for judgement, and the exact development of these flow features remains to be universally agreed upon.

A majority of studies have focused on the smooth wall boundary layer, but rarely does a turbulent boundary layer exist in isolation from external perturbations or compounding flow histories. A hydrogen bubble flow visualization over varying rough wall geometries in a channel flow by Grass [11] showed ejection and sweep motions common to smooth wall features observed by Kline et al. [5]. However, Grass [11] observed a marked increase of low momentum ejection due to the roughness, which they observed to be strong enough to extend over the entire thickness of the boundary layer, but in a later investigation performed at a higher level above the roughness sublayer, Grass et al. [12] noted a tendency of the rough wall flow to "order itself" and return to an "undisturbed" flow with increasing vertical distance from the wall. The implications of these observations are consistent with the idea of Townsend’s wall-similarity hypothesis, which suggests that, outside of the immediate roughness vicinity, the flow behaves as a smooth wall layer with equivalent scale characteristics. The quantitative versus qualitative validity of this hypothesis is widely disputed, although given a certain criteria for boundary layer thickness to roughness parameter ratios, several studies of rough wall, zero pressure gradient (ZPG) flat plate and channel flows have demonstrated a collapse of mean velocity and turbulence statistics between rough and smooth wall flows [13, 14]. The comparability of rough and smooth wall flows becomes a little more complicated in non-equilibrium conditions where the flow history becomes a major factor in the local boundary layer behaviors, which has already been demonstrated in studies of non-equilibrium smooth walls [15, 16]. But there is significant gap in the literature regarding rough wall, non-equilibrium flows.

By comparing the eddy structures developing in non-equilibrium boundary layers over rough and smooth surfaces, one can improve the understanding of the wall-similarity hypothesis by identifying qualitative versus quantitative variations between the wall conditions. The inherent complexity of turbulent motions requires a decomposition of the mean and fluctuating statistics to identify flow features responsible for the dominant characteristics of the boundary layer. Proper orthogonal decomposition (POD) is widely used for resolving spatially dependent coherent structures in turbulent flow data [17]. This method reduces data by producing spatially orthogonal modes to compose the spatial correlation tensor. [18] demonstrated the use of POD on a direct numerical simulation (DNS) of wall-bounded turbulent flow to identify instantaneous hairpin vortical structures that appear with high spatial frequency in the flow data. However, the POD process causes nonsequential ordering of the data snapshots, thus losing the time-dependence aspects of the data [19]. Another spectral analysis tool, dynamic mode decomposition (DMD) does the exact opposite to POD, thus losing

the spatial correlations. Although relatively new, spectral POD (SPOD), computed in the frequency domain of POD, resolves structures that evolve both spatially and temporally. As turbulent flow is also time dependent, SPOD serves as a more comprehensive data analysis technique. In the SPOD method, there is an additional time constraint to separate the behaviors at various frequencies and energies [20]. SPOD has been shown to be a more effective tool for unsteady flow analysis than either POD and DMD, as shown in a turbulent jet simulation as part of an explanation of the method by [21].

This paper seeks to expand the current knowledge of the velocity field and turbulent structures in turbulent boundary layers over rough and smooth surfaces by identifying qualitative similarities and differences in the response to a non-equilibrium pressure gradient field. This entails an analysis of the development of mean and fluctuating velocity profiles and characteristic boundary parameters parameters in a systematically varying streamwise pressure gradient. The structure of the paper is as follows. A short explanation of the SPOD algorithm as established by [21] is provided in section II. Then, the experiment configuration in section III is followed by a summary of experimental results and discussion regarding the pressure gradient effects on mean pressure, mean velocity, and turbulence statistics in section IV. Observations from the SPOD performed on the TR-PIV data sets and the distribution of energy in the turbulent flow features are also discussed and are followed by concluding remarks.

II. Analysis Method

This research study aims to apply the methods of spectral proper orthogonal decomposition (SPOD) to correlate recognized flow behaviors in a turbulent wall boundary layer under pressure gradient in both the spatial and temporal domains. A qualitative approach is used to evaluate the boundary layer differences in flows experiencing adverse versus favorable pressure gradients and qualitatively compare the modal energies contained within the most dominant modes of a characteristic frequency common across the same wall condition. This section provides a brief summary of the SPOD algorithm implemented in this study, which is an adapted version of the `spod()` MATLAB algorithm developed by [21], which implements Welch's method for spectral density estimations. As introduced in the previous section, SPOD is computed in the frequency domain of POD analysis, and a high-level explanation of the method with context to the present PIV experimental data is provided discussed, and specificity of numerical methods and range of the algorithm capacity are not discussed. The primary assumption for SPOD is that the flow field is statistically stationary, i.e. the mean and variance are assumed to be constant in time.

A set of $24,839$ image realizations were measured in the PIV experiment at a high-speed sampling frequency f_s, of 12.85 kHz. The full set of the time-resolved data is organized temporally in a matrix Q, where each snapshot of the instantaneous velocity vectors from the PIV frame is represented by u_k, where k represents the counter for each image realization.

$$Q = \begin{bmatrix} u_1(\vec{x},t) & u_2(\vec{x},t) & u_3(\vec{x},t) & \dots & u_N(\vec{x},t) \end{bmatrix} \tag{1}$$

The data matrix is then discretized into a number of windows or "blocks" (N_b), where each block has an assigned 256 snapshots (N_f). The windowing step is critical in avoiding spectral leakage of the data. Depending on the application, the windows can overlap. In this study, the default windowing methods of the [21] algorithm are implemented; there is a 50% overlap of each record block, which are weighted using a Hamming window in the time domain. Then, a fast Fourier transform (FFT) is performed on this weighted matrix to compute the discrete Fourier transform (DFT), as shown in equation 3.

$$Q^b = \begin{bmatrix} u_1^b(\vec{x},t) & u_2^b(\vec{x},t) & u_3^b(\vec{x},t) & \dots & u_{N_f}^b(\vec{x},t) \end{bmatrix} \tag{2}$$

$$\hat{Q}^b = FFT(Q^b) \tag{3}$$

The windowed and Fourier transformed data matrices, $\hat{Q}^b$, are compiled for each discrete frequency f_k where w represents a series of scalar weights to avoid complications caused by any non-periodic behavior in each data matrix block [19].

$$\hat{Q}_{f_k} = \frac{\Delta t}{\Sigma w^2} \begin{bmatrix} \hat{u}_1^b(\vec{x},t) & \hat{u}_2^b(\vec{x},t) & \hat{u}_3^b(\vec{x},t) & \dots & \hat{u}_{N_f}^b(\vec{x},t) \end{bmatrix} \tag{4}$$

The cross spectral density (CSD), S_k tensor is computed from the above transformed data matrix.

$$S_{f_k} = \hat{Q}_{f_k} * \hat{Q}_{f_k}^T = \theta_{f_k} * \tilde{\Lambda}_{f_k} * \theta_{f_k}^T \tag{5}$$

Finally, the SPOD modes are computed from the spectral eigenvalue decomposition of the CSD tensor.

$$\tilde{\Psi}_{f_k} = \tilde{Q}_{f_k} * \theta_{f_k} * \tilde{\Lambda}_{f_k} \tag{6}$$

The real parts of the SPOD modes are plotted for a characteristic frequency to compare the coherent structures appearing in the most dominant mode.

III. Experimental Facility & Setup

A. Virginia Tech Stability Wind Tunnel

The data discussed in this paper were acquired in experiments conducted in the Virginia Tech Stability Wind Tunnel. It is a continuous, single return, subsonic wind tunnel that has interchangeable test configurations; anechoic Kevlar walled, and aerodynamic, hard-walled test section, the latter of which was used in this study [22]. The test section is 7.32 m long with a 1.85 m x 1.85 m square cross section. The side walls consist of 0.61 m × 0.61 m modular square panels, arranged in a grid pattern that can be removed and replaced with panels with custom instrumentation. The tunnel is capable of reaching flow speeds up to 80 m/s, and a Reynolds number per meter of approximately 5 million. The empty tunnel, freestream turbulence levels are on the order of only 0.031% at 57 m/s, owing to seven turbulence reducing screens in the settling chamber.

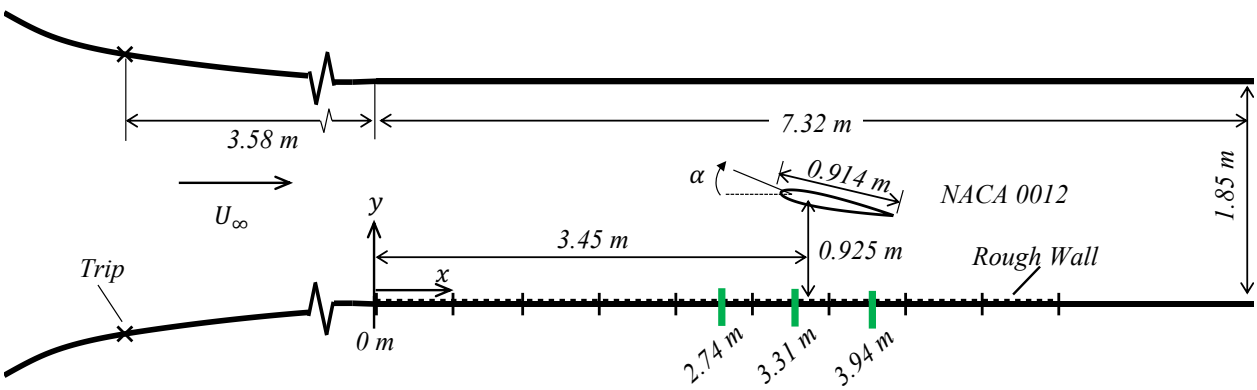

Fig. 1 Top-down schematic of test section. Boundary layer wall of interest is the "port" wall, seen here as the lower wall. Green lines indicate locations of TR-PIV planes corresponding to stations maximum upstream and downstream $\partial p/\partial x$) at x = 2.74 m and x = 3.94 m, and at the maximum p at x = 3.31 m.

B. Airfoil Geometry

A 0.9144 m chord NACA 0012 airfoil rotated to both negative and positive angles of attack generated a systematically varying family of pressure gradients on the test section wall. The airfoil quarter chord is positioned, at x = 3.45 m and y = 0.925 m with respect to the coordinate origin, as indicated in Figure 1. The wall experiences both an adverse and favorable pressure gradient, but the behavior after the station adjacent to the quarter chord depends on the angle of attack. Although both test walls experience the same nominal pressure gradient histories because of the symmetric airfoil, the research surface on the suction side of the airfoil corresponds the lower wall in Figure 1.

C. Roughness Geometry

A portion of the rough surface used in this study is shown in Figure 2. The surface entails a staggered pattern array of circular cylindrical elements that have a roughness height of k_g = 2 mm and diameter of 3.14 mm and are periodic on a 0.61 m x 0.61 m pattern (corresponding to the size of the removable test section panels). As shown in the test schematic in Figure 1, the rough wall starts at the test section entrance and extends 5.43 m downstream covering the entire test section wall. The elements are spaced s = 6.93 mm apart in the streamwise direction, and half this distance in the spanwise direction. The roughness elements were fabricated from epoxy using high-density polyethylene (HDPE) molds that were CNC milled with insets in the element shape. The mold was then overlaid on an aluminum test section panel and vacuum bag sealed for 24 hours of cure time. For ease of fabrication, the cylindrical element tips were tapered by 1°. Given current skin friction estimates computed from regression fits using a modified Clauser method for the rough wall law of the wall, the roughness Reynolds number at the stations of PIV measurements discussed in the present study ranges between k_s^+ = 314 – 478. Thus, this flow is in the fully rough regime.

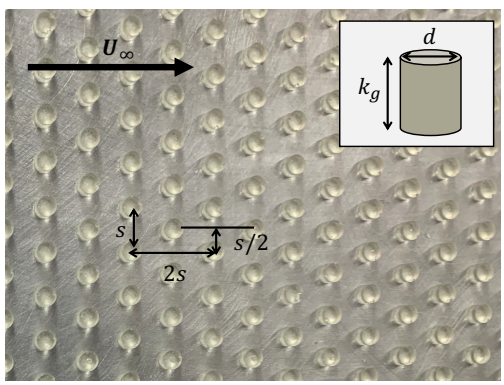

Fig. 2 Staggered, circular cylindrical roughness configuration used in this study; s = 6.93 **mm,** d = 3.14 **mm,** k_g = 2 **mm. Inset shows features of a cylindrical element.**

D. Experimental Systems

1. Time Resolved Particle Image Velocimetry (TR-PIV)

In order to implement SPOD, which requires time-dependent flow realizations, this study acquires turbulence statistics using stereoscopic TR-PIV. This non-intrusive measurement technique involves high-speed imaging of illuminated particles injected into the flow, which are then image-correlated to determine flow speeds and features. The TR-PIV data were measured at three streamwise positions highlighted in green in Figure 1. These planes correspond to the locations of upstream and downstream maximum pressure gradient, at x = 2.74 m and 3.94 m respectively, and the location of maximum pressure at 3.31 m. The flow-field was seeded using an MDG fog-generator that uses a neutral fog fluid composed of a highly refined and filtered mineral oil base with particle diameters between 500-700 nm. A laser-sheet was emitted through and perpendicular to the boundary layer wall using a Photonics Nd:YAG dual cavity

diode pumped solid state, high repetition rate laser emitting 532 nm light at 15 mJ/pulse. A Phantom v2512 camera, equipped with a 300 mm Nikon lens, recorded 24, 839 realizations in double-frame mode. The mean statistics presented in this paper were measured at a 1 kHz sampling rate and at a higher frequency of 12.85 kHz for the time-resolved SPOD results. The measurements of the mean statistics were also made with two image resolutions which were concatenated to create a cohesive profile; the outer region data were measured with a baseline 300 mm Nikon lens, and the inner region data were measured with the addition of Vivitar 2× teleconverter lens to the baseline lens to doubly magnify the field of view. This produced results that were resolved to 1.06 – 1.09 mm in the near wall and 2.24 – 2.29 mm in the outer wall. Further information regarding this process can be found in Vishwanathan *et al.* [23]. The data were processed in LaVision's DaVis10 using two initial passes of a 64x64 $pixel^2$ interrogation window with 50% overlap, which was followed by two final passes of a 24x24 $pixel^2$ interrogation window with a 75% overlap.

2. Mean Pressure Measurements

The two hard sidewalls of the test section were equipped with 82 static pressure taps each. The taps were carefully flush mounted to the inner wall and had 0.1 mm inner diameter. The mean surface pressure distributions were measured using an Esterline 9816/98RK pressure scanner with a range of ± 10" H_2 0 and a 32-channel DTC Initium scanner with a range of ± 4" $H_2$0. The reference pressure was measured as the ambient pressure in the control room.

Figure 3 shows the distribution of normalized pressure and pressure gradient on the instrumented portions of the center streamline on the research wall for the rough and smooth wall test cases. The pressures include the contribution of the naturally occurring flat-plate pressure gradient of the test section in addition to the airfoil generated pressure gradients. At positive angles of attack the port wall experiences an adverse pressure gradient which switches to a favorable pressure gradient at a streamwise station approximately adjacent to the airfoil quarter-chord. The opposite phenomena are experienced by the wall in negative angles of attack.

3. Experimental Conditions

To generate both the adverse and favorable wall pressure gradients, the airfoil was rotated through a sequence of nominal angles of attack between -10° and $+12^o$. This corresponded to Clauser pressure gradient parameters varying between $-0.91 < \beta < +0.71$ for the smooth wall, and between $-1.06 < \beta < +1.29$ for the rough wall, where the minimum and maximum pressure gradient magnitudes are reached after the pressure gradient sign change. A majority of the discussions in this paper focus on the data measured at the pressure gradient extremes when the airfoil was at -10° (initially favorable pressure gradient), 0° (initially zero-pressure gradient), and $+12^o$ (initially adverse pressure gradient). Depending on the magnitude and pressure gradient history, the momentum-based Reynolds number varied between $12,065 < Re_\theta < 19,824$ for the smooth wall and $24837 < Re_\theta < 36835$ for the rough wall. A summary of the test conditions is provided in Tables 1 - 3.

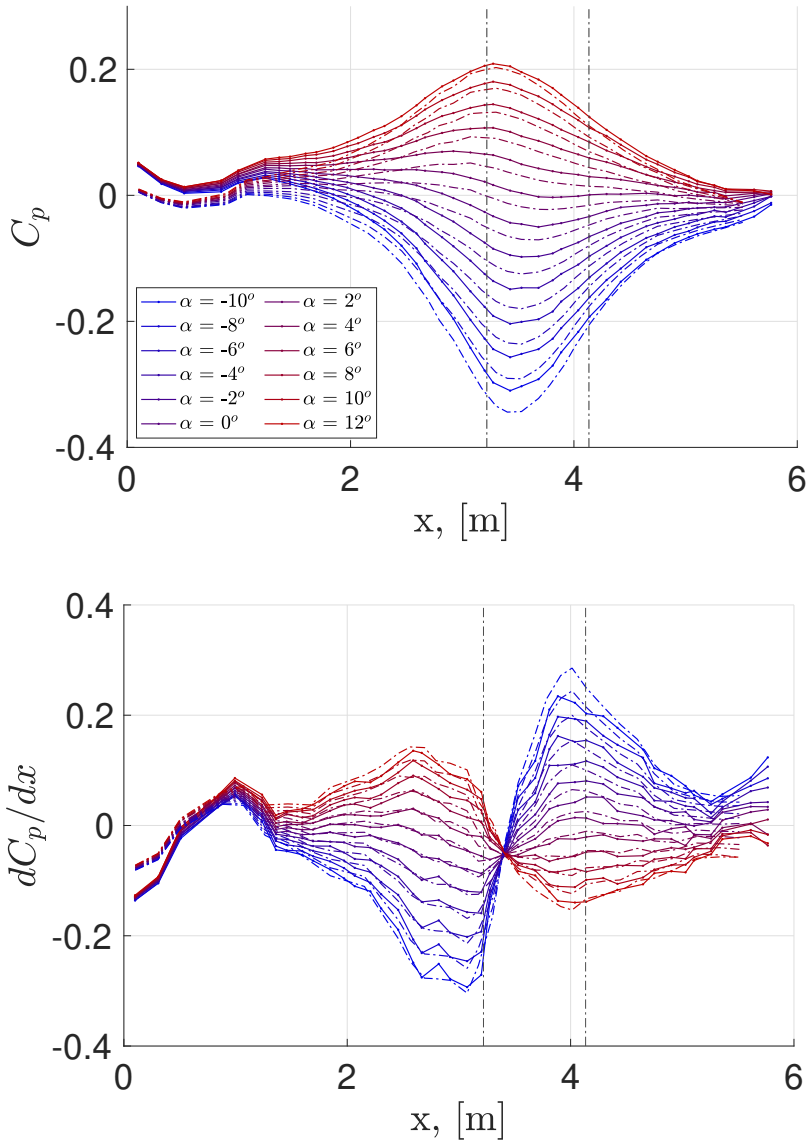

Fig. 3 Pressure coefficient (top) and pressure coefficient gradient (bottom) distributions on the research wall due to pressure gradients generated by the NACA 0012 airfoil for the rough (———) and smooth (- - - - -) wall flows. Vertical lines indicate the streamwise locations of the leading and trailing edge of the airfoil at 0° angle of attack.

Table 1 Smooth and rough wall flow parameters at x = 2.74 m.

Wall Condition	α [^{o}]	δ, [mm]	θ, [mm]	δ^*, [mm]	$C_f \times 10^3$	Re_θ	k_s^+
	-10	62.18	5.97	7.54	2.70	14348	-
Smooth	0	65.59	7.01	9.07	2.53	15549	-
	12	77.80	9.47	12.75	2.19	19228	-
	-10	87.38	10.38	16.14	6.27	24884	429
Rough	0	97.79	11.35	17.96	5.48	24837	390
	12	109.33	13.71	23.76	4.25	27395	328

Table 2 Smooth and rough wall flow parameters at x = 3.31 m.

Wall Condition	α [^{o}]	δ, [mm]	θ, [mm]	δ^*, [mm]	$C_f \times 10^3$	Re_θ	k_s^+
	-10	56.69	4.87	6.01	2.82	12065	-
Smooth	0	65.21	5.97	7.43	2.63	13491	-
	12	85.93	9.46	12.40	2.23	18405	-
	-10	96.53	11.38	17.81	6.27	28900	478
Rough	0	105.26	13.43	21.10	5.46	30257	374
	12	122.76	18.70	30.55	4.26	36835	315

Table 3 Smooth and rough wall flow parameters at x = 3.94 m.

Wall Condition	α [^{o}]	δ, [mm]	θ, [mm]	δ^*, [mm]	$C_f \times 10^3$	Re_θ	k_s^+
	-10	65.20	6.17	7.83	2.62	14982	-
Smooth	0	79.77	8.06	10.23	2.46	18305	-
	12	88.07	9.81	12.76	2.37	19824	-
	-10	100.31	13.28	21.33	5.16	31433	424
Rough	0	115.35	14.99	22.71	5.21	33178	381
	12	130.41	17.57	26.13	5.19	34975	354

IV. Results & Discussion

A. Mean Flow Behaviors

1. Boundary Layer Development

Figure 4 shows the streamwise and pressure gradient dependent progression of the boundary layer displacement thickness, δ^* compared for the rough and smooth walls. Data in this plot were acquired using both a 30-Pitot probe boundary layer rake about which more information can be found in Fritsch et al. [15]. The profile behavior shows an overall thickening of the boundary layer under rough wall conditions, but, regardless of wall condition, demonstrates the same qualitative response to the complex pressure gradient flow history. The cross over in the profiles, occurring downstream of the pressure gradient switch seen at $x \approx 3.45$ m in Figure 3, indicates non-local effects on the flow development, referred to as a "history effect" [15, 24]. This lag in response occurs earlier in the rough wall boundary layer, at $x \approx 4.20$ m as opposed to $x \approx 4.50$ m for the smooth wall, implying a more rapid return to equilibrium under the increased mixing of the rough wall boundary layer.

2. Mean Velocity

Mean velocity profiles measured using TR-PIV are shown in defect coordinates in Figure 5. The profiles are shown for three streamwise stations corresponding to the locations of maximum pressure and maximum pressure gradients upstream and downstream of the pressure gradient switch when the NACA 0012 airfoil is at -10°, 0°, and $+12^o$. In both wall conditions, an initially APG results in a higher velocity deficit than either the initially FPG or ZPG conditions,

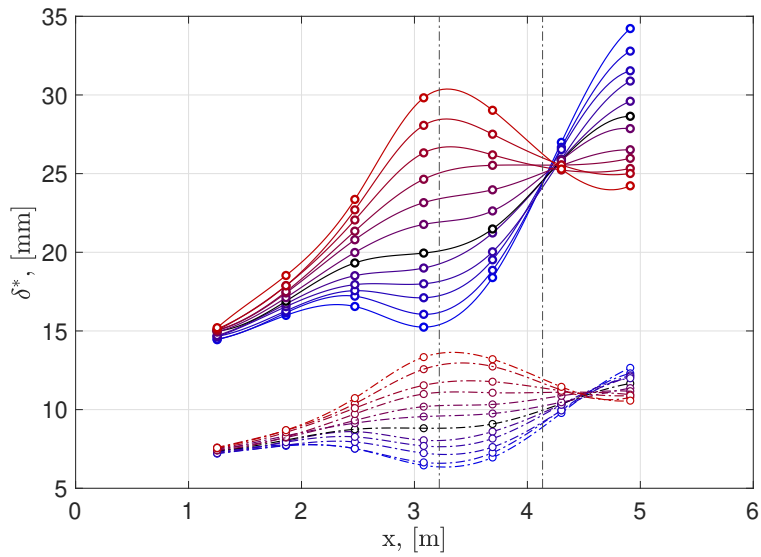

Fig. 4 Displacement thickness with streamwise position as a function of pressure gradient. Color and symbol legend same as Figure 3.

which increases with proximity to the wall. After the pressure gradient switch from FPG to APG, the apparent velocity deficit has increased, and for the rough wall, surpassed the deficit observed in the APG to FPG flow condition. This behavior is consistent with rapid relaxation to equilibrium observed in displacement thickness response to history effects seen in Figure 4, where the recovery from the pressure gradient switch occurred earlier for the rough wall flow conditions.

Good collapse is observed in the outer regions of the boundary layer prior to the pressure gradient switch, where the collapse extends below $y/\delta = 0.1$ for the measured portions of the initially favorable and zero-pressure gradient conditions. However, as the pressure gradient history starts to change, the collapse becomes less distinctive, largely for the condition that has switched from the FPG to APG (blue curves), which has completely lost semblance of similarity by the most downstream location at $x = 3.94$ m. Interestingly, the profiles with flow history from APG to FPG (red curves) shows a progressive decrease in velocity deficit and both the rough and smooth wall profiles have merged closer. The lack of consistent wall-similarity with varying local Reynolds number and pressure gradient history implies that a comparison between rough and smooth walls for wall-similarity is a complex multi-variable function requiring consideration of both the local and historical flow behaviors. An evaluation of wall-similarity based solely on mean velocity conditions is insufficient, and therefore inconclusive.

3. Reynolds Turbulence Stress

Reynolds normal and shear stresses in mixed inner-outer scaling for the flow conditions discussed in section IV.A.2 are shown in Figures 6 - 8. As explained in Section III, the mean turbulence profiles consist of concatenated profiles

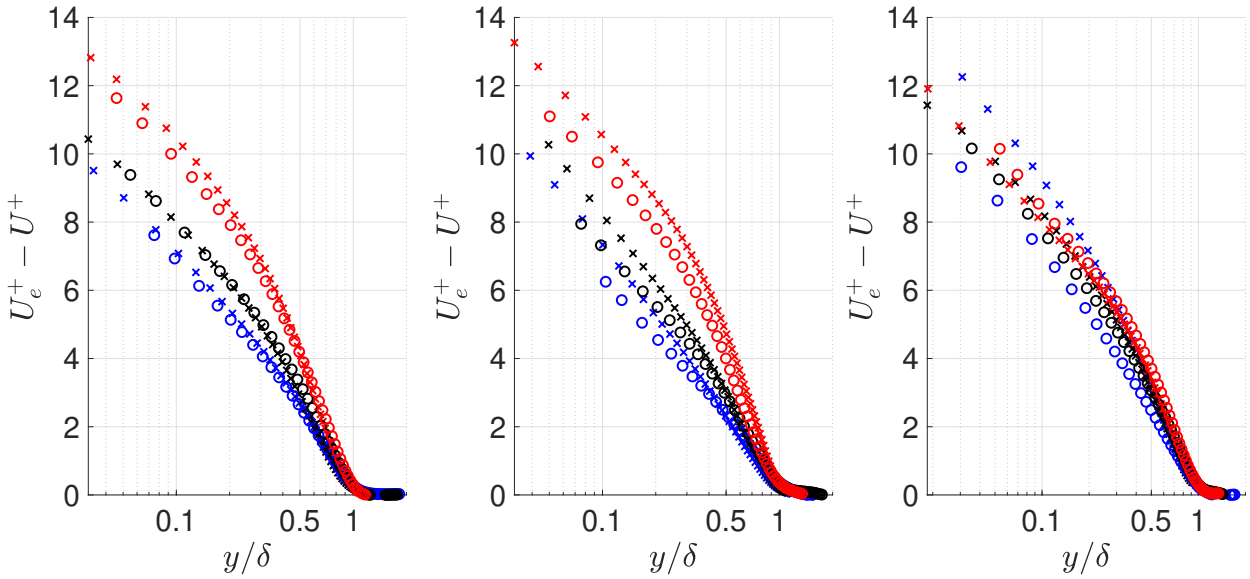

Fig. 5 Mean velocity profiles in defect coordinates at (left) x = 2.74 **m, (middle)** x = 3.31 **m, (right)** x = 3.94 **m for the smooth (○) and rough (×) wall boundary layers.**

from a fine and coarse resolution PIV configuration to reduce near-wall turbulence attenuation due to under-resolved spatial fields, which as discussed in Vishwanathan *et al.* [23], introduces bias uncertainty of the measured statistics. The point of concatenation of the profiles measured with the two fields of view varied for each condition depending on the normalized boundary layer thickness, but typically occurred between $0.5 < y/\delta < 0.8$. Turbulence stress magnitudes in all components of both the rough and smooth wall flows are higher in the initially APG condition, which start to attenuate after the pressure gradient has switched direction. In fact, the rough wall $\overline{v^2}^+$ stress, and by product, the $\overline{uv}$ stress at 3.94 m for the rough wall case shows a turbulence magnitude that is lower than even the initially FPG and ZPG conditions which is consistent with the earlier relaxation to equilibrium observed in the δ^* behavior in Figure 4. This behavior again suggests that the rough wall flow requires a shorter streamwise distance to return to equilibrium than the smooth wall. This is an important implication for computors for purposes of grid development and boundary conditions when simulating rough wall flows.

When the airfoil is at $+12^o$, the near wall turbulence stress becomes depressed, and an outer layer peak becomes more prominent in the $\overline{u^2}$ stress, occurring at $y/\delta \approx 0.5$ in both the rough and smooth wall profiles in Figure 6. This behavior is akin to the traveling hump, dubbed the "stress bore" observed in both studies of convex curvature by Smits and Wood [25] and roughness perturbations by Andreopoulos and Wood [26] and Jacobi and McKeon [27]. The stress bore gives indication of a large transport of velocities in the regions encompassed by the internal layers and a transition to new local flow conditions with the pressure gradient switch. The similarity in this stress bore behavior observed in the rough and smooth wall gives further indication that the flows under both wall conditions respond with the same qualitative characteristics but may differ in scale and magnitude. The next sections investigate the dominant, coherent

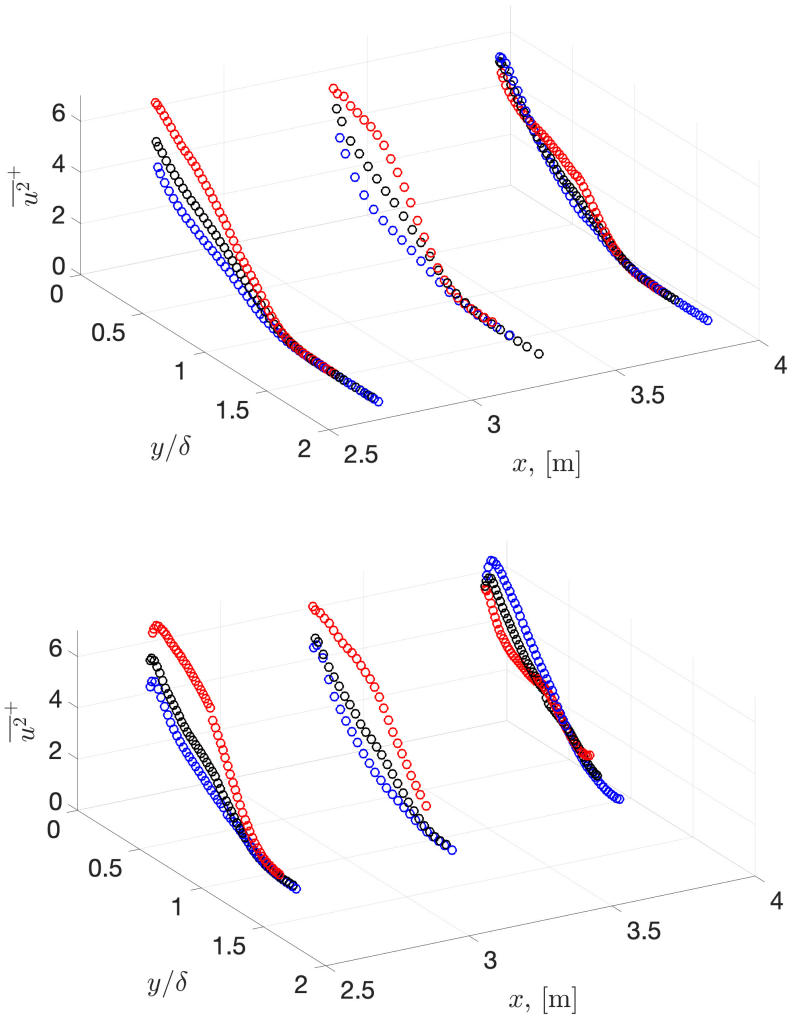

Fig. 6 Streamwise Reynolds stress for the smooth (top) and rough (bottom) wall by streamwise station and airfoil angle of attack. Color legend same as for Figure 5.

structures occurring at $y/\delta \approx 0.5$ to compare the scaled behaviors of both the rough and smooth wall and at equivalent wall-normal position.

B. Vortex Structure in Instantaneous Velocity Fields

Although qualitative, the instantaneous and Reynolds decomposed fluctuating velocity fields acquired using the TR-PIV system are rich in making observations for the flow structures. The static limitations of a paper manuscript have required a representative selection of the velocity fields for the $+12^o$ condition shown in Figure 9 for the smooth wall and Figure 10 for the rough wall at three streamwise stations, before, after, and at the apex of the pressure gradient switch from APG to FPG. The colormaps show the streamwise mean velocity fields normalized on shear velocity, the vector field shows the Reynolds decomposed instantaneous velocity field (vector scales are the same for both wall

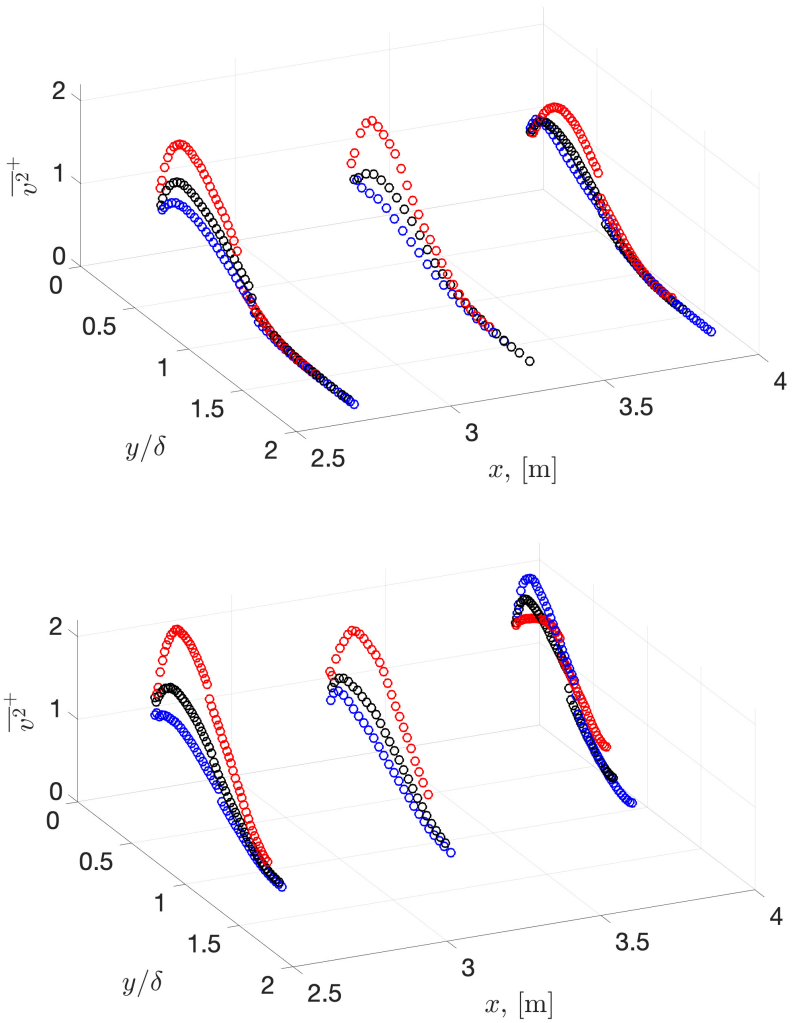

Fig. 7 Wall-normal Reynolds stress for the smooth (top) and rough (bottom) wall by streamwise station and airfoil angle of attack. Color legend same as for Figure 5.

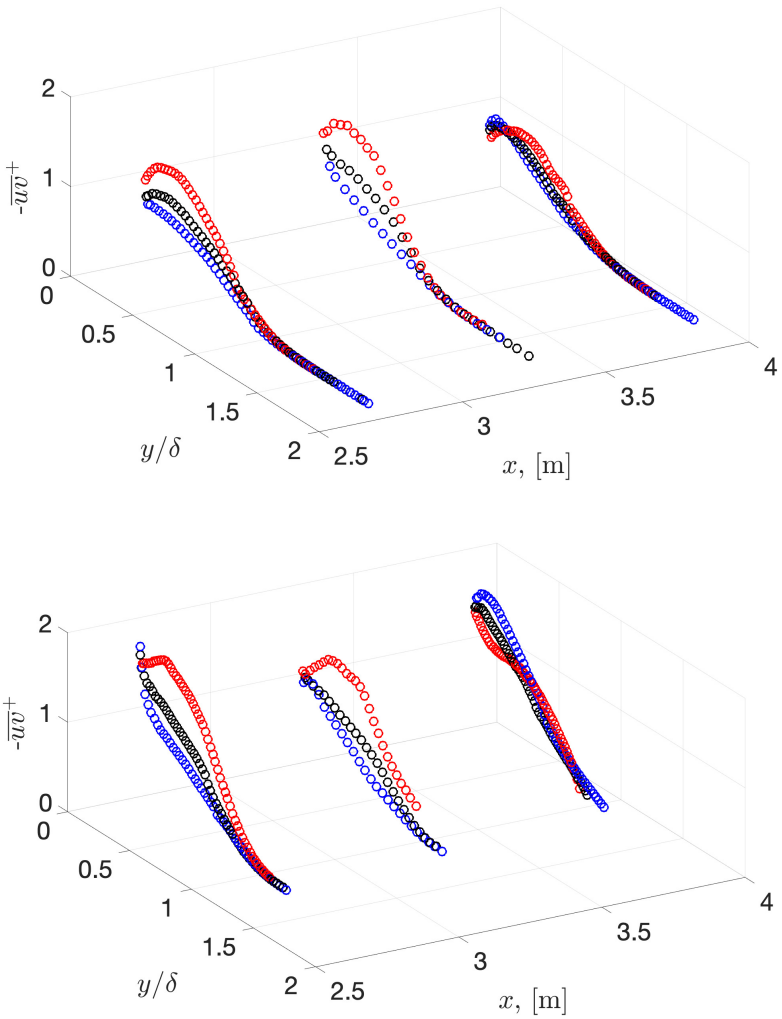

Fig. 8 Reynolds shear stress for the smooth (top) and rough (bottom) wall by streamwise station and airfoil angle of attack. Color legend same as for Figure 5.

conditions), and the spatial fields are normalized on boundary layer thickness. These specific vector fields were selected after an intensive inspection of a large selection of instantaneous images to be the most representative of recurring features of each pressure gradient and wall condition. The most obvious observation of these figures is the increase of shear velocity magnitudes of the rough wall flow, indicated by a lower overall magnitude of normalized velocity for the rough wall mean velocity field shown in Figures 9 and 10. The streamwise transitions between the APG and FPG conditions reveal much about the response of the turbulent eddies to the non-equilibrium nature of the flow field. For the smooth wall field, there is an increase in the appearance of hairpin packets, characterized in two-dimensions (2D) by vortical heads, indicated by red circles in Figures 9 and 10. The adaptation of the eddy size as it moves to the outer regions of the boundary layer is also consistent with Townsend's attached eddy hypothesis which postulates the size of the eddy to be proportional to the distance from the wall [28].

When the flow is initially at an APG, concentrated eddies are clearly distinguishable in size and shape as shown in in Figure 9(a) at $y \approx 0.45$ and $y \approx 0.6$, and at $y \approx 0.9$ in Figure 10. The instantaneous features of the flow become visually more chaotic, over both wall conditions, as the flow transitions from the APG to the FPG at $x = 3.31$ m, indicated in the center figures of the contour maps. The chaos is indicative of high levels of mixing between wall-normal layers as the vector fields exhibit large regions of ejection and sweep zones, as well as an upward progression of the hairpin vortices. At the most downstream measured station, the flow has transitioned to a FPG, shown in Figures 9(c) and 10(c), in which the immediate response near the wall is indicated by a decrease in the turbulence for the smooth wall, but a retention of the turbulent near wall features in the rough wall. For instance, the density of decomposed vectors below $y/\delta \approx 0.3$ in all three contours of Figure 10 seem to indicate a consistent roughness impact to a larger outward extent of the boundary layer despite changing external pressure gradient conditions. Although the flow has switched to the FPG, there is a natural increase in boundary layer thickness and the response to the upstream APG has rendered some of initial near wall structures to enlarge and move towards the outer regions of the wall.

As previously observed in the mean statistics, the rough wall appears to show the same qualitative response to the streamwise gradient of the pressure field, but direct comparisons of the same station between the two wall conditions suggests differences in the velocity structure due to a larger effect of the roughness in outer extents of the boundary layer.

C. Vortex Structure in SPOD Modes

The stress bore behavior observed in the Reynolds stress profiles described in the previous section motivates an investigation of the coherent structures occurring in the vicinity of this phenomenon. As identified in the previous sections, the stress bore appears to manifest itself most prominently at the most downstream station, at a $y/\delta \approx 0.5$ when the airfoil is at $+12^o$ in both the rough and smooth wall flows.

The spectral proper orthogonal decomposition (SPOD) modes for the flows corresponding to an initial APG ($+12^o$) are analyzed, where the characteristic frequency analyzed corresponds to ratio of the wall-normal mean velocity and

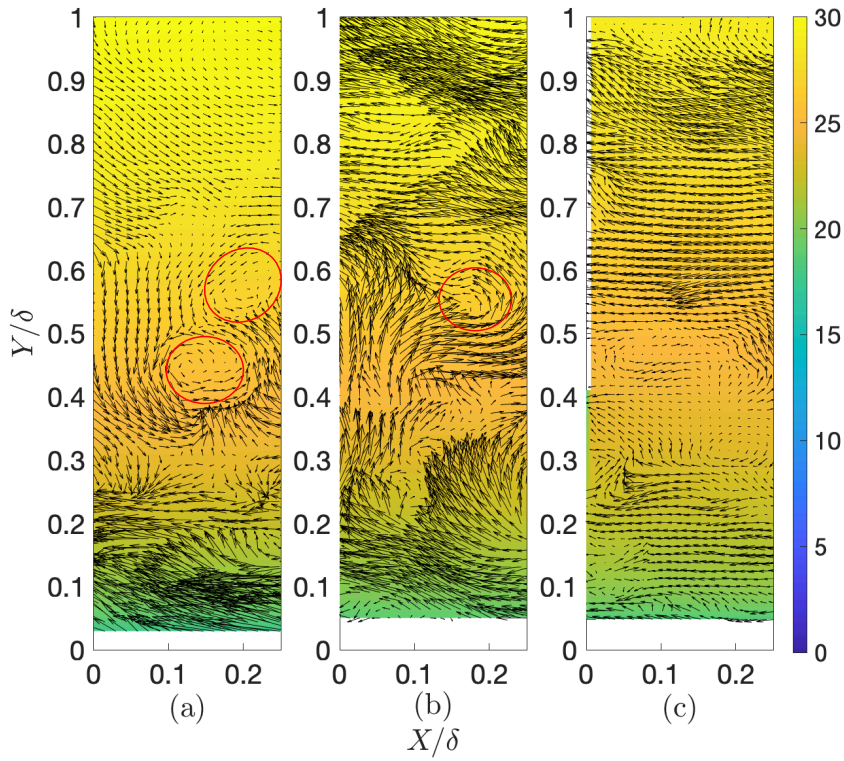

Fig. 9 See Figure 10 for caption.

position at $y/\delta = 0.5$ for each local Reynolds number and wall condition. The SPOD script used in the current work is an adaptation of the algorithm developed by Towne et al. [21]. The distribution and shapes of the modal energies normalized on the shear velocity are shown in Figures 11, 12, and 13 for three streamwise stations, where the top image of each figure corresponds to smooth wall modes and the bottom for rough wall modes. As with the instantaneous velocity contours, a representative snapshot of the SPOD modes is selected for presentation for each condition at three time steps within the period of the characteristic frequency. All displayed vector magnitudes are the same between streamwise station and wall conditions.

In the smooth wall boundary layer, the dominant modes are clear and, consistent with the observations of the boundary layer development in the previous sections, appears to move outward from the wall with streamwise development, where the modes initially appearing between $0.2 < y/\delta < 0.4$ at $x = 2.74$ m have moved to $0.4 < y/\delta < 0.6$ at $x = 3.31$ m (Figure 12). Interestingly, a new set of structures appear near the wall supplementing the ejected motions at $x = 3.94$ m (Figure 13). This progression is not obvious in the rough wall layer, where the dominant structures are elongated and dispersed throughout the layer. In fact, at the most downstream station, the dominant mode covers the entire boundary layer thickness. The implication of the distribution of these structures with respect to the location of the stress bore observed in the Reynolds stress profiles shown in Figure 6 is not so obvious. However, the clear difference in eddy

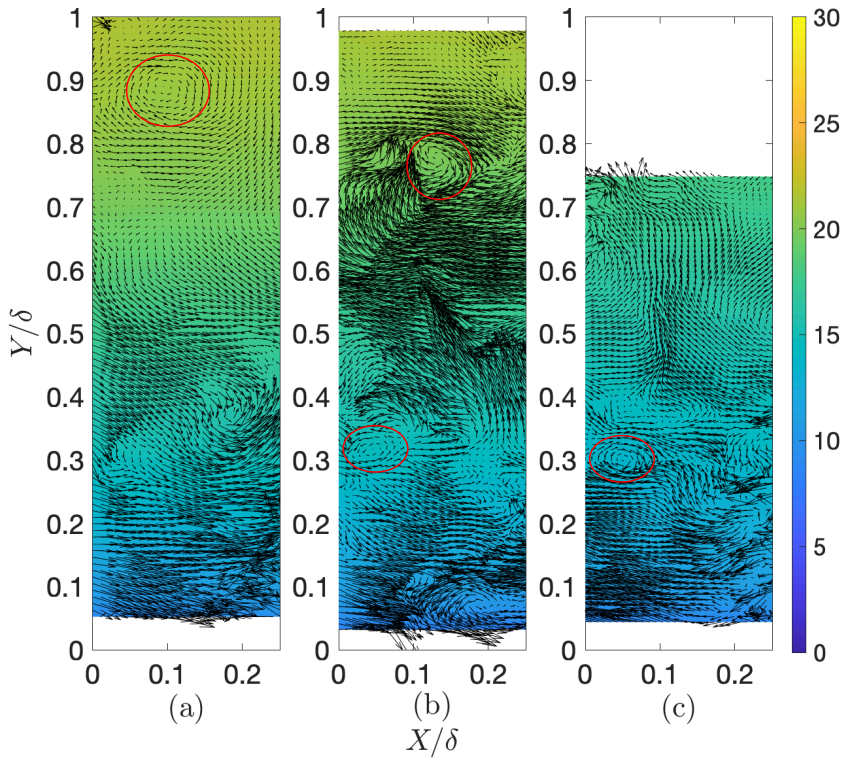

Fig. 10 Instantaneous and Reynolds decomposed fluctuating velocity fields for flows over the smooth wall (Figure 9 and the rough wall (present figure) with the airfoil at $+12^o$ at (a) $x = 2.74$ m, (b) $x = 3.31$ m, and (c) $x = 3.94$ m plotted over the color contour of the mean velocity normalized on local shear velocity ($\overline{U}/u_\tau$). Red circles indicate vortical heads of the hairpin vortices determined by visual inspection.

structure shape and distribution at all stations of the pressure gradient history suggests that, although the response of the wall boundary layer is qualitatively similar (i.e. enlargement and outward movement of eddy structure with increasingly APG flows), there appears to be a lack of direct similarity between the rough and smooth wall conditions.

V. Conclusions

The development of a high Reynolds number, smooth wall-bounded turbulent velocity field in a systematically varying pressure gradient is analyzed with experimental data acquired using time-resolved PIV. In the experimental setup, a NACA 0012 airfoil, placed at the center of the VT Stability Wind Tunnel, was swept to negative and positive angles of attack to generate a pressure gradient field on the test section wall. The negative angles of attack corresponded to an initially favorable pressure gradient on the boundary layer wall of interest, while the positive angles of attack corresponded to an initially adverse pressure gradient. The transition to the opposite pressure gradient domain occurred at the pressure apex approximately adjacent to the quarter-chord of the airfoil. However, crossover points occurring in the integrated boundary layer parameters occurred downstream of this point of pressure gradient change, which is consistent with both the rough and smooth wall flows. However, the rough wall relaxation to equilibrium occurs at an

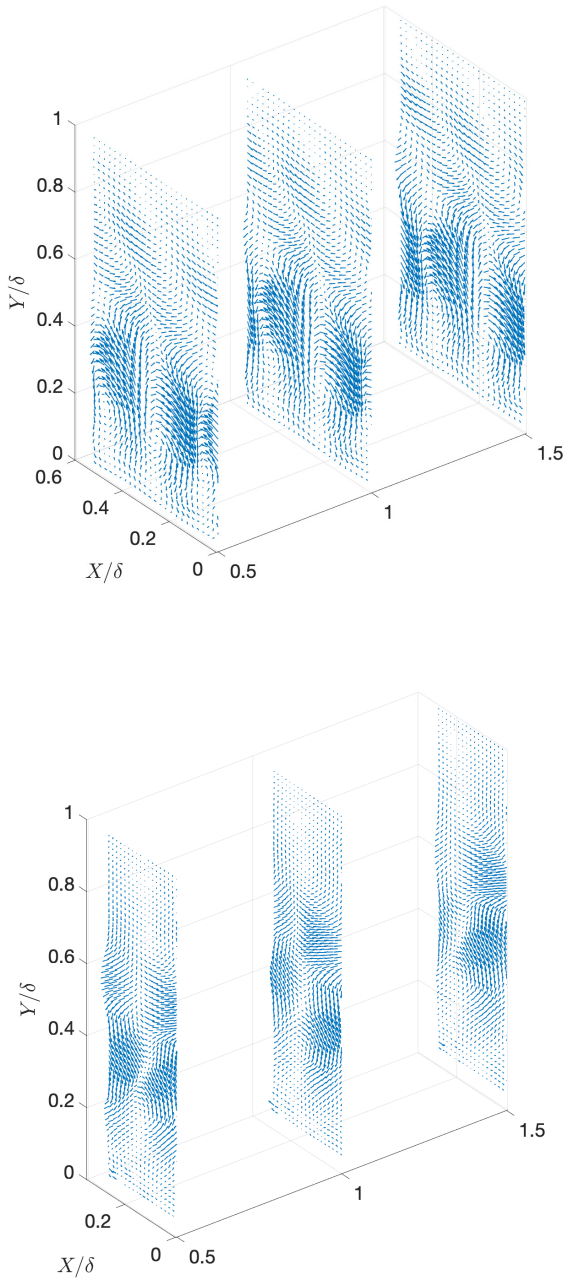

Fig. 11 SPOD modes normalized on shear velocity, u_τ, for the characteristic frequency corresponding to a $y/\delta = 0.5$ position for the smooth (top) and rough (bottom) wall at $x = 2.74$ m.

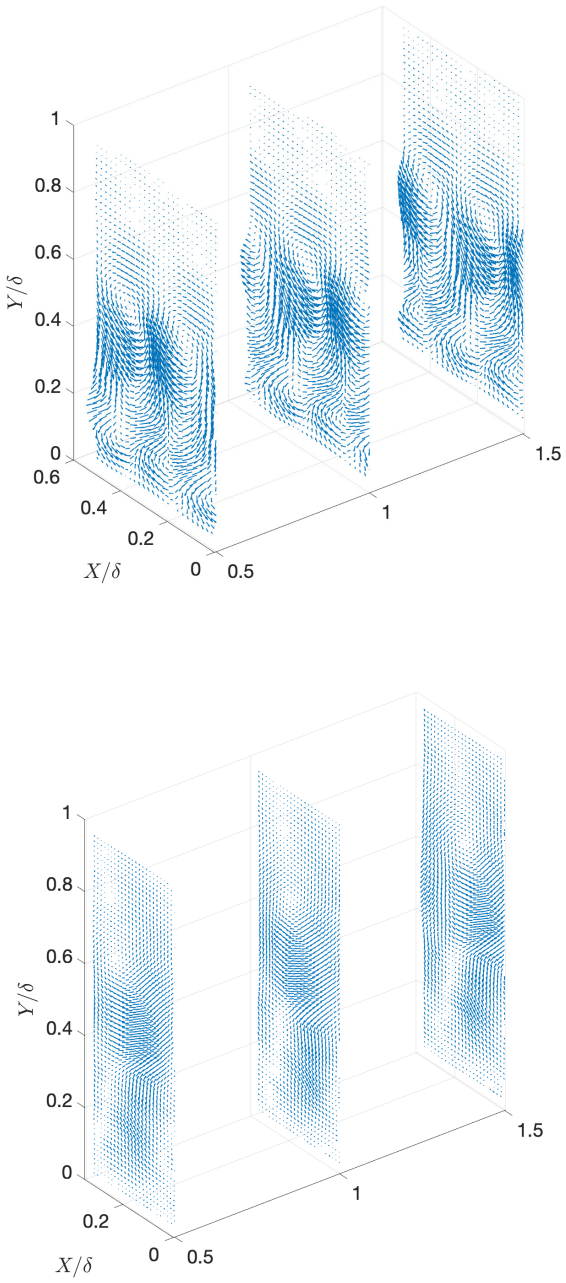

Fig. 12 SPOD modes normalized on shear velocity, u_τ, for the characteristic frequency corresponding to a $y/\delta = 0.5$ position for the smooth (top) and rough (bottom) wall at $x = 3.31$ m.

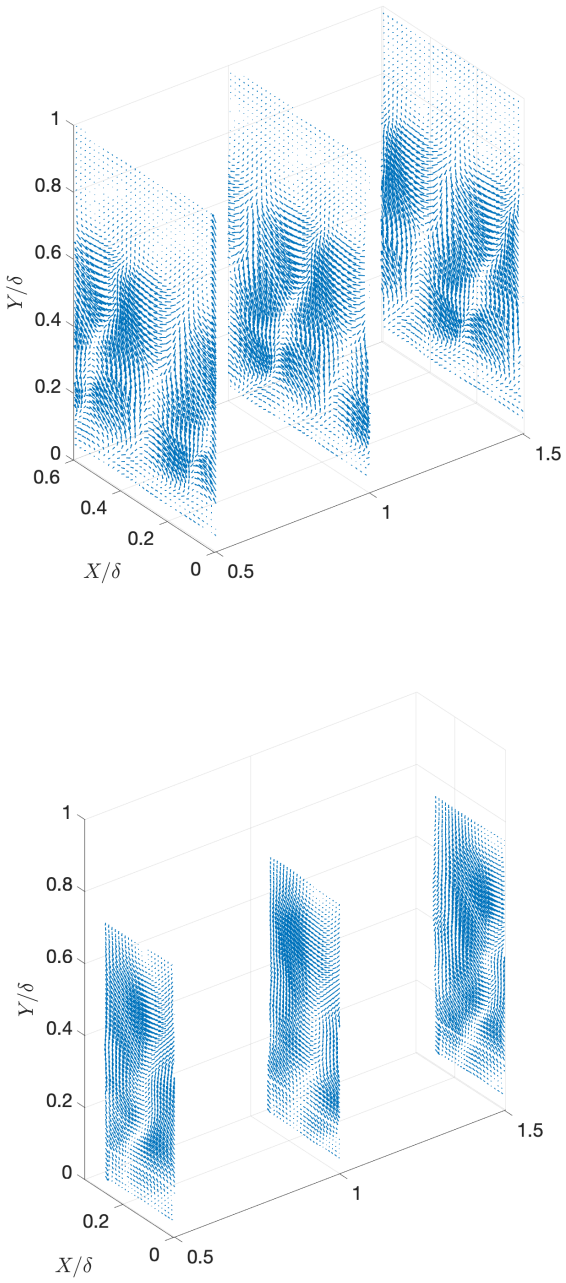

Fig. 13 SPOD modes normalized on shear velocity, u_τ, for the characteristic frequency corresponding to a $y/\delta = 0.5$ position for the smooth (top) and rough (bottom) wall at $x = 3.94$ m.

earlier sreamwise station. The velocity gradients in the mean velocity profiles show a response to the change in pressure gradient, which is consistent across both rough and smooth wall conditions. However, increasingly non-equilibrium flow history differences between the rough and smooth wall render the conditions incomparable and a comparison on the basis of wall-similarity is not valid. These delayed responses to the flow development indicate the effect of upstream flow histories on the behavior of the turbulent boundary layer.

Qualitative analysis of the instantaneous velocity fields shows the generation of hairpin vortices when the flow is in an initially adverse pressure gradient, which transitions to overwhelming indications of mixing between layers in response to the change in the pressure gradient direction. The transition to a favorable pressure gradient shows a decrease in turbulent mixing in the inner regions of the smooth wall, but the apparent effect of mixing due to the roughness layer is still visible even in the outer portions of the boundary layer. Both the turbulence stresses and SPOD modes indicate that the flows in the initially APG are more sensitive to the pressure gradient histories than those developing in the initially favorable pressure gradient. Lastly, the mode shapes and distributions of shapes across the boundary layer is varied between the rough and smooth wall. These quantitative differences between the wall conditions suggests a qualitative similarity in response to non-equilibrium flow histories, but an inability for quantitative comparison due to the lack of matching of integral parameters pertaining to the local Reynolds number and pressure gradient history.

Acknowledgments

The authors would like to thank the Office of Naval Research and Dr. Peter Chang and Dr. Julie Young under grants N00014-19-1-2109 and N00014-18-1-2455. The authors are also grateful to VT Stability Wind Tunnel research faculty and staff Dr. Aurélien Borgoltz, Dr. Mate Szöke, and William Oetjens. We thank fellow graduate research students Jarrod Banks and Surabhi Srivastava, and undergraduate assistants Mason Fitzsimmons and Sasha Mintz for their assistance during the experiments. Lastly, we are very grateful to the AOE Machine Shop, headed by James Lambert, for their support and assistance with the manufacturing and assembly of several of our integral test components.

References

[1] Theodorsen, T., *Mechanism of Turbulence*, 1952.

[2] Adrian, R. J., "Hairpin vortex organization in wall turbulence," *Physics of Fluids*, Vol. 19, No. 4, 2007, p. 041301. https://doi.org/10.1063/1.2717527.

[3] Adrian, R. J., Meinhart, C. D., and Tomkins, C. D., "Vortex organization in the outer region of the turbulent boundary layer," *Journal of Fluid Mechanics*, Vol. 422, 2000, pp. 1–54. https://doi.org/10.1017/S0022112000001580.

[4] Robinson, S. K., "Coherent Motions in the Turbulent Boundary Layer," *Annual Review of Fluid Mechanics*, Vol. 23, No. 1, 1991, pp. 601–639. https://doi.org/10.1146/annurev.fl.23.010191.003125.

[5] Kline, S. J., Reynolds, W. C., Schraub, F. A., and Runstadler, P. W., "The structure of turbulent boundary layers," *Journal of Fluid Mechanics*, Vol. 30, No. 4, 1967, pp. 741–773. https://doi.org/10.1017/S0022112067001740.

[6] Wallace, J. M., Brodkey, R. S., and Eckelmann, H., "Pattern-recognized structures in bounded turbulent shear flows," *Journal of Fluid Mechanics*, Vol. 83, No. 4, 1977, pp. 673–693. https://doi.org/10.1017/S0022112077001402.

[7] Kim, J., and Moin, P., "The structure of the vorticity field in turbulent channel flow. Part 2. Study of ensemble-averaged fields," *Journal of Fluid Mechanics*, Vol. 162, 1986, pp. 339–363. https://doi.org/10.1017/S0022112086002070.

[8] Falco, R., "Coherent motions in the outer region of turbulent boundary layers," *The Physics of Fluids*, Vol. 20, No. 10, 1977, pp. S124–S132.

[9] Corino, E. R., and Brodkey, R. S., "A visual investigation of the wall region in turbulent flow," *Journal of Fluid Mechanics*, Vol. 37, No. 1, 1969, pp. 1–30. https://doi.org/10.1017/S0022112069000395.

[10] CunbiaoLee, and XianyangJiang, "Flow structures in transitional and turbulent boundary layers," *Physics of Fluids*, Vol. 31, No. 11, 2019, p. 111301. https://doi.org/10.1063/1.5121810.

[11] Grass, A. J., "Structural features of turbulent flow over smooth and rough boundaries," *Journal of Fluid Mechanics*, Vol. 50, No. 2, 1971, pp. 233–255. https://doi.org/10.1017/S0022112071002556.

[12] Grass, A. J., Stuart, R. J., Mansour-Tehrani, M., Walker, J. D. A., and Smith, F. T., "Vortical structures and coherent motion in turbulent flow over smooth and rough boundaries," *Philosophical Transactions of the Royal Society of London. Series A: Physical and Engineering Sciences*, Vol. 336, No. 1640, 1991, pp. 35–65. https://doi.org/doi:10.1098/rsta.1991.0065.

[13] Flack, K. A., Schultz, M. P., and Shapiro, T. A., "Experimental support for Townsend's Reynolds number similarity hypothesis on rough walls," *Physics of Fluids*, Vol. 17, No. 3, 2005, p. 035102. https://doi.org/10.1063/1.1843135.

[14] Jiménez, J., "Turbulent flows over rough walls," *Annual Review of Fluid Mechanics*, Vol. 36, No. 1, 2004, pp. 173–196. https://doi.org/10.1146/annurev.fluid.36.050802.122103.

[15] Fritsch, D. J., Vishwanathan, V., Lowe, K. T., and Devenport, W. J., "Fluctuating Pressure Beneath Smooth Wall Boundary Layers in Nonequilibrium Pressure Gradients," *AIAA Journal*, Vol. 0, No. 0, 2022, pp. 1–19. https://doi.org/10.2514/1.J061431.

[16] Bobke, A., Vinuesa, R., Örlü, R., and Schlatter, P., "History effects and near equilibrium in adverse-pressure-gradient turbulent boundary layers," *J. Fluid Mech*, Vol. 820, 2017, pp. 667–692.

[17] Lumley, J. L., *Stochastic tools in turbulence*, Courier Corporation, 2007.

[18] Baltzer, J., Adrian, R., and Wu, X., "Turbulent boundary layer structure identification via POD," *Proceedings of the summer program*, 2010, p. 55.

[19] Schmidt, O. T., and Colonius, T., "Guide to Spectral Proper Orthogonal Decomposition," *AIAA Journal*, Vol. 58, No. 3, 2020, pp. 1023–1033. https://doi.org/10.2514/1.J058809.

[20] Sieber, M., Paschereit, C. O., and Oberleithner, K., "Spectral proper orthogonal decomposition," *Journal of Fluid Mechanics*, Vol. 792, 2016, pp. 798–828. https://doi.org/10.1017/jfm.2016.103.

[21] Towne, A., Schmidt, O. T., and Colonius, T., "Spectral proper orthogonal decomposition and its relationship to dynamic mode decomposition and resolvent analysis," *Journal of Fluid Mechanics*, Vol. 847, 2018, pp. 821–867. https://doi.org/10.1017/jfm.2018.283.

[22] Duetsch-Patel, J. E., Vishwanathan, V., Minionis, J. B., Totten, E., Gargiulo, A., Fritsch, D. J., Szoke, M., Borgoltz, A., Roy, C. J., Lowe, K. T., and Devenport, W. J., *Aerodynamic Design and Assessment of Modular Test Section Walls for CFD Validation in Hybrid Anechoic Wind Tunnels*, 2020, p. 12p. https://doi.org/10.2514/6.2020-2214.

[23] Vishwanathan, V., Fritsch, D. J., Lowe, K. T., and Devenport, W. J., "Spatial Resolution Limitations of Particle Image Velocimetry in High Reynolds Number Turbulent Boundary Layers," , 2023.

[24] Vishwanathan, V., Fritsch, D. J., Lowe, K. T., and Devenport, W. J., "History effects and wall similarity of non-equilibrium turbulent boundary layers in varying pressure gradient over rough and smooth surfaces," *12th International symposium on turbulence and shear flow phenomena (TSFP12), Osaka, Japan (19-22 July, 2022)*, 2022.

[25] Smits, A. J., and Wood, D. H., "The Response of Turbulent Boundary Layers to Sudden Perturbations," *Annual Review of Fluid Mechanics*, Vol. 17, No. 1, 1985, pp. 321–358. https://doi.org/10.1146/annurev.fl.17.010185.001541.

[26] Andreopoulos, J., and Wood, D. H., "The response of a turbulent boundary layer to a short length of surface roughness," *Journal of Fluid Mechanics*, Vol. 118, 1982, pp. 143–164. https://doi.org/10.1017/S0022112082001001.

[27] Jacobi, I., and McKeon, B., "New perspectives on the impulsive roughness-perturbation of a turbulent boundary layer," *Journal of Fluid Mechanics*, Vol. 677, 2011, pp. 179–203.

[28] Townsend, A., *The structure of turbulent shear flow*, Cambridge university press, 1980.

Chapter 6

Conclusions and Outlook

6.1 Conclusions

This dissertation work describes experimental investigations focused on the velocity fields of high Reynolds number, non-equilibrium turbulent boundary layers over rough and smooth surfaces. Although a study of fundamental flow physics, this research is relevant to many practical applications as most real flows experience the compounding effects of roughness and pressure gradient (i.e. curvature or external forces). All measurements acquired as part of this research were conducted in the Virginia Tech Stability Wind Tunnel. A NACA 0012 airfoil was used as the mechanism to generate a systematically varying family of bi-directional pressure gradients over both the smooth and rough wall. Particle image velocimetry (PIV) was the main instrument used to measure the flow fields and generate the data presented in this dissertation. The rough wall consisted of a 2 mm tall circular cylindrical elements arranged in a staggered pattern, and produced flows that were in the fully turbulent and rough regime. This work is especially applicable for improving data driven modeling by improving the current experimental database for non-equilibrium rough and smooth wall boundary layers, which was previously lacking. The database of velocity and turbulence profiles are also made available through the Virginia Tech library (DOI pending). This work has highlighted key limitations with conventional evaluations of the wall-similarity hypothesis for rough wall flows. Additionally, limitations of particle image velocimetry spatial resolution on accurately measuring the anisotropy of turbulent fields are discussed.

The findings of the works presented in this dissertation thus far are summarized below.

- Regardless of wall condition and Reynolds number the flow in a non-equilibrium turbulent boundary layer exhibits increasingly non-local behavior with streamwise development. This is apparent as a lag in the response of the streamwise developing integrated boundary layer parameters (i.e. skin friction, momentum thickness, dis-

placement thickness) to the pressure gradient distribution. This behavior is referred to as a "history effect."

- There is clear evidence that rough wall boundary layers reduces the relaxation time to equilibrium in non-equilibrium flows.

- History effects are also prevalent in the mean velocity and Reynolds stress behaviors. In the mean velocity profiles, this is demonstrated as a "cross-over" of the favorable and adverse pressure gradient profiles in the logarithmic layer. Similar cross-over points are observed in the Reynolds shear and normal stresses, particularly at the streamwise station downstream of the pressure gradient switch. This behavior is indicative of a stress bore which gives indication of a large outward transport of velocities encompassed in these layers.

- For rough wall flows, indirect methods to determine skin friction, specifically using regression fits of the mean velocity profiles, show high sensitivity to of the selected logarithmic region on the computed shear stresses. Direct measurements of skin friction are necessary to accurately compare wall conditions on the basis of wall-similarity.

- The validity of wall-similarity is relevant to a huge range of engineering and modeling applications, but the present study has revealed that multiple criteria pertaining to flow histories, boundary layer thickness to roughness parameter ratios, and local Reynolds numbers must be matched to an equivalent smooth wall case for proper comparison on the basis of this hypothesis. Despite inherent uncertainties of indirect skin friction methods for the rough wall, the effective sandgrain roughness parameter is constant with pressure gradient history.

- Spatial resolution limitations of PIV experiments cause an attenuation of the measured turbulence statistics. There is no discernible impact of the resolution limitation to the resulting mean velocity profiles. However, Reynolds stresses show depressed values with coarser resolutions, with particular impacts to the wall-normal velocity components. This reduction was shown to be due to the smaller correlation lengthscales occurring the wall-normal direction as opposed to the energy-dominant larger scales occurring in the predominantly streamwise structures.

- A fixed spatial resolution presents limitations for studies in which variable flow conditions are compared. This is because the range of scales of turbulence, dictated by

the local Reynolds number, has a threshold of detection based on the instrument resolution. This limitation results in a higher disparity of Reynolds stress magnitudes of measurements made with a coarse and fine resolution when the flow is an initially adverse pressure gradient, a disparity that is comparably lower in flows in an initially zero or favorable pressure gradient.

- A comparison of the same variable quantities between the rough and smooth wall boundary layers show that the a coarse resolution can attenuate the computed Reynolds stresses for both rough and smooth wall flows. However, this stress magnitude reduction is more prevalent in the smooth wall flow, while the rough wall flow shows attenuation at certain local Reynolds numbers. Nevertheless, an evaluation of biases from under-resolution of non-dominant stress components is still necessary in the design of rough and smooth wall experiments.

- Qualitative analysis of the instantaneous smooth wall velocity fields shows evidence of Townsend's attached eddy hypothesis with the enlargement of eddy scales with wall-normal distance under adverse pressure gradient conditions.

- Both spectral proper orthogonal decomposition on the velocity fields and an evaluation of the instantaneous flow field shows that, although the rough wall qualitatively responds to the pressure gradient histories as the smooth wall, there are fundamental differences in the velocity field structure and shape, again emphasizing the need to match multiple variables for comparison of rough and smooth wall boundary layers on the basis of wall-similarity.

6.2 List of Publications

This work has and will be disseminated in the following conference and peer-reviewed journal publications, for which the current author has served as a primary or contributing (select works) author:

6.2.1 Peer-Reviewed Journal Proceedings

- **Vishwanathan, V.**, Fritsch, D. J., Lowe, K. T., and Devenport, W. J. "Spatial Resolution Limitations of Particle Image Velocimetry in High Reynolds Number Turbulent Boundary Layers." 2023. *In-Review*
- **Vishwanathan, V.**, Fritsch, D. J., Lowe, K. T., and Devenport, W. J. "History Effects and Wall Similarity of Non-Equilibrium Turbulent Boundary Layers in Varying Pressure Gradient Over Rough and Smooth Surfaces." 2023. *In-Review*
- Fritsch, D.J., **Vishwanathan, V.**, Lowe, K.T., and Devenport, W.J., "Fluctuating Pressure Beneath Smooth Wall Boundary Layers in Non-Equilibrium Pressure Gradients," AIAA Journal, 2022, Vol. 60, no. 8, pp. 4725-4743, doi: 10.2514/1.J061431

6.2.2 Conference Proceedings

- **Vishwanathan, V.**, Fritsch, D., Lowe, T. K., and Devenport, W. J. "Analysis of Coherent Structures over a Smooth Wall Turbulent Boundary Layer in Pressure Gradient Using Spectral Proper Orthogonal Decomposition," AIAA AVIATION 2021 FORUM. 2021., doi: 10.2514/6.2021-2893
- **Vishwanathan, V.**, Fritsch, D. J., Lowe, K. T., and Devenport, W. J. "History effects and wall similarity of non-equilibrium turbulent boundary layers in varying pressure gradient over rough and smooth surfaces," 12th International symposium on turbulence and shear flow phenomena (TSFP12), Osaka, Japan (19-22 July, 2022). 2022.

Additionally, the mean velocity, Reynolds stress, and mean pressure data will be made available through the Virginia Tech library data repository (DOI pending).

6.3 Outlook

The work presented in this dissertation has significantly improved our understanding of the resolution and structure of high Reynolds number turbulent boundary layers over rough and smooth surfaces in a systematically varying family of pressure gradients. Namely, this work has highlighted several considerations of experiment design for comparison of rough

and smooth wall boundary layers including measurement uncertainty due to under-resolved spatial fields, sensitivities of indirect skin friction methods for rough wall flow analyses, and has provided a list of comparative parameters necessary to evaluate the wall-similarity hypothesis. Nevertheless, several questions remain regarding this topic of study.

As currently presented, there are many opportunities for further analysis and technical expansion from the work investigated in this dissertation. Many rough wall studies, include the present work, have relied on indirect measurements of skin friction computed from mean velocity and Reynolds stress profiles. However, these methods have high levels of sensitivity associated with uncertainty in regressive fits of the mean profiles and/or require a demanding quantity of data along the streamwise developing flow history for methods using the momentum integral equations. Direct measurements of skin friction, such as by force balance or floating element systems, over rough wall surfaces are paramount in reducing uncertainty of roughness parameters and their ranges. Although these direct measurements may present logistical challenges, especially in high-Reynolds number flow fields performed in large-scale facilities, indirect estimates of rough wall skin friction make too many assumptions regarding the flow behavior in the outer regions of the boundary layer (i.e. that the logarithmic region follows a prescribed behavior).

This study has confirmed the importance of ensuring sufficiently large boundary layer thickness to effective sandgrain roughness ratios (δ/k_s) when evaluating the independence of outer-region flow behaviors from the roughness sublayer. Future work on this topic must consider flows that have, at minimum $\delta/k_s > 40$, but values upwards of this tolerance are highly recommended. The results from this work have also evidenced the highly non-local impacts for flow development in non-equilibrium flows. The mean velocity and turbulence stresses are not self-preserving and are highly dependent on upstream flow history, but these behaviors are qualitatively common across both rough and smooth surfaces. For instance, integrated boundary layer parameters show a lag in response to the changes in pressure gradient history, but the delay is shorter for the rough wall flow implying a faster relaxation towards equilibrium. Variations of pressure gradient history between rough and smooth wall flows result in a lack of collapse on the basis of wall-similarity. It is clear that, in addition to the δ/k_s parameter, history effects must be considered and matched between comparable flow conditions over rough and smooth surfaces.

One suggestion for future implementation of such comparative wall studies is to first establish the rough wall flow study and flow conditions and match the smooth wall flow parameters (i.e.

flow histories and characteristic parameters). As the rough wall flow conditions are highly dictated by parameters such as the effective sandgrain roughness and sublayer geometries, which are in addition to flow parameters already considered for the smooth wall, evaluating the rough wall flow first will simplify the design of experiments for matching conditions on the basis of wall-similarity for the smooth wall. Additionally, evaluating multiple families of pressure gradient histories, such as by changing the geometry of the mechanism for pressure gradient generation (i.e. rotating a different airfoil in the same experiment configuration used in this study), will improve the understanding of universally applicable flow behaviors that are not exclusive to a specific flow history.

Lastly, it is clear that limitations of instrument resolution in measuring anisotropic turbulent flow fields results in significant attenuation of measured turbulence stress magnitudes. For a wall boundary layer, the turbulence attenuation of the measurements is particularly dominant in the wall-normal component stresses as the fluctuating magnitudes are comparatively lower for the more dominant streamwise component. These impacts of resolution are prevalent in both rough and smooth wall flows, although the level of impact for the rough wall flow appears to be dependent on local Reynolds number and flow history. Regardless, convergence studies based on resolution refinement on improving measured turbulence stress magnitudes must be considered, and preferably quantified, to not mislead conclusions for comparative studies of varying flow conditions. Although out of the scope of the current investigation, the application of numerical extrapolation methods, based on the principles of Richardson extrapolation, is a potential way to correct under-resolved experimental measurements.

The results and conclusions of this study have provided significant breadth and depth of knowledge regarding the topic of non-equilibrium, high Reynolds number turbulent boundary layers over rough and smooth surfaces. However, this work has also highlighted the need for continued investigation on the comparative rough and smooth wall flows based on the provided suggestions to improve experiment design provided in this section.

Bibliography

[1] R. J. Adrian, C. D. Meinhart, and C. D. Tomkins. Vortex organization in the outer region of the turbulent boundary layer. *Journal of Fluid Mechanics*, 422:1–54, 2000. ISSN 0022-1120. doi: 10.1017/S0022112000001580.

[2] Ronald J. Adrian. Hairpin vortex organization in wall turbulence. *Physics of Fluids*, 19 (4):041301, 2007. doi: 10.1063/1.2717527.

[3] J. Andreopoulos and D. H. Wood. The response of a turbulent boundary layer to a short length of surface roughness. *Journal of Fluid Mechanics*, 118:143–164, 1982. ISSN 0022-1120. doi: 10.1017/S0022112082001001.

[4] R. A. Antonia and P. A. Krogstad. Scaling of the bursting period in turbulent rough wall boundary layers. *Experiments in Fluids*, 15(1):82–4, 1993. ISSN 0723-4864.

[5] R. A. Antonia and R. E. Luxton. The response of a turbulent boundary layer to an upstanding step change in surface roughness. *Journal of Basic Engineering*, 93(1):22–32, 1971. ISSN 0021-9223. doi: 10.1115/1.3425174.

[6] R. A. Antonia and R. E. Luxton. The response of a turbulent boundary layer to a step change in surface roughness. part 2. rough-to-smooth. *Journal of Fluid Mechanics*, 53 (4):737–757, 1972. ISSN 0022-1120. doi: 10.1017/S002211207200045X.

[7] Carolyn D Aubertine and John K Eaton. Turbulence development in a non-equilibrium turbulent boundary layer with mild adverse pressure gradient. In *Fourth International Symposium on Turbulence and Shear Flow Phenomena*. Begel House Inc., 2005. ISBN 2642-0554.

[8] R. Balachandar, D. Blakely, M. Tachie, and G. Putz. A study on turbulent boundary layers on a smooth flat plate in an open channel. *Transactions of the ASME. Journal of Fluids Engineering*, 123(2):394–400, 2001. ISSN 0098-2202. doi: 10.1115/1.1366321.

[9] P. R. Bandyopadhyay. Rough-wall turbulent boundary layers in the transition regime. *Journal of Fluid Mechanics*, 180:231–66, 1987. ISSN 0022-1120. doi: 10.1017/S0022112087001794.

[10] P. R. Bandyopadhyay and R. D. Watson. Structure of rough-wall turbulent boundary layers. *Physics of Fluids*, 31(7):1877–83, 1988. ISSN 0031-9171. doi: 10.1063/1.866686.

[11] D. J. Bergstrom, O. G. Akinlade, and M. F. Tachie. Skin friction correlation for smooth and rough wall turbulent boundary layers. *Journal of Fluids Engineering*, 127(6):1146–1153, 2005. ISSN 0098-2202. doi: 10.1115/1.2073288.

[12] R. Blackwelder and L. S. G. Kovasznay. Large scale motion of a turbulent boundary layer with a zero and a favorable pressure gradient. Report, Johns Hopkins Univ., USA, 1970.

[13] Alexandra Bobke, Ricardo Vinuesa, Ramis Örlü, and Philipp Schlatter. History effects and near equilibrium in adverse-pressure-gradient turbulent boundary layers. *J. Fluid Mech*, 820:667–692, 2017.

[14] K. K. Botros. Experimental investigation into the relationship between the roughness height in use with nikuradse or colebrook roughness functions and the internal wall roughness profile for commercial steel pipes. *Journal of Fluids Engineering*, 138(8), 2016. ISSN 0098-2202. doi: 10.1115/1.4032601.

[15] C. Bourassa and F. O. Thomas. An experimental investigation of a highly accelerated turbulent boundary layer. *Journal of Fluid Mechanics*, 634:359–404, 2009. ISSN 0022-1120. doi: 10.1017/S0022112009007289.

[16] P. Bradshaw and Y. M. Koh. A note on poisson's equation for pressure in a turbulent flow. *The Physics of Fluids*, 24(4):777–777, 1981. ISSN 0031-9171. doi: 10.1063/1.863442.

[17] K. C. Brown and P. N. Joubert. The measurement of skin friction in turbulent boundary layers with adverse pressure gradients. *Journal of Fluid Mechanics*, 35(4):737–757, 1969. ISSN 0022-1120. doi: 10.1017/S0022112069001418.

[18] Raul Bayoan Cal, Brian Brzek, Gunnar Johansson, and Luciano Castillo. Lda measurements on rough turbulent boundary layers subject to strong favorable pressure gradients. In *2006 ASME Joint U.S.- European Fluids Engineering Division Summer Meeting, FEDSM2006, July 17, 2006 - July 20, 2006*, volume 2 FORUMS of *Proceedings of ASME Fluids Engineering Division Summer Meeting 2006, FEDSM2006*, pages 1003–1012. American Society of Mechanical Engineers, 2006.

[19] Raúl Bayoán Cal, Brian Brzek, T Gunnar Johansson, and Luciano Castillo. The rough favourable pressure gradient turbulent boundary layer. *Journal of fluid mechanics*, 641: 129–155, 2009. ISSN 1469-7645.

[20] Francis H. Clauser. The turbulent boundary layer**the research presented in this article was supported by the office of scientific research, a.r.d.c.; u. s. air force, under contract af 18(600)671. the author was assisted by his colleagues drs. s. corrsin, g. corcos, and d. johnson. In H.L. Dryden and Th. von Kármán, editors, *The Turbulent Boundary Layer*, volume 4 of *Advances in Applied Mechanics*, pages 1–51. Elsevier, 1956. doi: https://doi.org/10.1016/S0065-2156(08)70370-3.

[21] Donald Coles. The law of the wake in the turbulent boundary layer. *Journal of Fluid Mechanics*, 1(2):191–226, 1956. ISSN 1469-7645.

[22] CunbiaoLee and XianyangJiang. Flow structures in transitional and turbulent boundary layers. *Physics of Fluids*, 31(11):111301, 2019. doi: 10.1063/1.5121810.

[23] David B. De Graaff and John K. Eaton. Reynolds-number scaling of the flat-plate turbulent boundary layer. *Journal of Fluid Mechanics*, 422:319–346, 2000. ISSN 0022-1120. doi: 10.1017/S0022112000001713.

[24] Shivsai Ajit Dixit and O. N. Ramesh. Determination of skin friction in strong pressure-gradient equilibrium and near-equilibrium turbulent boundary layers. *Experiments in Fluids*, 47(6):1045, 2009. ISSN 1432-1114. doi: 10.1007/s00348-009-0698-2.

[25] D. M. Driver. Application of oil-film interferometry skin-friction measurement to large wind tunnels. *Experiments in Fluids*, 34(6):717–725, 2003. ISSN 1432-1114. doi: 10.1007/s00348-003-0613-1.

[26] P. A. Durbin and S. E. Belcher. Scaling of adverse-pressure-gradient turbulent boundary layers. *Journal of Fluid Mechanics*, 238:699–722, 1992. ISSN 0022-1120. doi: 10.1017/S0022112092001873.

[27] M. P. Escudier, A. Abdel-Hameed, M. W. Johnson, and C. J. Sutcliffe. Laminarisation and re-transition of a turbulent boundary layer subjected to favourable pressure gradient. *Experiments in Fluids*, 25(5):491–502, 1998. ISSN 1432-1114. doi: 10.1007/s003480050255.

[28] RE Falco. Coherent motions in the outer region of turbulent boundary layers. *The Physics of Fluids*, 20(10):S124–S132, 1977. ISSN 0031-9171.

[29] D. S. Finnicum and T. J. Hanratty. Effect of favorable pressure gradients on turbulent boundary layers. *AIChE Journal*, 34(4):529–40, 1988. ISSN 0001-1541. doi: 10.1002/aic.690340402.

[30] Karen Flack, Michael Schultz, Julio Barros, and Y. C. Kim. Skin-friction behavior in the transitionally-rough regime. *International Journal of Heat and Fluid Flow*, 61: 21–30, 2016. doi: 10.1016/j.ijheatfluidflow.2016.05.008.

[31] Karen A. Flack and Michael P. Schultz. Roughness effects on wall-bounded turbulent flows. *Physics of Fluids*, 26(10):101305, 2014. doi: 10.1063/1.4896280.

[32] Karen A. Flack, Michael P. Schultz, and Thomas A. Shapiro. Experimental support for townsend's reynolds number similarity hypothesis on rough walls. *Physics of Fluids*, 17 (3):035102, 2005. doi: 10.1063/1.1843135.

[33] Daniel J. Fritsch, Vidya Vishwanathan, K. Todd Lowe, and William J. Devenport. Fluctuating pressure beneath smooth wall boundary layers in nonequilibrium pressure gradients. *AIAA Journal*, 0(0):1–19, 2022. doi: 10.2514/1.J061431.

[34] Davide Gatti, Alexander Stroh, Bettina Frohnapfel, and Ramis Örlü. Spatial resolution issues in rough wall turbulence. *Experiments in Fluids*, 63(3):63, 2022. ISSN 1432-1114. doi: 10.1007/s00348-022-03412-x.

[35] William K George and Luciano Castillo. Zero-pressure-gradient turbulent boundary layer. *Applied Mechanics Reviews*, 1997. ISSN 0003-6900.

[36] Y. G. Guezennec. Stochastic estimation of coherent structures in turbulent boundary layers. *Physics of Fluids A: Fluid Dynamics*, 1(6):1054–1060, 1989. doi: 10.1063/1.857396.

[37] Francis R. Hama. Boundary layer characteristics for smooth and rough surfaces. In *Boundary Layer characteristics for smooth and rough surfaces*, 1954.

[38] Zambri Harun, Jason P. Monty, Romain Mathis, and Ivan Marusic. Pressure gradient effects on the large-scale structure of turbulent boundary layers. *Journal of Fluid Mechanics*, 715:477–498, 2013. ISSN 0022-1120. doi: 10.1017/jfm.2012.531.

[39] M. R. Head and P. Bandyopadhyay. New aspects of turbulent boundary-layer structure. *Journal of Fluid Mechanics*, 107:297–338, 1981. ISSN 0022-1120. doi: 10.1017/S0022112081001791.

[40] M. R. Head and I. Rechenberg. The preston tube as a means of measuring skin friction. *Journal of Fluid Mechanics*, 14(1):1–17, 1962. ISSN 0022-1120. doi: 10.1017/S0022112062001020.

[41] N. Hutchins and Ivan Marusic. Evidence of very long meandering features in the logarithmic region of turbulent boundary layers. *Journal of Fluid Mechanics*, 579:1–28, 2007. ISSN 0022-1120. doi: 10.1017/S0022112006003946.

[42] Nicholas Hutchins and Ivan Marusic. Large-scale influences in near-wall turbulence. *Philosophical Transactions of the Royal Society A: Mathematical, Physical and Engineering Sciences*, 365(1852):647–664, 2007. doi: doi:10.1098/rsta.2006.1942.

[43] I Jacobi and BJ McKeon. Dynamic roughness perturbation of a turbulent boundary layer. *Journal of Fluid Mechanics*, 688:258–296, 2011. ISSN 0022-1120.

[44] I Jacobi and BJ McKeon. New perspectives on the impulsive roughness-perturbation of a turbulent boundary layer. *Journal of Fluid Mechanics*, 677:179–203, 2011. ISSN 0022-1120.

[45] Javier JimÉNez and Alfredo Pinelli. The autonomous cycle of near-wall turbulence. *Journal of Fluid Mechanics*, 389:335–359, 1999. ISSN 0022-1120. doi: 10.1017/S0022112099005066.

[46] Javier Jiménez. Turbulent flows over rough walls. *Annual Review of Fluid Mechanics*, 36(1):173–196, 2004. doi: 10.1146/annurev.fluid.36.050802.122103.

[47] Liselle AnnMarie Joseph. *Pressure fluctuations in a high-Reynolds-number turbulent boundary layer over rough surfaces of different configurations.* Thesis, Virginia Tech, 2017.

[48] Pranav Joshi and Joseph Katz. Experimental investigation of turbulent boundary layers under favorable pressure gradient. In *ASME 2010 3rd Joint US-European Fluids Engineering Summer Meeting, FEDSM 2010 Collocated with 8th International Conference on Nanochannels, Microchannels, and Minichannels*, volume 1 of *American Society of*

Mechanical Engineers, Fluids Engineering Division (Publication) FEDSM, pages 2085–2094. American Society of Mechanical Engineers (ASME), 2010. ISBN 08888116. doi: 10.1115/FEDSM-ICNMM2010-30764.

[49] Pranav Joshi, Xiaofeng Liu, and Joseph Katz. Effects of fluctuating pressure gradients on boundary layer turbulence. *Journal of Fluid Mechanics*, 748:36, 2014. doi: 10.1017/jfm.2014.147.

[50] John Kim and Parviz Moin. The structure of the vorticity field in turbulent channel flow. part 2. study of ensemble-averaged fields. *Journal of Fluid Mechanics*, 162:339–363, 1986. ISSN 0022-1120. doi: 10.1017/S0022112086002070.

[51] Philip S. Klebanoff. Characteristics of turbulence in a boundary layer with zero pressure gradient. In *Characteristics of turbulence in a boundary layer with zero pressure gradient*, 1955.

[52] S. J. Kline, W. C. Reynolds, F. A. Schraub, and P. W. Runstadler. The structure of turbulent boundary layers. *Journal of Fluid Mechanics*, 30(4):741–773, 1967. ISSN 0022-1120. doi: 10.1017/S0022112067001740.

[53] Andrey Nikolaevich Kolmogorov. The local structure of turbulence in incompressible viscous fluid for very large reynolds numbers. *Cr Acad. Sci. URSS*, 30:301–305, 1941.

[54] Leslie SG Kovasznay. Structure of the turbulent boundary layer. *The Physics of Fluids*, 10(9):S25–S30, 1967. ISSN 0031-9171.

[55] P. å Krogstad, R. A. Antonia, and L. W. B. Browne. Comparison between rough- and smooth-wall turbulent boundary layers. *Journal of Fluid Mechanics*, 245:599–617, 1992. ISSN 0022-1120. doi: 10.1017/S0022112092000594.

[56] P. Lavoie, G. Avallone, F. De Gregorio, G. P. Romano, and R. A. Antonia. Spatial resolution of piv for the measurement of turbulence. *Experiments in Fluids*, 43(1): 39–51, 2007. ISSN 1432-1114. doi: 10.1007/s00348-007-0319-x.

[57] Phillip M. Ligrani and Robert J. Moffat. Structure of transitionally rough and fully rough turbulent boundary layers. *Journal of Fluid Mechanics*, 162:69–98, 1986. ISSN 0022-1120. doi: 10.1017/S0022112086001933.

[58] John L Lumley. *Stochastic tools in turbulence*. Courier Corporation, 2007. ISBN 0486462706.

[59] Ivan Marusic, Jason P. Monty, Marcus Hultmark, and Alexander J. Smits. On the logarithmic region in wall turbulence. *Journal of Fluid Mechanics*, 716:R3, 2013. ISSN 0022-1120. doi: 10.1017/jfm.2012.511.

[60] R. Mathis, N. Hutchins, and I. Marusic. Large-scale amplitude modulation of the small-scale structures in turbulent boundary layers. *Journal of Fluid Mechanics*, 628:311–337, 2009. ISSN 0022-1120. doi: 10.1017/S0022112009006946.

[61] B. J. McKeon, A. S. Sharma, and I. Jacobi. Experimental manipulation of wall turbulence: A systems approach. *Physics of Fluids*, 25(3):031301, 2013. doi: 10.1063/1.4793444.

[62] Faraz Mehdi, Joseph C. Klewicki, and Christopher M. White. Mean momentum balance analysis of rough-wall turbulent boundary layers. In *Mean momentum balance analysis of rough-wall turbulent boundary layers*, volume 239 of *Physica D: Nonlinear Phenomena*, pages 1329–1337. Elsevier B.V., 2010. ISBN 01672789. doi: 10.1016/j.physd.2009.06.008.

[63] G. L. Mellor and D. M. Gibson. Equilibrium turbulent boundary layers. *Journal of Fluid Mechanics*, 24(2):225–253, 1966. ISSN 0022-1120. doi: 10.1017/S0022112066000612.

[64] A. J. Musker. Explicit expression for the smooth wall velocity distribution in a turbulent boundary layer. *AIAA Journal*, 17(6):655–657, 1979. doi: 10.2514/3.61193.

[65] Y Nagano, M Tagawa, and T Tsuji. *Effects of adverse pressure gradients on mean flows and turbulence statistics in a boundary layer*, pages 7–21. Springer, 1993.

[66] Johann Nikuradse. Laws of flow in rough pipes. *NACA Report*, 1950.

[67] M. Novean, J. Schetz, R. Bowersox, M. Novean, J. Schetz, and R. Bowersox. *Direct measurements of skin friction in complex supersonic flows*. AIAA, 2012. doi: 10.2514/6.1997-394.

[68] A. E. Perry and P. N. Joubert. Rough-wall boundary layers in adverse pressure gradients. *Journal of Fluid Mechanics*, 17(2):193–211, 1963. ISSN 0022-1120. doi: 10.1017/S0022112063001245.

[69] A. E. Perry, W. H. Schofield, and P. N. Joubert. Rough wall turbulent boundary layers. *Journal of Fluid Mechanics*, 37(2):383–413, 1969. ISSN 0022-1120. doi: 10.1017/S0022112069000619.

[70] Stephen B. Pope. *Turbulent Flows*. Cambridge University Press, Cambridge, 2000. ISBN 9780521598866. doi: DOI:10.1017/CBO9780511840531.

[71] L Prandtl. On the motion of fluids with very little friction. *English trans. in Early Developments of Modern Aerodynamics*, 1:484, 1905.

[72] S Rahgozar, Y Maciel, and Philipp Schlatter. Spatial resolution analysis of planar piv measurements to characterise vortices in turbulent flows. *Journal of Turbulence*, 14(10): 37–66, 2013. ISSN 1468-5248.

[73] M. R. Raupach, R. A. Antonia, and S. Rajagopalan. Rough-wall turbulent boundary layers. *Applied Mechanics Reviews*, 44(1):1–25, 1991. ISSN 0003-6900. doi: 10.1115/1.3119492.

[74] Lewis Fry Richardson. Atmospheric diffusion shown on a distance-neighbour graph. *Proceedings of the Royal Society of London. Series A, Containing Papers of a Mathematical and Physical Character*, 110(756):709–737, 1926. ISSN 0950-1207.

[75] S. K. Robinson. Coherent motions in the turbulent boundary layer. *Annual Review of Fluid Mechanics*, 23(1):601–639, 1991. ISSN 0066-4189. doi: 10.1146/annurev.fl.23.010191.003125.

[76] Joseph A Schetz and Rodney DW Bowersox. *Boundary layer analysis*. American Institute of Aeronautics and Astronautics, 2011. ISBN 160086824X.

[77] W. H. Schofield. Measurements in adverse-pressure-gradient turbulent boundary layers with a step change in surface roughness. *Journal of Fluid Mechanics*, 70(3):573–593, 1975. ISSN 0022-1120. doi: 10.1017/S0022112075002200.

[78] C Rt Smith, JDA Walker, AH Haidari, and U Sobrun. On the dynamics of near-wall turbulence. *Philosophical Transactions of the Royal Society of London. Series A: Physical and Engineering Sciences*, 336(1641):131–175, 1991. ISSN 0962-8428.

[79] A. J. Smits, S. T. B. Young, and P. Bradshaw. The effect of short regions of high surface curvature on turbulent boundary layers. *Journal of Fluid Mechanics*, 94(2): 209–242, 1979. ISSN 0022-1120. doi: 10.1017/S0022112079001002.

[80] AJ Smits, J Monty, Marcus Hultmark, Sean Christoper Collison Bailey, Nicholas Hutchins, and Ivan Marusic. Spatial resolution correction for wall-bounded turbulence measurements. *Journal of Fluid Mechanics*, 676:41–53, 2011. ISSN 1469-7645.

[81] Philippe R. Spalart. Direct simulation of a turbulent boundary layer up to r = 1410. *Journal of Fluid Mechanics*, 187:61–98, 1988. ISSN 0022-1120. doi: 10.1017/S0022112088000345.

[82] Philippe R. Spalart and Jonathan H. Watmuff. Experimental and numerical study of a turbulent boundary layer with pressure gradients. *Journal of Fluid Mechanics*, 249: 337–371, 1993. ISSN 0022-1120. doi: 10.1017/S002211209300120X.

[83] DB Spalding. A single formula for the "law of the wall". 1961. ISSN 0021-8936.

[84] D. T. Squire, C. Morrill-Winter, N. Hutchins, I. Marusic, M. P. Schultz, and J. C. Klewicki. Smooth- and rough-wall boundary layer structure from high spatial range particle image velocimetry. *Physical Review Fluids*, 1(6):064402, 2016. doi: 10.1103/PhysRevFluids.1.064402.

[85] DT Squire, C Morrill-Winter, N Hutchins, MP Schultz, JC Klewicki, and I Marusic. Comparison of turbulent boundary layers over smooth and rough surfaces up to high reynolds numbers. *Journal of Fluid Mechanics*, 795:210–240, 2016. ISSN 0022-1120.

[86] A. A. Townsend. Equilibrium layers and wall turbulence. *Journal of Fluid Mechanics*, 11(1):97–120, 1961. ISSN 0022-1120. doi: 10.1017/S0022112061000883.

[87] AAR Townsend. *The structure of turbulent shear flow*. Cambridge university press, 1980. ISBN 0521298199.

[88] Ricardo Vinuesa, Ramis Orlu, Carlos Sanmiguel Vila, Andrea Ianiro, Stefano Discetti, and Philipp Schlatter. Revisiting history effects in adverse-pressure-gradient turbulent boundary layers. *Flow, Turbulence and Combustion*, 99(3):565–587, 2017. ISSN 1573-1987. doi: 10.1007/s10494-017-9845-7.

[89] Vidya Vishwanathan, Danny Fritsch, Todd K. Lowe, and William J. Devenport. *Analysis of Coherent Structures over a Smooth Wall Turbulent Boundary Layer in Pressure Gradient Using Spectral Proper Orthogonal Decomposition*. 2021. doi: 10.2514/6.2021-2893.

[90] Vidya Vishwanathan, Daniel J Fritsch, K Todd Lowe, and William J Devenport. History effects and wall similarity of non-equilibrium turbulent boundary layers in varying pressure gradient over rough and smooth surfaces. In *12th International symposium on turbulence and shear flow phenomena (TSFP12), Osaka, Japan (19-22 July, 2022)*, 2022.

[91] Ralph J. Volino and Michael P. Schultz. Determination of wall shear stress from mean velocity and reynolds shear stress profiles. *Physical Review Fluids*, 3(3):034606, 2018. doi: 10.1103/PhysRevFluids.3.034606.

[92] James M. Wallace, Robert S. Brodkey, and Helmut Eckelmann. Pattern-recognized structures in bounded turbulent shear flows. *Journal of Fluid Mechanics*, 83(4):673–693, 1977. ISSN 0022-1120. doi: 10.1017/S0022112077001402.

[93] J. Zhou, R. J. Adrian, S. Balachandar, and T. M. Kendall. Mechanisms for generating coherent packets of hairpin vortices in channel flow. *Journal of Fluid Mechanics*, 387: 353–396, 1999. ISSN 0022-1120. doi: 10.1017/S002211209900467X.